

TECHNICAL UNIVERSITY OF CRETE

DIPLOMA THESIS

Measurement and Modeling of Point Spread Function for Improving the Spatial Resolution in Microscopy

Author:
Evangelos TZARDIS

Supervisor:
Prof Costas BALAS



*A thesis submitted in partial fulfillment of the requirements
for the Diploma of Electrical and Computer Engineering*

in the

Electronics Laboratory
Department of Electrical and Computer Engineering

THESIS COMMITTEE
Professor Costas BALAS
Professor Demosthenes ELLINAS
Associate Professor George N. KARYSTINOS

October, 2017

Acknowledgements

I would like to express my everlasting esteem and gratitude towards my thesis supervisor Prof. Costas BALAS who along with my thesis advisor and colleague Kastrinakis Marios gave me the inspiration and the will to learn and work on new for me scientific fields.

A BIG thanks as well to the guys in the lab who gave me the necessary insight of the used experimental equipment and of course provided a friendly collaborative environment.

Last but not least, a HUGE thanks to my family and my close friends for their continuous and constant support throughout my university life and especially when emerging situations stumped me.

Abstract

Due to the widespread use of the light microscope as a diagnostic tool for many scientific fields like medicine, biology, chemistry as well as for industrial applications, light microscopy has been undergoing vast and continuing innovations both regarding the hardware and software domain. The optical resolution of light microscopes is physically constrained by the phenomenon of diffraction. Out-of-focus light and light originated from adjacent areas of a sample are superposed degrading the quality of the image of the object under study. In this degradation, the Point Spread Function (PSF) of the optical system is the main culprit and it is the one that determines the optical resolution. This degradation effect can be eased by sophisticated and expensive confocal microscopy systems or reversed to some degree by much cheaper widefield deconvolution microscopy methods. Deconvolution processes need a PSF as much as accurate it can be in order to provide satisfactory and realistic results. The description of the PSF can be done either by mathematical models or by experimental measurements. Experiments for this purpose include measurements of fluorescent microbeads as well as estimation of the Modulation Transfer Function (MTF) of the optical systems which finally yields the PSF. The present diploma thesis deals with the mathematical modelling of the PSF in comparison with its experimental measurement via a method that uses the general MTF estimation process, with application on optical microscopes. This evaluation is done with the use of quantitative metrics that describe the quality of the deconvolved images aiming at an objective assessment of them. Results show a superiority of the experimental PSF as far as the metrics are concerned. As for the visual perception, deconvolution with a modelled PSF seems to produce results of higher contrast. Contrast enhancement is therefore not in agreement necessarily with the improvement of images that approaches the real optical information. In addition, several standard contrast enhancement techniques are used for extra comparison. This work is integrated in a graphical user interface which additionally allows quantitative comparison on user-imported images.

Contents

Acknowledgements	iii
Abstract	v
List of Abbreviations	x
1 Introduction	1
2 Background information and theory	3
2.1 Microscopy	3
2.1.1 Magnification of lenses	3
2.1.2 Diffraction-limited resolution	8
2.1.3 Anatomy of an optical microscope	11
2.1.4 Fluorescence Microscopy	11
2.2 Point Spread Function	15
2.2.1 Theoretical PSF	16
2.2.2 Experimental PSF	19
2.3 Modulation Transfer Function - Optical Transfer Function	20
2.3.1 Physical meaning and PSF-MTF-OTF relation	20
2.3.2 Experimental measurement of MTF - slanted edge	21
2.4 Image formation and deblurring technologies	24
2.4.1 Sources of image degradation	24
2.4.2 Deblurring technologies	25
2.4.3 Standard Processing Techniques	37
2.5 Quantitative metrics of image quality and enhancement	37
3 Deconvolution algorithms GUI with measuring and modelling PSF	41
3.1 Getting to know the GUI	41
3.2 Code implementation	43
3.2.1 Files and directories	43
3.2.2 Software Experiments	45
Experimental vs Modelled PSF comparison using quantitative metrics	45
4 Explanation of software experiments results	81
4.1 Conclusions	81
4.2 Discussion	85
Bibliography	87

List of Figures

2.1	Principal interactions of light with a medium	3
2.2	Different shapes of simple lenses	4
2.3	Image formation of an object with a convex lens	5
2.4	An objective-eyepiece compound	6
2.5	An objective-tube-eyepiece compound	7
2.6	Diffraction by Huygens-Fresnel principle	8
2.7	Fraunhofer diffraction	9
2.8	Angle of first intensity minimum (left) - Diffraction pattern formed on the sensor across the vertical line the diffraction curve extends (1D) (middle) - Diffraction pattern formed across the whole sensor plane (2D - Airy disk) (right)	9
2.9	Basic parts of a typical optical microscope	12
2.10	Widefield epi-illumination fluorescence microscope schematic	13
2.11	Jablonski energy diagram showing transitions involved in absorption and emission of light by a fluorochrome. Straight lines show absorption or emission of a photon, whereas wavy lines show non-radiative processes.	14
2.12	PSF formed by 2,3 and 9 wavelets of the Huygens-Fresnel model	16
2.13	PSF formed by "infinite" wavelets of the Huygens-Fresnel model. The hourglass-like shape of the PSF in the center defines the detail in which the point source is resolved. The red dotted line is the optical axis along which the light travels	16
2.14	The true analog ESF (along 1 spatial direction for simplification) (top left) will be digitized but with a quantization error which depends on the number of pixels in the horizontal axis of the sensor and the single pixel size. Top right, bottom left and bottom right show 2, 0 and 1 samples respectively which define the edge.	22
2.15	Every center a pixel is assumed the role of a sample of the ESF	22
2.16	30
3.1	Initial deconvolution algorithms GUI with highlighted panels	41
3.2	PSF generation	42
3.3	Deconvolution results with the use of the measured PSF (in comparison with the original image and the Blind deconvolution result).	49
3.4	50
3.5	Deconvolution results with the use of the modelled PSF (in comparison with the original image and the Blind deconvolution result).	51
3.6	52
3.7	SPT results	55
3.8	Intensity profiles	56
3.9	57
3.10	Convergence of iterative algorithms - execution times	58
3.11	Residual norms of every algorithm	58
3.12	SSIM of every algorithm	59

3.13	I-divergence of every algorithm	59
3.14	Standard Processing Techniques comparison	60
3.15	Deconvolution results with the use of the measured PSF (in comparison with the original image and the Blind deconvolution result).	61
3.16	62
3.17	Deconvolution results with the use of the modelled PSF (in comparison with the original image and the Blind deconvolution result).	63
3.18	64
3.19	SPT results	65
3.20	Intensity profiles	66
3.21	67
3.22	Convergence of iterative algorithms - execution times	68
3.23	Residual norms of every algorithm	68
3.24	SSIM of every algorithm	69
3.25	I-divergence of every algorithm	69
3.26	Standard Processing Techniques comparison	70
3.27	Deconvolution results with the use of the measured PSF (in comparison with the original image and the Blind deconvolution result).	71
3.28	72
3.29	Deconvolution results with the use of the modelled PSF (in comparison with the original image and the Blind deconvolution result).	73
3.30	74
3.31	SPT results	75
3.32	Intensity profiles	76
3.33	77
3.34	Convergence of iterative algorithms - execution times	78
3.35	Residual norms of every algorithm	78
3.36	SSIM of every algorithm	79
3.37	I-divergence of every algorithm	79
3.38	Standard Processing Techniques comparison	80

List of Abbreviations

NA	N umerical A perture
PSF	P oint S pread F unction
OTF	O ptical T ransfer F unction
MTF	M odulation T ransfer F unction
PTF	P hase T ransfer F unction
ESF	E dge S pread F unction
LSF	L ine S pread F unction
NIF	N aive I nverse F ilter
RIF	R egularized I nverse F ilter
TRIF	T ikhonov R egularized I nverse F ilter
LW	L and W eber algorithm
ICTM	I terative C onstrained T ikhonov- M iller algorithm
JVC	J ansson- V an C ittert algorithm
RL	R ichardson L ucy algorithm
RLTV	R ichardson L ucy - T otal V ariation algorithm
FISTA	F ast I terative S oft- T hresholding A lgorithm
SPT	S tandard P rocessing T echniques
SSIM	S tructural S IMilarity index

Chapter 1

Introduction

The widespread use of light microscope as a diagnostic tool for many scientific fields like medicine, biology, chemistry as well as for industrial applications, has provoked vast and continuing innovations both regarding the hardware and software domain. The motive behind this dissertation lies in the ascertained fact that optical imaging in general exhibits inherent physical limitations. These limitations are due to the phenomenon of diffraction. As it is elaborated in the next chapter, an object under study is not depicted as it is in the reality. More specifically, its image is degraded due to many reasons involving blur, glare, scatter of light and incoming photon related noise. The aforementioned diffraction phenomenon is related to blur. The work realised in this thesis deals with the following concept. Out-of-focus light and light originated from adjacent areas of a sample are superposed blurring the image of the object under study. For this effect, the Point Spread Function (PSF) of the optical system is the main culprit and it is the one that determines the optical resolution. This degradation effect can be eased by sophisticated and expensive confocal microscopy systems or reversed to some degree by much cheaper widefield deconvolution microscopy methods. Deconvolution processes need a PSF as much as accurate it can be in order to provide satisfactory and realistic results. The description of the PSF can be done either by mathematical models or by experimental measurements. Experiments for this purpose include measurements of fluorescent microbeads as well as estimation of the Modulation Transfer Function (MTF) of the optical systems which finally yields the PSF.

The present diploma thesis deals with the mathematical modelling of the PSF in comparison with its experimental measurement via a method that uses the general MTF estimation process, with application on optical microscopes. This evaluation is done with the use of quantitative metrics that describe the quality of the deconvolved images aiming at an objective assessment of them. Results show a superiority of the experimental PSF as far as the metrics are concerned. As for the visual perception, deconvolution with a modelled PSF seems to produce results of higher contrast. Contrast enhancement is therefore not in agreement necessarily with the improvement of images that approaches the real optical information. In addition, several standard contrast enhancement techniques are used for extra comparison. This work is integrated in a graphical user interface which additionally allows quantitative comparison on user-imported images.

In order for someone to be introduced to the above-mentioned matter, at first the basic physical concepts are gradually explained. Beginning with how lenses in general work, how their providing magnification is defined and in which way the optical resolution of an optical system is limited, one can get to know the basic stuff behind the field of optics. Then, the anatomy of a modern conventional microscope is described. At this point, the concept of fluorescence and the anatomy of a fluorescent

microscope is explained, since the test images used in this thesis contain a fluorescence microscope.

Knowing the parts of an optical system and how the its provided images are physically degraded, one can go deeper into how a PSF can be mathematically modelled and how it can alternatively be experimentally measured.

Finally, since the blurring effect in an image, is mathematically described using the concept of convolution, the rest background chapter deals with de-convolution methods with their ultimate goal to be the de-blurring of the captured image.

Chapter 2

Background information and theory

2.1 Microscopy

Microscopy is the technical field of using microscopes to view objects and areas of objects that cannot be seen with the naked eye (objects that are not within the resolution range of the normal eye). There are three well-known branches of microscopy: optical, electron, and scanning probe microscopy. Optical (light) microscopy, which is the case of study, uses visible light and a system of lenses in order to project a magnified image of a specimen under study on the eye or on a camera sensor.

2.1.1 Magnification of lenses

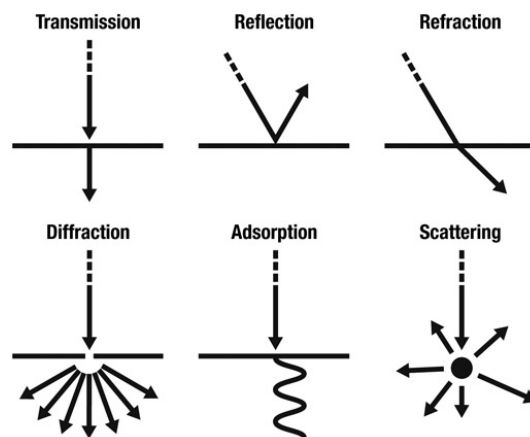


FIGURE 2.1: Principal interactions of light with a medium

Source: [http://](http://physicsweekly.weebly.com/reflection-refraction-and-diffraction.html)

physicsweekly.weebly.com/reflection-refraction-and-diffraction.html

Light can interact with a medium in many ways, depending on the material of the medium, the angle of the incidence and the wavelength. Fig. 2.1 is self explanatory. As for **diffraction** (expounded in Sec. 2.1.2), this phenomenon is based on the principals of constructive and destructive wave interference. Light behaves in the same way as a mechanical wave encountering an obstacle or passing through a slit. It is defined as the bending of light around the corners of an obstacle or a slit (aperture) into the region of geometrical shadow of the obstacle. In order to exhibit diffraction, this obstacle or this slit must be comparable in size with the wavelength of the

encountering wave. From this, also it follows that an obstacle or a slit can have sharp edges.

In microscopy, all these kinds of interaction are significant. Transmission, reflection, refraction are used to build a path for the light rays. Diffraction, absorption and scattering, though, eventually act as degrading factors for the microscoped image.

For the purposes of light microscopy, the basic components relative to the optical train are **lenses** and **filters**.

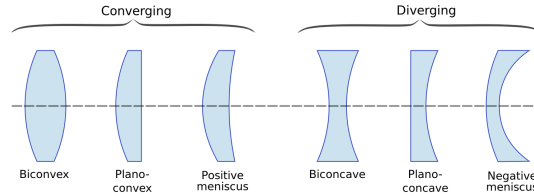


FIGURE 2.2: Different shapes of simple lenses

Source: http://data.allenai.org/tqa/optics_L_0755/

LENSES

Lenses come in different shapes (Fig. 2.2). They can be grouped and form a compound system with special properties (i.e better focusing, better magnification or eradication of aberrations). Two are the main characteristics of a lens. The distance over which initially parallel light rays are brought to a focus (**focal length** f) and the **magnification**. Image formation happens when light rays converge either in real or seem to do so (virtually). [1]

- A real image is formed in the plane where light rays converge in real (using converging lenses) and the object to be pictured is placed farther than the focal length of the lens. When the object is placed in between f and $2f$ the image is bigger than the object, whereas when it is placed in a distance bigger than $2f$ the image is smaller. A real image is always inverted and can be formed in a screen. For a converging lens, the focal length is said to be positive, which is the reason why they are also called positive.
- A virtual image is formed in the plane where light rays seem to converge (continuing ,virtually backwards, the rays coming out of the lens). This happens in diverging lenses or when the object to be pictured is placed inside the focal distance of a converging lens. A virtual image is always erect and cannot be projected onto a screen as it on the same side of the lens as the object.

THIN LENS

In the simple case of just one thin convex lens(thickness is negligible) (Fig. 2.3), the equation of the thin lens (Eq. 2.1) and the provided magnification (Eq. 2.2) can be computed, using the metric relations of the formed triangles: [4]

$$\frac{1}{s_1} + \frac{1}{s_2} = \frac{1}{f} \quad (2.1)$$

, where s_1 : object to lens distance, s_2 : real image to lens distance, f : focal length

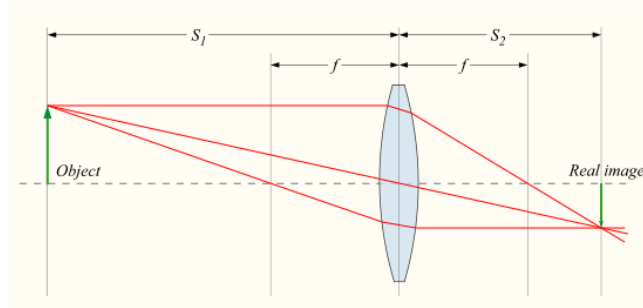


FIGURE 2.3: Image formation of an object with a convex lens
Source: [https://en.wikipedia.org/wiki/Lens_\(optics\)](https://en.wikipedia.org/wiki/Lens_(optics))

$$M = \frac{y_i}{y_o} = \frac{s_2}{s_1} \quad (2.2)$$

, where y_i : image height, y_o : object height

Usually, the object is put on the f_o , so the above equation becomes:

$$M = \frac{y_i}{y_o} = \frac{s_2}{f_o} \quad (2.3)$$

LENS WITH IMPORTANT THICKNESS

When the thickness of the lens is not negligible, in order to compute the effective focal length, **radii of the curvature** (RoC) of each side of the lens, along with the **refractive index** (r.i) of the lens medium must be known. So the corresponding equation is:

$$\frac{1}{f} = (n - 1) \left[\frac{1}{R_1} - \frac{1}{R_2} + \frac{(n - 1)d}{nR_1R_2} \right] \quad (2.4)$$

, where R_1 : RoC of closer to the light source lens side, R_2 : RoC of farther to the light source lens side, n : r.i of the lens medium, d : lens thickness

TWO LENS SYSTEM (*thin lenses*)

A compound microscope system of two lenses provides better magnification than that of one lens. It consists of at least two converging lenses; the **objective** and the **eyepiece**. The former has a focal length $f_o < 1$ cm and the latter has a f_e of a few cm. The total magnification M of the two lenses is given by the product of the magnifications of the individual lenses. Thus, we have:

$$M = M_{objective} \times M_{eyepiece} \quad (2.5)$$

The individual magnifications are given by 2.2, which in order lead to:

$$M = \frac{S_2}{S_1} \times \frac{S'_2}{S'_1} \quad (2.6)$$

The distances between object-objective lens S_1 , objective lens-real (first) image S_2 and real image-eyepiece lens S'_1 may vary. But the distance between the eyepiece lens

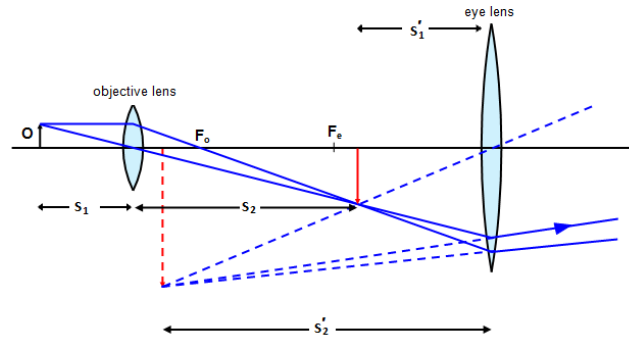


FIGURE 2.4: An objective-eyepiece compound

Source: <https://physics.stackexchange.com/questions/307050/>

[why-we-take-objective-of-short-focal-length-and-eye-piece-of-long-focal-length-i](https://physics.stackexchange.com/questions/307050/why-we-take-objective-of-short-focal-length-and-eye-piece-of-long-focal-length-i)

and the virtual (final) image S_2' is set to 25 cm. This is because 25 cm is the closest point at which an object can be brought into focus by a "normal" human eye. Closest distance is important, because apparently the image of the object will be the most detailed it can be. Eventually, the eye perceives the final magnified image as if it were in that distance of 25 cm.

When the object is put on the f_o , the intermediate image is formed on the f_e . Hence the above equation becomes:

$$M = \frac{T}{f_o} \times \frac{25 \text{ cm}}{f_e} \quad (2.7)$$

, where T : distance between f_o and f_e , usually 16 cm

CONVENTIONAL MICROSCOPE LENSES

In a typical microscope a third lens is added, namely the **tube lens**, for the reason that the objective lens projects incoming light into infinity. The tube lens forms the real image on its focal point. Light rays originating from the two ends of the object are adequate for the purpose of explaining conventional microscope lenses. To take it from the start: The objective (Fig.2.5(2)) is designed to project the incoming light rays of the object (Fig.2.5(1)) into infinity. Then, the tube lens (Fig. 2.5(3)) produces a magnified intermediate image (Fig.2.5(4)) which in turn is captured by the eyepiece (Fig.2.5(5)) and finally shown to the eye (Fig.2.5(6)). The resulting viewing angle δ_1 of the case A is much larger than δ_2 of case B, where the object is seen directly from a distance of approximately 25 cm. Regarding the overall magnification of such a system, it can be computed by the product of the individual magnifications of the objective and the eyepiece lenses. [3]

USING AN IMAGE CAPTURING SYSTEM INSTEAD OF THE EYEPIECE

In cases that recording of the specimen in an imaging system of a sensor and a computer monitor is preferred, the eyepiece can be omitted. The magnification is produced by the optical system (i.e objective, tube lens) and the electronic imaging system which provides a magnification factor due to the optical to electronic system adaptor (computer monitor adaptor). The total magnification of the system can be computed as:

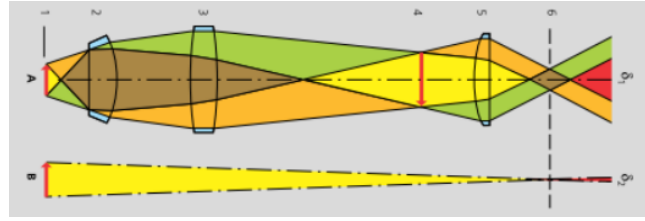


 FIGURE 2.5: An objective-tube-eyepiece compound

$$M_{overall} = M_{optical} \times M_{electronic} \quad (2.8)$$

The optical magnification in case of just one objective and an adapter is given by:

$$M_{optical} = M_{objective} \times M_{adapter} \quad (2.9)$$

The electronic magnification is the ratio of the active sensor diagonal and the useful monitor diagonal:

$$M_{electronic} = diagonal_{monitor} / diagonal_{sensor} \quad (2.10)$$

WHAT ARE THE LIMITS OF MAGNIFICATION - USEFUL MAGNIFICATION

As it was mentioned above, greater magnification can be achieved using two or more lenses. So, the question is if there are any boundaries to magnifying an object infinitely. The short answer is NO. Despite the fact that with an infinite number of lenses an infinite magnification is achieved, after a point that huge magnification is useless because "deeper" details of the magnified object cannot be resolved further. So the maximum useful magnification for a conventional optical microscope it is known to be 2000x. In terms of the tiniest possible distinguishable area of an object, the conventional optical microscope can produce a virtual image of a 200 nm diameter spot of the object. This is approximately the width of an average-sized bacterium. The smaller this distinguishable area is, the bigger the resolution of the microscope is. However, in practice this resolution of 200 nm cannot be approached due to lenses' imperfections. Further improvements have been accomplished by the nobel prize-awarded Super Resolution Microscopy which circumvents the aforementioned limit and brings it to the nanodimension. The explanation to the existence of a limit to the resolving power of the microscope, lies in the concept of diffraction which is eventually the reason why more and more magnification power of lenses lead merely to a magnification of the smallest distinguishable area, without unveiling further details.

2.1.2 Diffraction-limited resolution

DIFFRACTION - WHY IT HAPPENS AND HOW IT IS AFFECTED

Lens-systems have an opening which allows a cone of light to pass through. Here lies the resolution limitation of the microscope (and of every optical device incorporating apertures). As it was mentioned in the early introduction of this section, light bends around the corners of an obstacle or a slit (aperture) into the region of geometrical shadow of the obstacle when the size of the latter is comparable with the wavelength of the incoming light. From this, also it follows that light bends around the sharp edges of an obstacle or an aperture.

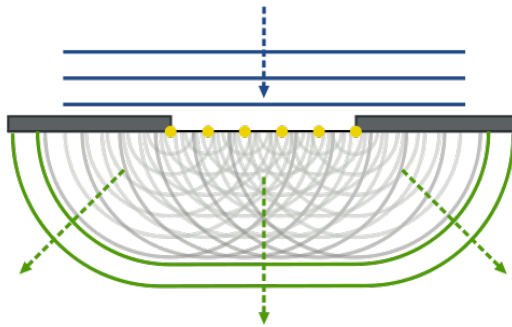


FIGURE 2.6: Diffraction by Huygens-Fresnel principle

Source: https://en.wikipedia.org/wiki/Huygens%E2%80%93Fresnel_principle

The significance of the phenomenon of diffraction in the case of image capturing lies in the fact that light does not travel linearly from the aperture towards the sensor (camera or human eye), but instead spreads to a cone angle. As it was mentioned earlier, light diffraction behaves in the same way a mechanical wave behaves entering a slit. The spreading of the post-aperture light can be explained by the Huygens-Fresnel principle. It argues that every single point of a wave front (wavelet) acts like a source of new spherical waves. These emanating waves interfere constructively or destructively with themselves creating a characteristic pattern in the post-aperture area. In Fig. 2.6, this principle is visualized with the use of 6 wavelets at the level of the aperture. While these waves propagate the total aggregating wave front takes the form of the green lines, giving the effect of the spreading of light.

When the spreading light eventually "hits" the sensor, a two-dimensional diffraction pattern appears on it. This is the resolved image of the point light source. So, as long as the light bends after it passes through the slit, the resolved image is larger. This means that the final captured image is a degraded form of the true point source. Fig. 2.7 exhibits a case where light arrives at the aperture in plane wave fronts. That is accomplished when the light source, the aperture and the sensor are far apart in order for the spherical source waves to expand in such a degree that their wave fronts become plane or close to plane. Another occasion is when curved wave fronts enter the objective lens of the microscope and come out as plane ones. This is the Fraunhofer diffraction. In case where the incoming wave fronts are curved and sensor is relatively close to the aperture, Fresnel diffraction applies. Fraunhofer diffraction helps the understanding of the parameters that affect the level of light bending and the diffraction patterns on the sensor, because of its simplicity compared to Fresnel

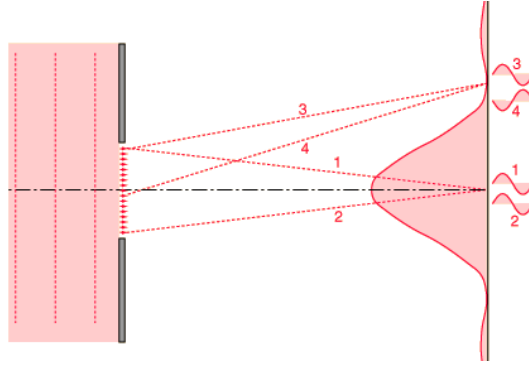


FIGURE 2.7: Fraunhofer diffraction

Source:

<http://hyperphysics.phy-astr.gsu.edu/hbase/phyopt/sinlitd.html#c1>

diffraction. The figure shows the sensor plane and the intensity of light in each point on it.

A wave of light interferes constructively with another of the same wavelength λ when their path lengths differ by m multiples of λ . They interfere destructively when their path lengths differ by $(m + \frac{1}{2})\lambda$. In Fig. 2.7 rays 3 and 4 arrive 180 degrees out of phase on the sensor and lead to a minimum light intensity in that point. Rays 1 and 2 arrive in phase and lead to maximum light intensity.

In order to calculate how much the light diffracts, after it passes the aperture, it is sufficient to calculate the angle of the first intensity minimum over the optical axis (aperture middle). From Fig. 2.8, using trigonometric small-angle approximations (because Fraunhofer approach considers that aperture to slit length $L \gg w$ and thus $\theta' \approx \theta$) and applying the destructive interference condition $\frac{w}{2} \sin \theta = \frac{\lambda}{2}$, it can be shown that the angle of first intensity minimum (first trough or dark fringe) is:

$$\sin \theta = 1.22 \frac{\lambda}{w} \quad (2.11)$$

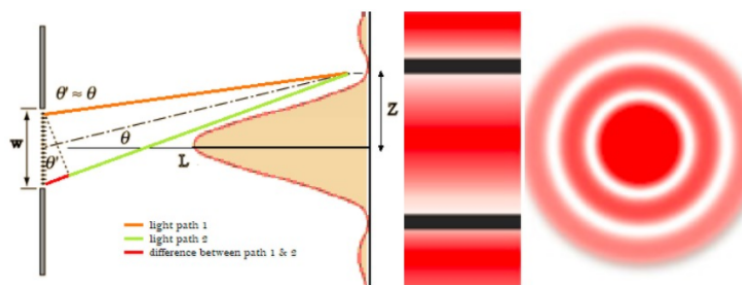


FIGURE 2.8: Angle of first intensity minimum (left) - Diffraction pattern formed on the sensor across the vertical line the diffraction curve extends (1D) (middle) - Diffraction pattern formed across the whole sensor plane (2D - Airy disk) (right)

Source: Own illustration

The above equation makes clear that the longer the wavelength of the incoming light, the larger the level of light bending after the aperture. Additionally, the bigger the aperture, the smaller the degree to which the light diffracts. Hence, in order to have a better resolved image of the true point source regardless its wavelength, the

bigger the aperture is, the better this can be achieved. Bigger aperture means longer lens so as the latter gathers all the light that passes through the aperture. To express how large cone of light a lens can gather, a quantity is introduced:

NUMERICAL APERTURE AND RESOLUTION

Numerical Aperture of a lens (NA) : characterizes the range of angles over which the lens can accept (or emit) light. It is a function of the refractive index n of the medium in which the lens is working (i.e air, water, oil) and half the angle (θ) of the largest pencil of light that the lens can accept (or emit). [4]

$$NA = n \sin \theta \quad (2.12)$$

From this definition along with the aforementioned simple aperture characteristics, it can be concluded that the bigger the numerical aperture, the smaller the diffraction spreading and thus the better the resolution of a point source. But in order to quantify the resolution of the lens-aperture system, the smallest distance between two diffraction patterns, caused by two point sources, must be found so that they both can be resolved (seen separately). This distance is called the Rayleigh resolution limit and is defined as the distance between the crests of the two diffraction patterns, when the crest of the main lobe of the first one meets the first trough of the second one. It is equivalent to the distance between the crest of the main lobe and the first dark fringe. This lateral resolution is a function of wavelength and numerical aperture.

Because of refraction and reflection phenomena that appear when light passes from the coverslip of the specimen to the objective through a gap of air, it is preferable that an immersion oil (high refractive index medium) is used. This allows light to travel straight towards the objective, leading thus to a larger effective NA . So, the refractive index of the immersion oil, also, plays a role in the final formation of the diffraction pattern.

$$r_{lateral} = \frac{1.22 \lambda}{2n \sin \theta} = \frac{0.61 \lambda}{NA} \quad (2.13)$$

, where $r_{lateral}$ resolution of the lens-aperture system, λ : wavelength of light, n : refractive index of the medium surrounding the point sources, θ : half-angle of the cone of light that enters the lens, NA : effective numerical aperture of the lens-aperture system

A condenser lens is often used so as to focus the illuminating cone of light onto the sample. This has to be computed too. The lateral resolution is now given by:

$$r_{lateral} = \frac{1.22 \lambda}{NA_{obj} + NA_{cond}} \quad (2.14)$$

In a properly configured microscope, the condenser must have equal NA with the objective. So, this leads to the first resolution equation (Eq. 2.13)

DIGITAL RESOLUTION

When it comes to capturing an image and translate it to a digital one, the question of how the resolution is related to the image pixels arises. The image 2D signal in order to be aliasing-free and properly represent the analog true signal needs to be sampled accordingly to the *Nyquist theorem*. The latter states that a signal in general needs to be sample in a rate $f_s > 2f_{max}$, with f_{max} the highest frequency that is wished to be recorded. In an image, frequency has the meaning of periodic changes of luminance of the depicted objects. Thus the corresponding "period" has to do with distance between this changes. The Nyquist sampling rate can be modified to: $D_s < D_{min}/2$, where D corresponds to distance (or size). This gives the imaging sample rate (pixel size) which should be 1/2 the size of the smallest object (resolution) that is wished to be recorded. In practice, an image pixel usually represents distance that is 2.3-3 times smaller than the optical resolution. [21]

Let it be that the sampling process is completed. In order to find the physical distance that is represented by a pixel without knowing the sampling rate, the sensor pixel size and the magnification of the optical system must be known:

$$physical\ distance = \frac{sensor\ pixel\ size}{overall\ magnification} \quad (2.15)$$

2.1.3 Anatomy of an optical microscope

As it was mentioned, this study concentrates on brightfield, fluorescence and confocal microscopy. Brightfield microscopy is achieved using and configuring appropriately an optical microscope. Fig. 2.9 shows the optical train inside a modern optical microscope. Light emanated from a source travels through a system of diaphragms (apertures), plates and lenses in order to be configured in a way that it evenly disperses across the plane of the field of view of the focused specimen. The final stage of this source light-configuring system is the condenser, which focuses the cone of light onto the specimen plane. Then, the re-emitted light from the sample travels through the objective-eyepiece or/and the objective-camera sensor system. Focus knobs are used, as the name implies, to adjust the microscope tube or the specimen stage for proper focusing. The coarse focus knob adjusts in the centimeter range, whereas the fine focus knob adjusts in the micrometer range. There are also knobs for the adjustment of the desired field of view of the sample.

2.1.4 Fluorescence Microscopy

A *fluorescent microscope* is a specialized optical microscope. Because specimens are self-illuminated by internal light (fluorescence), they can be seen against a dark background. So, due to the enhanced contrast, it is easier for the human eye to see details not visible in a brightfield microscope. For the latter, there exist ways of being converted to a fluorescent microscope with the use of specific accessories.

When specimens, living or non-living, organic or inorganic, absorb and subsequently re-radiate light, the process is described as *photoluminescence*. If the emission of light persists for up to a few seconds after the excitation energy (light) is discontinued, the phenomenon is known as *phosphorescence*. *Fluorescence*, on the other hand, describes light emission that continues only during the absorption of the

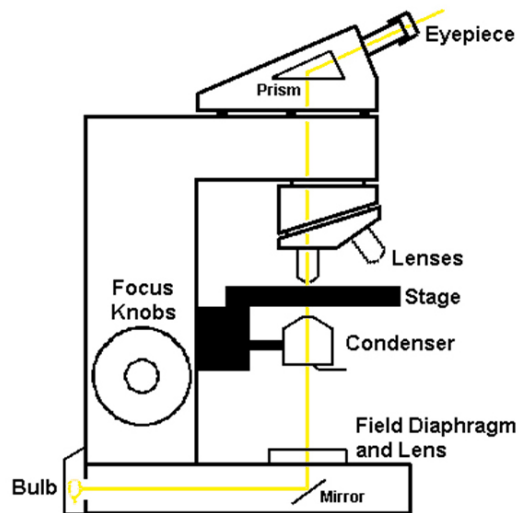


FIGURE 2.9: Basic parts of a typical optical microscope
 Source: <http://www.doctorc.net/Labs/Lab2/lab2.htm>

excitation light. The time interval between absorption of excitation light and emission of re-radiated light in fluorescence is of extraordinarily short duration, usually less than a millionth of a second.

BASIC CONCEPT OF A FLUORESCENCE MICROSCOPE

For each fluorescent substance, there is a certain range of wavelengths that cause its stimulation. After the absorption of the excitation light, the substance emits light of longer wavelength which is finally captured. In order to illuminate the specimen with the wavelength band which excites it, an *excitation filter* is placed right after the light source. Similarly, in order to observe the re-emitted fluorescent light, an *emission filter* is placed right before the eyepiece or the camera sensor. These filters are termed *barriers*, since they block by absorption the unwanted light. Due to the epi-illumination fluorescence microscope design, there must be a specialized filter that will reflect the excitation light towards the specimen and will allow re-emitted light to pass through it. Such a filter is named a *dichroic mirror* or else a *dichromatic beam-splitter*. Reflection occurs via destructive and illuminance-reducing interference with alternating layers of high and low refractive indices, whereas transmission happens via constructive and reinforced interference with the layers. For this reason, such filters belong to the family of *interference filters*. Specifically, successive layers of dielectric materials, with thickness values ranging between one-quarter and one-half of the target wavelength consist the main body of these filters. In many of the current epi-illumination fluorescence microscopes, the excitation, emission filters along with the dichroic mirror are altogether incorporated into a single *fluorescence filter cube*. The whole design of the microscope is epigrammatically shown in Fig. 2.10 and is termed widefield epi-illumination fluorescence microscope. [2]

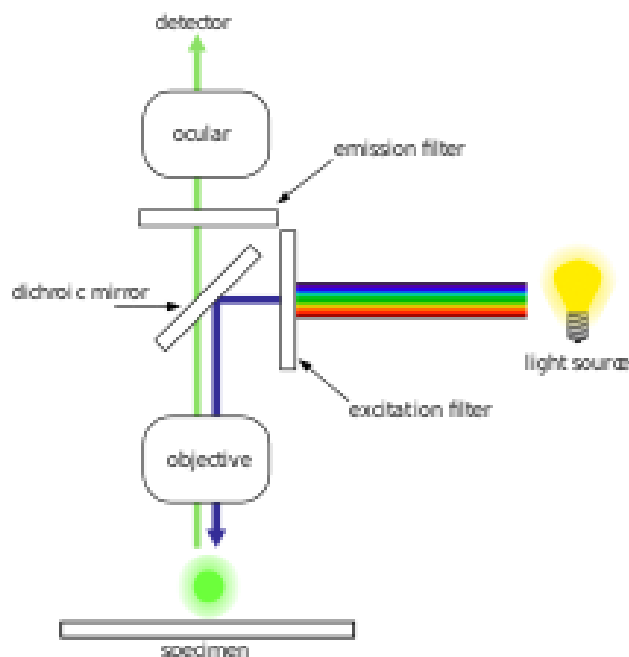


FIGURE 2.10: Widefield epi-illumination fluorescence microscope schematic

Source: https://en.wikipedia.org/wiki/Fluorescence_microscope

FLUORESCENCE

[11] Fluorescence may be exhibited naturally by some materials or biological structures (*autofluorescence/primary fluorescence*) as well as exhibited by artificially added fluorescent markers (*secondary fluorescence*). Fluorescent molecules are also called *fluorescent probes*, *fluorochromes* or simply *dyes*. When they are conjugated to a larger macromolecule, through absorption or covalent bonds, they are termed *fluorophores*. Thanks to this attachment, the distribution of the corresponding macromolecule of a fluorophore can be observed.

Due to heat transfer within fluorophores or interactions between fluorophores and other molecules, the re-radiated light has less energy than the absorbed light. So, the emitted light has a longer wavelength than that of the excitation light. This difference between the maxima of the excitation-emission bands is termed as *Stokes shift*. Typically, the emission band is a mirror of the excitation one. In general, fluorescence investigations are conducted in the range of ultraviolet to visible spectrum (250 – 700 nm).

The distribution of electrons and the overall molecular geometry can be determined by *electronic states*. Several different electronic states exist, depending on the total electron energy and the symmetry of various electron spin states (paired or unpaired spins - opposite or same spins in an orbital). The number of unpaired electron spins in an electronic state defines the state name in the numeration form of singlet, doublet, triplet etc. The ground state of most organic molecules is an electronic singlet, that is no electron spins are unpaired. The excitation process has no effect in changing the spin-pairing, hence the excited states are singlets too. Each electronic state is further subdivided into *vibrational* and *rotational* states associated with the atomic nuclei and the bonding orbitals. In fluorescence, various transitions are taking

place through different paths among energy levels. Transitions involved in absorption and emission of light by a fluorochrome can be shown in a *Jablonski energy diagram* (Fig. 2.11).

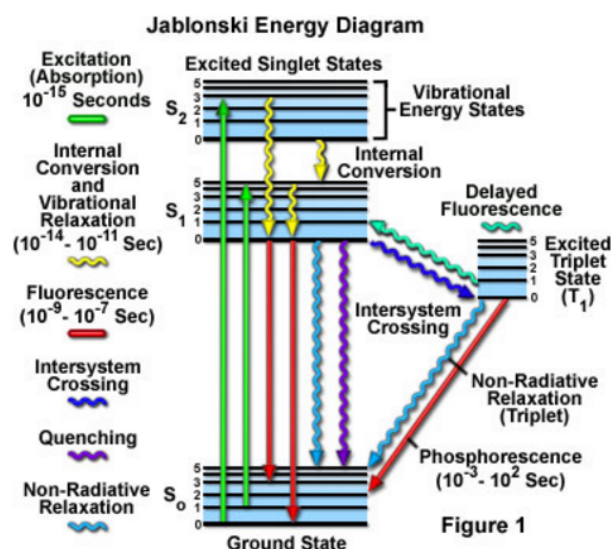


FIGURE 2.11: Jablonski energy diagram showing transitions involved in absorption and emission of light by a fluorochrome. Straight lines show absorption or emission of a photon, whereas wavy lines show non-radiative processes.

Source: <http://www.olympusmicro.com/primer/techniques/fluorescence/fluorescenceintro.html>

Absorption leads the molecule to an excited singlet state depending on the energy of the incident photon which has to be at least equal to the corresponding energy of an excited state. This takes place "instantly", in approximately a femtosecond. Afterwards, several processes will occur with varying probabilities. The most likely will be non-radiative relaxation to the lowest vibrational energy level of the first excited state. This is the *vibrational relaxation* which can happen directly or through an *internal conversion* process. From this point forward, many paths can be taken. One is the desired *fluorescence emission* which is usually accompanied by transitions to higher vibrational energy levels of the ground state. Other roads are energy dissipation non-radiatively as *heat* or energy transfer due to molecules collision (i.e. *quenching*) or transition to an intermediate triplet excited state at its lowest vibrational state. The latter transition is known as *intersystem crossing*, again with no radiation. From that point, excitement back to the higher-energy singlet state might occur, resulting in a *delayed fluorescence* after a radiative relaxation. The other possibility is relaxation to the ground state, even though transition from an excited triplet state to the ground singlet state is forbidden. It might happen again in the form of heat, but also with the emission of a photon, which is termed *phosphorescence*. Because of this forbidding law, phosphorescence is very rare, with a probability of several orders of magnitude lower than that of fluorescence.

Considering the aforementioned different transition paths, it is clear why fluorescent light is of longer wavelength than that of the absorption light, justifying the Stokes shift. Bearing energy of light is inversely proportional to the wavelength of it. Specifically, radiative relaxations are of high probability when they start from

the lowest vibrational state of the first excited state and when they culminate in the highest vibrational state of the ground state. Hence, the emission energy leap is much smaller than the absorption energy leap. Contributing factors to this phenomenon are heat conversions, resonance energy transfer (RET) and quenching processes. In RET, energy is transferred with non-radiative long range dipole-dipole interactions between fluorophores. In quenching, energy might be transferred through collisions between fluorophores and other molecules (usually oxygen, halogens and amines) that are translated as coupling of electronic orbitals between the interacting molecules. Also, formation of non-fluorescent complexes can reduce the population of active excitable molecules, thus limiting the absorption of incident light.

Another unwanted phenomenon, regarding energy and intensity loss, is *photo-bleaching*. Fluorochromes can lose the ability of fluorescence permanently due to long exposition to high intensity light which cause chemical destruction to them.

In general, the decay of fluorescence intensity as a function of time in a uniform population of molecules excited with a brief pulse of light is described by an exponential function:

$$I(t) = I(0) e^{-t/\tau} \quad (2.16)$$

, where $I(0)$: initial fluorescence intensity, τ : time in which fluorescence intensity falls in $1/e \approx 37\%$ of $I(0)$

The exact decaying degree depends on the particular fluorochrome. In addition to this, other parameters are also used to describe and compare different fluorochromes:

- *Extinction coefficient*: Ability of light to absorb light. Those chromophores that have a high extinction coefficient also have a high probability of fluorescence emission, in the expense though of their intrinsic lifetime (below).
- *Quantum yield*: Gauge of the efficiency of fluorescence emission. It describes the probability that an excited molecule will end up in emitting a photon, either through a direct or a delayed fluorescence process.
- *Fluorescence lifetime*: The characteristic time that a molecule remains in an excited state prior to returning to the ground state.

2.2 Point Spread Function

Fig. 2.8 shows the formation of a diffraction pattern on the sensor plane. Because this pattern is the spreaded light initially emanated from a point source, it is given the name Point Spread Function (PSF). The term "function" is valid because the spreading, as it was said, depends on the NA of the lens-aperture system, the refractive index of the immersion oil (if it exists) and the λ of the source light.

By simulating the single-slit phenomenon in a computer, the PSF can be visualized. Using 2,3 and 9 in-phase wavelets of the Huygens-Fresnel model (Fig. 2.12), it can be shown how a PSF is formed across the aperture-sensor plane space. As long as there is no finite number of wavelets, also a simulation of "infinite" ones is shown in Fig. 2.13

The resolution on the image plane (lateral resolution) is given by Eq. 2.13. The tiniest discernible distance in the optical axis (depth axis) is larger than the lateral one. It can be computed by:

$$r_{axial} = \frac{2\lambda n}{(NA)^2} \quad (2.17)$$

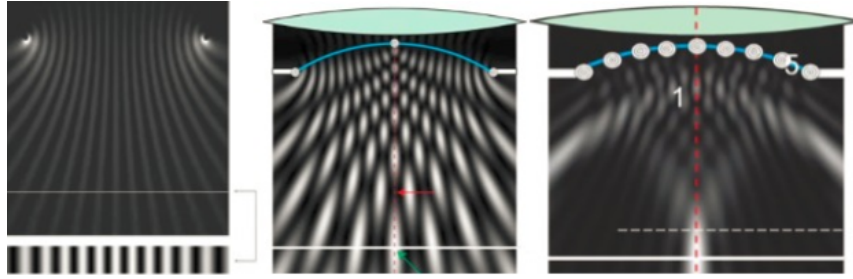


FIGURE 2.12: PSF formed by 2,3 and 9 wavelets of the Huygens-Fresnel model

Source: Youtube: "iBioEducation" channel - "iBiology Microscopy Course" - "Microscopy: Point Spread Function (Jeff Lichtman)" - video snapshots

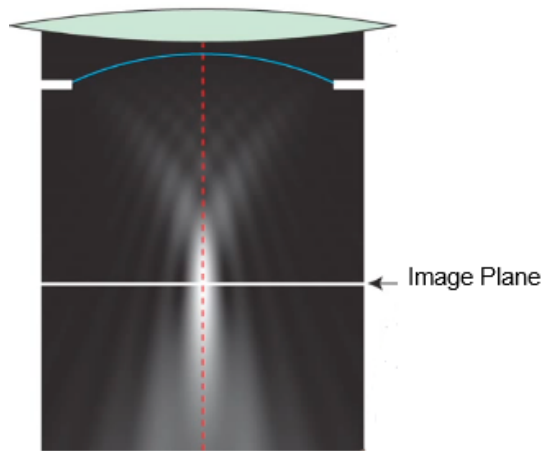


FIGURE 2.13: PSF formed by "infinite" wavelets of the Huygens-Fresnel model. The hourglass-like shape of the PSF in the center defines the detail in which the point source is resolved. The red dotted line is the optical axis along which the light travels

Source: Youtube: "iBioEducation" channel - "iBiology Microscopy Course" - "Microscopy: Point Spread Function (Jeff Lichtman)" - video snapshots

This leads to the same conclusion as for the lateral resolution. That is, the shorter the λ or/and the larger the NA , the better the axial resolution.

The PSF can either be calculated theoretically by various models or be measured experimentally.

2.2.1 Theoretical PSF

Taking into account how the wave fronts of light interfere with a propagation medium, a mathematical expression can be built gradually [12]. This expression will be in terms of wave amplitude and phase as a function of the 2D coordinates of the propagating wave of light at a specific, perpendicular to the optical axis, plane z (depth plane). The emission of waves from a point source can be seen as an input impulse:

$$u_0(x, y) = A_0 \delta(x, y) \quad (2.18)$$

, where A_0 : initial wave amplitude of the emitting source of light

At first, light travels in free space meaning no lenses or apertures are included. The free-space system has an impulse response, let it be $h(x, y; z)$. Thus, the output wave amplitude of this system at the depth plane z_0 just before the lens, will be:

$$u(x, y; z_0) = h(x, y; z_0) * A_0 \delta(x, y) = A_0 h(x, y; z_0) \quad (2.19)$$

, where $*$ is the convolution operation sign

The affected transmission of light through the lens-aperture system of focal length f can be described with a pupil function which captures every optical aberration in the amplitude and phase that takes place between the object focus plane and the image plane. These aberrations [10] (deviations from the ideal optical path) happen due to irregularities or misalignments in any component of the imaging system light path, especially the objective lens but also other lenses, mirrors, filters or apertures. Such aberrations are present in various forms. Speaking about rays of the same wavelength: *Astigmatism*, where rays that propagate in two perpendicular planes, have different focal spots. *Coma*, where slanted parallel rays entering a lens, eventually focus on different spots on the image 3D space. *Defocus*, where rays do not focus on the a priori designed focal spot. *Chromatic aberration*, where rays of different wavelengths have different focal spots. *Spherical aberrations*, where rays from different points across the lens, focus on different spots of the optical axis. *Distortion*, where a rectilinear object eventually appears curved. These aberrations can be integrated to a scale-causing factor as for the wave amplitude. Thus an ideal lens-aperture system will have a scaling factor of 1 for every point of the pupil plane. Possible deviations will cause the scaling factor to diminish. Consequently, a pupil function integrates amplitude and phase factors, thus making it a complex function:

$$P(x, y) = p(x, y)e^{j\Phi(x, y; f)} \quad (2.20)$$

So, the wave fronts equation when light enters the free-space just after the exit of the lens becomes:

$$u'(x, y; z_0) = A_0 h(x, y; z_0)p(x, y)e^{j\Phi(x, y; f)} \quad (2.21)$$

Note: no convolution operation here, as the pupil function plays a scaling role.

Finally, when light reaches the image plane, the free-space impulse response function at the image plane z_1 convolves with the so far computed wave front equation. This leads to the wave function at the image plane which is the 2D PSF (on focus):

$$PSF(x, y) = u'(x, y; z_0) * h(x, y; z_1) = \left(A_0 h(x, y; z_0)p(x, y)e^{j\Phi(x, y; f)} \right) * h(x, y; z_1) \quad (2.22)$$

The above process can be also done in order to compute the wave function in different planes from the image focus plane. Hence, a 3D PSF is formed. In reality, though, a single 3D model is not sufficient to completely describe image formation throughout the 3D object space. This is because PSF is often a function of the location of the point source in the object space. Thus, in reality every point of the object corresponds to a different PSF. A system, the Point Spread Functions of which behave in this way, is called a shift-variant system.

Different approximations can be made, depending on the *nature of diffraction*, the possible consideration of *shift-variance* and the amount and degree of effect of possible *aberrations*, if the latter are taken into account.

Assuming there are no aberrations and that the Fraunhofer approach is valid, a more specific PSF can be built. A pupil function for a circular aperture of radius α through which light is transmitted unaffected has the value 1 inside the area encompassed by the *aperture* in the axes system x',y' . The polar coordinate translation is: $r = \sqrt{x'^2 + y'^2}$ and $\theta = \arctan(y'/x')$

At the *image plane* the axis system (x,y) is translated in polar coordinates as $\rho = \sqrt{x^2 + y^2}$ and $\psi = \arctan(y/x)$.

According to Principles of Optics by Born and Wolf, as stated in [16], the diffraction pattern wave function (amplitude) is the Fourier Transform of the pupil function. From this it follows that:

$$D(x, y) = \int_0^a \int_0^{2\pi} e^{-ikr\rho \cos(\theta-\psi)} r d\theta dr \quad (2.23)$$

, where $k = 2\pi/\lambda$ (wavenumber)

Using the Bessel function of the first kind and order 0, the above equation can be modified as:

$$D(\rho) = 2\pi C \int_0^\alpha J_0(kr\rho) r dr \quad (2.24)$$

, where C: constant

PSF is in terms of intensity of light which is proportional to the squared amplitude of the wave function. So, from the above equation arises that:

$$PSF(\rho) = \left| 2\pi C \int_0^\alpha J_0(kr\rho) r dr \right|^2 \quad (2.25)$$

For an aberration-free and shift-invariant in all directions PSF, the 3D **Born and Wolf** approximation can be useful [5]. The constraint is though, that the observed fluorophore particle is located at the focal plane of the objective lens but right beneath the coverslip. The model is expressed in the Kirchhoff's diffraction integral formula as:

$$PSF(x, y, z) = \left| \int_0^1 J_0 \left[k \frac{NA}{n_i} \sqrt{x^2 + y^2} \rho \right] e^{-\frac{1}{2}jk\rho^2 z \left(\frac{NA}{n_i} \right)^2} \rho d\rho \right|^2 \quad (2.26)$$

, where PSF: scalar, J_0 : Bessel function of the first kind of order 0 (Bessel function appear in problems of wave propagation), k : wavenumber of the emitted light in vacuum ($k = 2\pi/\lambda$), n_i : refractive index of the immersion oil

The **Gibson and Lanni** PSF model takes into consideration the consequences of the optical path modifications that occur when light rays follow trajectories other than that for which the optics were designed. It integrates the optical path difference (ODP), which is the difference between ideal trajectories and real trajectories, taking into account parameters determining path fluctuation: thickness (t_{oil}) and refractive index (n_{oil}) of the immersion oil, thickness (t_g) and refractive index (n_g) of the coverslip and the thickness (t_s) and refractive index (n_s) of the sample.

Any deviation of any of these parameters from the optimal values for which the optics were designed will cause *spherical aberrations*. The resulted prolonged focus

spot has the effect of an assymetry in the 3D PSF on the depth axis. In the case of microscopy, this is a common phenomenon which increases as the object focal plane moves deeper into the sample, thus inducing more refractive index mismatches inside the sample as well as between the sample, the coverslip and the immersion medium. Spherical aberration is the reason why PSF is shift-variant on the depth axis.

As for the Gibson and Lanni model, it incorporates shift-variance only in the depth axis. It can be seen as a generalization of Born and Wolf in the sense that the fluorophore particle can be located at any depth within the sample. It also considers three optical layers (sample-coverslip-immersion) instead of two (glass-immersion). The model description again in the Kirchhoff's diffraction integral formula is:

$$PSF(x, y, z) = \left| \frac{C}{z_d} \int_0^1 J_0 \left[k\alpha\rho \frac{\sqrt{x^2 + y^2}}{z} \right] e^{jW(\rho)} \rho d\rho \right|^2 \quad (2.27)$$

, where PSF: scalar, C : a normalizing constant, z_d : tube lens-detector distance, $W(\rho)$: phase aberration induced:

$$W(\rho) = k \left\{ n_s t_s \sqrt{1 - \left(\frac{NA\rho}{n_s} \right)^2} + n_g t_g \sqrt{1 - \left(\frac{NA\rho}{n_g} \right)^2} + n_{oil} t_{oil} \sqrt{1 - \left(\frac{NA\rho}{n_{oil}} \right)^2} \right. \\ \left. - n_g^* t_g^* \sqrt{1 - \left(\frac{NA\rho}{n_g^*} \right)^2} - n_i^* t_i^* \sqrt{1 - \left(\frac{NA\rho}{n_i^*} \right)^2} \right.$$

2.2.2 Experimental PSF

Prediction of all the various phenomena that take place in the optical train is proved to be a complex problem. Thus, the existing theoretical PSF models do not integrate every optical path deviation from the ideal path. The problem of diffraction pattern formation was examined using the concept of point sources of light. In fact, this is abstract, since there cannot be an infinitely small object. However, from the concept of optical system resolution, it follows that a sub-resolution object can be considered as an infinitely small object. Hence, depicting such an object, a real PSF can be built, which incorporates all optical train defects.

For that reason, several methods have been proposed, such as using quantum dots and fluorescent microbeads. *Quantum dots* are semiconductor particles with size of some nanometres that emit light of specific frequencies if electricity or light is applied to them. The disadvantage, though, is that good preparations of these are hard to obtain as they easily form aggregates, thus not being "single points" anymore.

[15] *Fluorescent microbeads* are of various materials. Even though in theory, they must be as small as they can be, this is impractical because these beads exhibit low Signal to Noise Ratio (SNR) and meagre signal. Thus, they are usually chosen to have size more than half the resolution of the optical system, such as 150 nm. A sufficient fluorescent signal by beads is possible either when they aggregate or when they receive a bigger quantity of excitation light. Big aggregation hinders the determination of a single bead because of the overlap by each single bead diffraction pattern. As for more intense excitation light, this has the danger of causing untimely photobleaching to the beads, thus diminishing their life span. Since the level of the light signal intensity is meagre, photon noise of the bead image capture is very pronounced which means a very low SNR.

2.3 Modulation Transfer Function - Optical Transfer Function

2.3.1 Physical meaning and PSF-MTF-OTF relation

As examined in Seq. 2.1.2 - NUMERICAL APERTURE AND RESOLUTION, the distance between the diffraction pattern crests of the images of two point sources of light, defines the resolution of the optical system. So, expanding this concept to more point sources aligned in a straight line, it is safe to say that the closer to each other they are, the more the corresponding diffraction patterns are overlapped, deteriorating thus the depicted contrast among the point sources. Further expanding to parallel lines of point sources (line sources) in a way that they form bright and dark stripes upon a plane parallel to the image sensor plane (square wave), the same conclusion can be made. The depicted line sources will exhibit an overlap of their diffraction patterns, thus diminishing the contrast among them. Consequently, the imaging lens, camera sensor, and illumination play key roles in determining the resulting image contrast. The lens contrast is typically defined in terms of the percentage of the object contrast that is reproduced. The sensor's ability to reproduce contrast is usually specified in terms of decibels (dB) in analog cameras and bits in digital cameras.

The term *modulation* of Modulation Transfer Function (MTF) is exactly the above-mentioned contrast. How well the optical system can *transfer* this contrast / modulation from the object to the image, is the second term. As for the term *function*, it is so because modulation transfer depends on the particular distance among the aforementioned line sources (to keep the last example) or otherwise the spatial frequency of these line pairs. A line pair is a bright (white) and a dark (black) stripe altogether, mathematically forming a pulse of light. The unit of spatial frequency is line pairs per millimeter or cycles per millimeter (lp/mm or cycles/mm).

To express the contrast percentage of an image of bright and dark stripes, the maximum and minimum intensity values must be used. A full-bright stripe is 1-valued, whereas a full-dark stripe is 0-valued. The contrast expression is given by: [14]

$$\% \text{ Modulation} = \frac{I_{max} - I_{min}}{I_{max} + I_{min}} \times 100 \quad (2.28)$$

Assuming no resolution loss by the optical system, it is clear that the modulation transferred is 100%. That is the optical system reproduces the contrast of the object in its whole 100%.

At a particular spatial frequency, the transferred contrast of an object depends on its off-(optical)axis distance. Specifically, the MTF decreases as the object is farther from the optical axis. Also, as the line pairs per millimeter get more and more, there is a limit where the optical system cannot anymore resolve them. At this point the modulation becomes 0%. The corresponding spatial frequency is the cut-off frequency.

As said above, changes in depicted contrast of an object pattern are described by MTF. Yet, optical system aberrations also cause changes in PSF intensities which in turn result in a linear lateral shift of the object pattern. This pattern-phase shift is described by a function called *Phase Transfer Function* (PTF). Altogether, these contrast changes and phase shifts are incorporated in a complex function called *Optical Transfer Function* (OTF): [18]

$$OTF = |OTF| e^{iPTF} = MTF e^{iPTF} \quad (2.29)$$

OTF can also be defined in terms of PSF, as :

$$OTF(\nu) = \int PSF(x) e^{-i2\pi\nu x} dx \quad (2.30)$$

, where x is the spatial coordinate in the image plane.

This equation implies that OTF is the Fourier transform of PSF. Intuitively, this can be comprehensible and be deduced from the below thinking using only the MTF (no lateral phase shifts of the image pattern): The point source acts like an input impulse to the system, resulting to an impulse response which is the PSF. It is known that, mathematically, in order to build an impulse, "all" frequencies are needed. So, the Fourier Transform of an impulse is a plane wave, integrating infinite frequencies. Ideally, if the PSF was identical to the point source, that plane wave would be the Fourier Transform. But since the PSF is different incorporating a resolution limit, instead of a plane wave, only a range of spatial frequencies will contribute to the formation of the PSF. Yet, these contributing frequencies form the MTF. The upper boundary of this spectrum depends on the above-mentioned resolution limit. As for an ideal aberration-free PSF, the cut-off frequency of its MTF is: $1/2\lambda f$.

2.3.2 Experimental measurement of MTF - slanted edge

Generally, there are 3 ways of measuring a MTF. Either by using a *square wave* as examined in 2.3.1 or by a *sine wave* (smoother changes between dark and bright areas) or by the *slanted edge method*. What is examined below is related to the slanted edge method.

From the aforementioned relation between impulse response and infinite frequencies, it is safe to say that in order to measure what band of spatial frequencies are resolvable by an optical system, its output with an impulse as input must be found. Specifically, the impulse is a 2D signal, allowing thus the imaging measurement of this line profile which it turn gives the *line spread function*. In practice, the theoretical impulse is not directly feasible as it requires zero width and infinite intensity. So, eventually the measurement of the MTF is done indirectly with experimental processes termed *edge-gradient methods*. [7]

Firstly, an *edge profile* is measured. An edge profile is ideally a step function. In the case of images, it is a dark 2D area followed by a bright one, forming thus a "step of light". The reproduced edge is translated through the optical system in a degraded degree. Specifically, there is no immediate change in light intensity from dark to bright, rather a smoother one. So, the acquired image of the edge can be called an *edge spread function* (ESF). The terms edge profile and ESF are used alternately. Then the computation of the discrete first *derivative of the ESF* will give the PSF. Finally, the modulus of the *Fourier Transform of the PSF* will grant the wanted MTF.

The above method can be executed with more than one ways. An edge profile can be taken from picturing a very precisely designed edge for this purpose, thus with no deformations along the edge. As a second way, an edge feature from image data can be captured providing the wanted edge profile. However, this requires a captured edge of sufficiently high optical quality, meaning negligible noise and clear edge details.

Regarding the first approach, in order to capture the edge profile, it must be sampled. As a first thought, the edge can be sampled parallel to the pixel columns of the camera sensor. However, the theoretical resolution of a sensor array is not sufficient to discern the luminance change of the edge with sufficient resolution. There

can be different digitization occasions depending on the sensor. This can be visualized in Fig. 2.14.

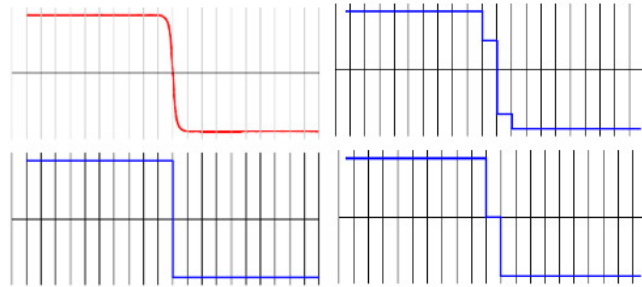


FIGURE 2.14: The true analog ESF (along 1 spatial direction for simplification) (top left) will be digitized but with a quantization error which depends on the number of pixels in the horizontal axis of the sensor and the single pixel size. Top right, bottom left and bottom right show 2, 0 and 1 samples respectively which define the edge.

Source: http://dougkerr.net/Pumpkin/articles/MTF_Slant_Edge.pdf

SLANTED EDGE PRINCIPLE

[17] Fortunately, "fake" enhanced resolution of the sensor can be realized by rotating the edge profile (usually by 5 degrees), thus forming an angle between it and the pixel grid (Fig. 2.15).

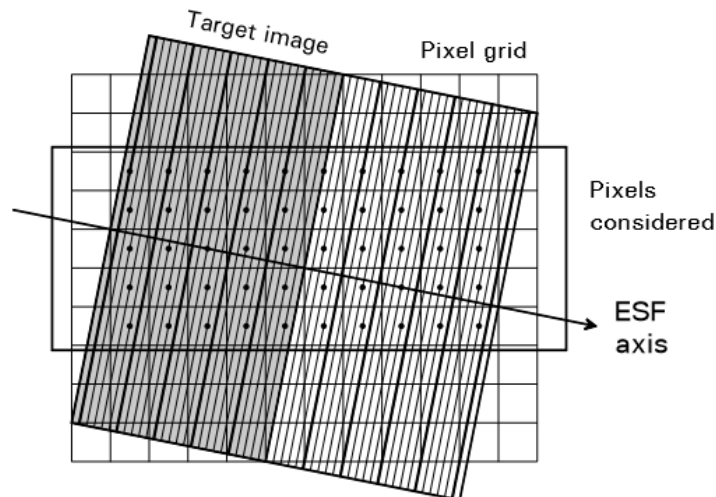


FIGURE 2.15: Every center a pixel is assumed the role of a sample of the ESF

Source: http://dougkerr.net/Pumpkin/articles/MTF_Slant_Edge.pdf

Since every evenly spaced vertical line, parallel to the edge, has the same luminance, it can be observed that every center of a pixel is assumed the role of a sample of the ESF. Hence, this "trick" provides a much better sampling of the ESF. By applying trivial trigonometric equations: Spacing of ESF samples = pixel pitch $\times \sin(a)$, where a is the angle of rotation of the edge profile. So, the smaller the pixel pitch and the angle are, the better the sampling is. Because, though, the pixel detectors

actually do not pick up the luminance at a point (dots in the example of Fig. 2.15), but rather respond to an average of some sort over a region (bin) approaching the domain of the pixel, certain special steps have to be taken in the evaluation of the ESF from the set of collected pixel detector values (examined below).

STANDARDIZED MTF EVALUATION METHOD

The whole process of measuring the MTF is standardized by the ISO 12233 and implemented by little or no modifications to the latter: [7]

- *ROI identification:* First, the region of interest (ROI) (m lines, n pixels) surrounding the edge is selected. The luminance from each RGB photosensor of the ROI is measured (a pixel consists of 1 red 2 green and 1 blue photosensors).
- *OECF transformation:* The image data are transformed with an opto-electronic conversion function (OECF). This function is a relationship between input luminance and digital output levels for an opto-electronic digital image capture system.
- *Luminance record computation:* A luminance array is computed as a weighted sum of red, green, and blue image records at each pixel.
- *Derivative of each data line:* The 1D discrete derivative of each line along the horizontal axis of the sensor is taken. In that way, the edge location and direction can be estimated. Note: the derivative of each line gives the 1D PSF which with the rest PSFs form the LSF.
- *Centroid computation for each line:* The centroid of a straight 1D line is actually its middle point. It is a translation of the line "weight". When, though, each point of the line has an intensity integrated to it, the centroid is found in a different point along the line depending on the intensity distribution. In the case of a first derivative of a line, the centroid is located upon or near the spike of the derivative.
- *Linear fit of the centroids:* In order to define the slanted edge, all the locations of the centroids are fitted with a linear equation.
- *Projection of the image data along the edge direction:* As stated in the SLANTED EDGE PRINCIPLE of this subsection, each pixel or more precisely each element of the luminance arrays, plays the role of a sample for the ESF. So, with a linear fit to line, a 1D "super sampled" ESF is formed.
- *Data binning with 1/4 of original sampling rate:* The previous step results in a $4x$ oversampling. At this step, a binning process (replacing of each 4 samples with a value that represents them) is done with a $1/4 x$ sampling rate.
- *Derivative of ESF and windowing:* This grants the LSF.
- *Fourier transform of LSF:* A discrete FT of the LSF (1D LSF = PSF) gives the OTF, as examined in 2.3.1.
- *Modulus of OTF and normalization:* As the wanted MTF describes a percentage of modulation transfer, the modulus of the OTF must be normalized in range 0-1.

2.4 Image formation and deblurring technologies

2.4.1 Sources of image degradation

Through different stages in the opto-electronic digital image capture system, many aspects of unwanted noise are introduced. The sources of degradation to the image can be classified as: [22]

- *Photon shot noise*: Due to the particle nature of light and the irregular distribution of photons among the pixels, some fluctuations of photon events occur. This is heavily observed when the light of the environment of the object is of low intensity. Random arrivals of photons can be modeled with Poisson distributions.
- *Thermal noise*: Electronics of the imaging system while in operation cause thermal agitation of electrons that were previously at equilibrium. This results in faulty pixel electron charge measurements. The random activation of electrons due to heat can be modeled with Gaussian distributions.
- *Scatter*: Specimens with high heterogeneity of refractive indices cause a scattering of light that because of its intrinsic complexity cannot be predicted and therefore to be modeled. Scatter increases as specimen thickness.
- *Glare*: Imperfections or misalignments of the components across the optical train cause a glare effect that can be corrected with material and alignment improvement.
- *Blur*: Diffraction phenomena put a limit in image resolution. So, when an optical system magnifies an object close to its intrinsic resolution, a blurred version of the true object is observed. Also, blurring happens when light from out-of-focus parts of the sample is recorded on the image plane and/or light from adjacent areas mix among each other. This form of noise is independent from the above-mentioned types of degradation. Blur removal is possible with the use of deblurring techniques.

Currently used microscopy technologies are targeted in different aspects of blur removal. One target is the eradication of effects related to diffraction phenomena or more specifically the improvement of the Airy disk so as to have a smaller radius and the surrounding diffraction pattern so as to exhibit ripples of lower intensity. This goal has been achieved by the nobel-awarded *Super Resolved Fluorescence Microscopy* technologies. They allow images to be taken with a higher resolution than the diffraction limit of an optical microscope, enhancing the resolution from 200 nm to 100 nm. Two different methods accomplish the super resolution goal; Stimulated Emission Depletion Microscopy (STED) and Single-Molecule Microscopy, just for mention.

The other target is the removal of defocused light from the focused image and of superpositioned light from on-plane neighboring areas. For this goal there exist two solutions: *Confocal Microscopy* and *Deconvolution Microscopy*.

2.4.2 Deblurring technologies

CONFOCAL FLUORESCENCE MICROSCOPY

[20] The basic element of a fluorescence confocal microscope is a pinhole that is placed before a light detector (i.e. photomultiplier tube or PMT). This pinhole allows only light coming from planes very close to the focal one to pass through. The advantage arising from this is that lateral as well as axial resolution are enhanced. One disadvantage is though, that blocking a significant percentage of the incoming cone of light leads to low signal intensity. This can be solved by long exposures to fluorescent light. However, this has the danger of quicker photobleaching, thus allowing less time for fluorescence observation as well as phototoxicity phenomena. The latter incorporate the toxic danger of some fluorochromes when they are attached to cells under study. Light activates some processes within the labeled cells that eventually compromise them entirely and damage their subcellular components. This danger increases as fluorochromes are repeatedly or heavily exposed to light.

WIDEFIELD FLUORESCENCE DECONVOLUTION MICROSCOPY

[22] An alternative way to remove the out-of-focus light is to record images at a series of focal planes using a widefield microscope and then use a detailed knowledge of the imaging process to correct it by computer image processing. Apart from defocused light, superpositioned light from on-plane neighboring areas has a blurring effect across this single plane. This happens since PSFs of adjacent points on a plane mix with each other. Fortunately, altogether the defocused and the on-plane superpositioned light can be restored back to their area of origin. Restoration has the meaning of reversing the process of blurring and ultimately the effect of the PSF on the image (either on a 2D or a 3D image).

The image of an object can be divided in individual areas. Through the linearity property of optical systems, the image of all the individual areas is equal to the ensemble of the images of each area separately. This means that:

$$\begin{aligned} \text{Image}(\text{object}) &= \text{Image}(a_1 + a_2 + \dots + a_n) \\ &= \text{Image}(a_1) + \text{Image}(a_2) + \dots + \text{Image}(a_n) \end{aligned}$$

, where a corresponds to a particular individual point.

Since, it is known that the depiction of an individual area of a particular luminance is spreaded by the weights of the PSF of the optical system and assuming a shift-invariant PSF, it can be deduced from the above equation that:

$$\begin{aligned} \text{Image}(\text{object}) &= \sum_{A_1} a_1 \odot PSF + \sum_{A_2} a_2 \odot PSF + \dots + \sum_{A_n} a_n \odot PSF \\ &= \mathbf{a} * PSF \end{aligned}$$

, where \odot : element-wise multiplication, \mathbf{a} : vector consisting of all the 'a' areas of the image, $*$: convolution operation sign, A_k : number of elements of a_k area; same size as PSF.

Thus, the convolution result y (with an omnipresent noise) of a true underlying fluorescent signal x with the PSF h is given by:

$$y = h * x + n \quad (2.31)$$

, where the images and the noise are represented by matrices.

So, in order to reverse as said the above process of the convolution of the object with the PSF, a de-convolution process must be realised. Deconvolution methods vary, as deconvolution is not just a simple step back to the original underlying image of the object to be depicted. These methods are computationally complex to some significant degree and so a trade-off between restored image quality and time consumed to produce it has to be determined.

Brief explanation of convolution: Let it be two matrices x and y . x will be convolved with y and the result will be z . y has to be at most the size of x . The operation is as follows: y matrix or else the convolution kernel "scans" x in a top to down and left to right direction. This "scan" is defined as the element-wise multiplication of x and y elements and the assignment of the sum of the multiplications to the central element of the sub-matrix of z that is scanned at that moment.

The discrete convolution is mathematically defined as:

$$y[\mathbf{p}] = (x * h)[\mathbf{p}] = \sum_{\mathbb{N}^3} x[\mathbf{r}]h[\mathbf{p} - \mathbf{r}] \quad (2.32)$$

, given at a 3D location $\mathbf{p} \in \mathbb{N}^3$

The above equation can be transformed via notation of linear algebra into a more easily read one:

$$\mathbf{y} = H\mathbf{x} + \mathbf{n} \quad (2.33)$$

, where \mathbf{n} : additive noise

, \mathbf{x}, \mathbf{y} : vectors corresponding to true and observed image respectively. For a 2D image a vector consists of the concatenation of the image rows.

, H : circulant matrix corresponding to the convolution operation.

It is not needed to examine further this concept of the convolution with a circulant matrix, since for deconvolution of large or a big group of images it is way too time-consuming for realistic applications.

Instead, the discrete FT of the Eq. 2.31 is used mostly in the deconvolution algorithms due to higher speed of computation and less used memory compared to non-FT solutions:

$$\hat{Y} = \hat{H} \odot \hat{X} + \hat{N} \quad (2.34)$$

, where the capital letters indicate the corresponding Fourier Transforms. Note: FT of a convolution in the spatial domain gives element-wise multiplication in the frequency domain.

As Fourier analysis states, a periodic signal is considered an infinite sum of sines and cosines of different harmonic frequencies with each sine and cosine contributing with varying amplitude. This can be extended to non-periodic signals, assuming their period is allowed to reach infinity. So, generally FT gives all the frequencies that contribute in building the original signal. In that notion, there exist another

transform that uses signals limited in time and frequency, which are termed wavelets, in order to decompose a signal to its contributing wavelets. This transform is called *Wavelet Transform*. When a wavelet transform is executed, one wavelet from a wide family of wavelets is used. The used wavelet is scaled in time in order to handle higher or lower frequencies of the signal to be decomposed. Wavelet Transforms are used in the algorithm explained at the end of this section (FISTA).

Thinking about solutions to the deconvolution problem, the first thing that comes to mind is to modify Eq. 2.33 (assuming the noise power is low) as $\mathbf{x} = H^{-1}\mathbf{y}$. This naive approach is proved not to work. The reason is that the inverse problem of deconvolution is known to have a high condition number (rendering it an ill-conditioned problem) which means that a small error in the input causes a big error in the output. This means that from a set of observed images with little differences among them, the estimated "true" images of each observed one will differ significantly. Specifically, the explicit solution is a poor choice since it is sensitive to any noise in the observed image. From the above, it occurs that there is no single solution to the naive inverse deconvolution method.

Thus, the best solution is to find the estimate which provides the best approximation of the true image. To know if a good estimate has been found, the deconvolved image is convolved again with the PSF and it is expected the difference of the observed image with the re-convolved image estimate to be infinitesimal in some way. This difference can be computed in many ways which will be examined in the next chapter.

Generally, the best estimate minimizes a cost function which corresponds to the aforementioned difference or otherwise residual:

$$\mathcal{C}(x) = \|y - Hx\|^2 \quad (2.35)$$

Continuing with the FT-form of the cost function, the $\underset{x}{\operatorname{argmin}} \mathcal{C}(x)$ is to be found, or else the x that makes the first derivative of the cost function to be zero.

It is true that:

$$\mathcal{C}(x) = (y - Hx)^T (y - Hx) = y^T y - x^T H^T y - y^T Hx + x^T H^T Hx \quad (2.36)$$

, where T denotes the transpose matrix.

From this it follows that:

$$\frac{\partial \mathcal{C}(x)}{\partial x} = 0 \Rightarrow x = H^{-1}y \quad (2.37)$$

or in the Fourier domain:

$$\hat{X} = \frac{\hat{Y}}{\hat{H}} \quad (2.38)$$

As it can be seen, this solution corresponds to the aforementioned naive solution, but in the frequency domain. Since, the FT of the observed image is divided by the FT of the PSF which may contain close to zero elements, it is very probable for the estimate to exhibit very large values, thus resulting in amplifying the already

existing noise. A better approach is to add some constraints (regularization) in the cost function which helps easing noise amplification problem.

All the algorithms explained below are in agreement with [15] and [9].

TIKHONOV REGULARIZATION (TRIF)

The cost function is modified as:

$$\mathcal{C}(x) = \|y - Hx\|_2^2 + \lambda \|x\|_2^2 \quad (2.39)$$

, where λ is the regularizing parameter that balances the contribution of the two terms and penalizes absolute high values of the solution. It consists a trade-off between data fidelity and regularization, since transition in absolute high values might be image details as well as noise. So, higher λ gives a smoother image. Minimization of such a problem (where more than one unknown terms appear) can be solved with Lagrange multipliers. The **solution** is given by:

$$x = (H^T H + \lambda \mathbf{I})^{-1} H^T y \quad (2.40)$$

, where \mathbf{I} is the identity matrix.

This can be expressed in the Fourier domain as:

$$\hat{X} = \frac{\overline{\hat{H}} \hat{Y}}{\hat{H} \hat{H} + \lambda \mathbf{1}} \quad (2.41)$$

, where $\overline{\hat{H}}$ denotes the conjugate of \hat{H} and $\mathbf{1}$ is a matrix of ones. When equations refer to the frequency domain, \odot is omitted for simplification.

REGULARIZED INVERSE FILTERING (RIF)

This method uses a cost function that when minimized it imposes smoothness on the estimate. That is accomplished by penalizing high values of the 2^{nd} derivative of \hat{X} . That is, the cost function becomes:

$$\mathcal{C}(x) = \|y - Hx\|_2^2 + \lambda \|Lx\|_2^2 \quad (2.42)$$

, where L is a differential operator, like the Laplacian operator ∇^2 .

Differentiation of an image acts as a high-pass filter, so minimization also of the 2nd term of the $\mathcal{C}(x)$ ends up in a smoother solution. But yet again, the "amount" of smoothness imposed, depends on λ . Again the method of Lagrange multipliers gives the **solution**:

$$x = (H^T H + \lambda L^T L)^{-1} H^T y \quad (2.43)$$

In the Fourier domain, this is expressed as:

$$\hat{X} = \frac{\overline{\hat{H}} \hat{Y}}{\hat{H} \hat{H} + \lambda \hat{L} \hat{L}} \quad (2.44)$$

Note: this FT solution gives a generalization of the classic Wiener filtering solution. To derive Wiener filtering solution, λ is defined as $1/\sigma_n$, with σ_n the noise variance. Also $L^T L$ must impose a whitening transformation on x .

WIENER FILTER

The Wiener filter integrates an estimated Noise-to-Signal power ratio (NSR). The **solution** is expressed as:

$$\hat{X} = \frac{\overline{\hat{H}}\hat{Y}}{\hat{H}\hat{H} + NSR} \quad (2.45)$$

CONSTRAINED ITERATIVE ALGORITHMS

Inverse filtering algorithms suffer from sensitivity to the PSF. Small errors in the estimation of the PSF may result in major artifacts in the solution. An alternative to this, is the option of iterative methods. They minimize a residual/cost function as well as inverse algorithms do, but by generating a series of improving approximate solutions. Often, the Wiener Filter solution is used as the initial guess. The advantage of them in contrast to the inverse solutions is that estimates exhibit *better stability and less sensitivity to errors of the PSF*. The disadvantage is though, that they are computationally intense.

LANDWEBER (LW)

This algorithm minimizes the unregularized $\mathcal{C}(x) = \|y - Hx\|^2$ using the iterative *gradient descent approach*. More specifically, one way to find the local minimum of a general function $F(x)$ starting from a particular point a , is to iteratively take steps proportional to the negative of the gradient of the function at the current point. This is because $F(x)$ decreases faster if we move against the direction of $\nabla F(a)$

So, starting with a and with b being the next point closer to the local minimum of $F(x)$ (or global if $F(x)$ is convex), we reach b via: $b = a - \gamma\nabla F(x)$, with γ being the step size or relaxation factor describing the speed of convergence of this method.

Thus, this can be expanded to more iterations and with an initial guess x_0 and the sequence $x_0, x_1, x_0, \dots, x_n$ we take the gradient descent general solution:

$$x_{n+1} = x_n - \gamma_n \nabla F(x_n), \quad n \geq 0 \quad (2.46)$$

The importance of the γ step size can be explained with the concept of the level sets. A level set is a set where the function takes on a given constant value. This can be visualized in Fig. 2.16. In the center, the minimum of the function resides. In this case, the wider the “circle”, the bigger the value of the function. So, taking little steps each time against the derivative of the function in a point of a “circle”, directs us to the minimum in the center. Here, we can see that the size of the step plays an important role, in the issue of convergence to our solution. Specifically, A small step-size guarantees convergence, but leads to very slow convergence, meaning more time to reach the center. On the other hand, A big step leads to faster but less stable convergence (more like circling around the center).

To continue with the gradient descent solution the gradient of $\mathcal{C}(x)$ must be computed.

$$\nabla \mathcal{C}(x) = -H^T y + H^T H x = -H^T (y - Hx) \quad (2.47)$$

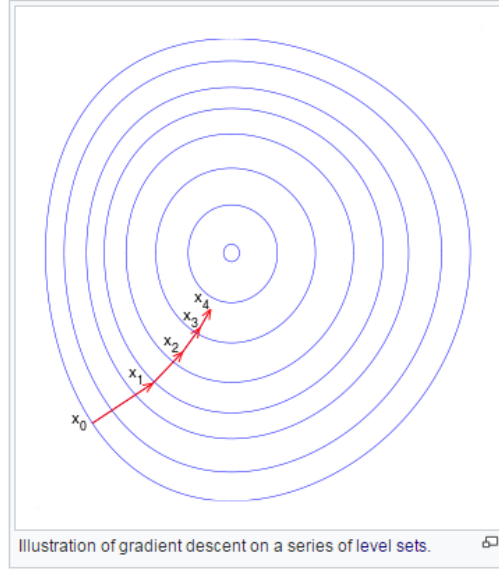


FIGURE 2.16

Source: https://en.wikipedia.org/wiki/Gradient_descent

The same applies for vector functions, so substituting the gradient in the Eq. 2.46 gives:

$$x_{n+1} = x_n + \gamma H^T (y - Hx), \quad 0 < \gamma < 2/\sigma_1^2 \quad (2.48)$$

, where σ_1 the largest singular value of H , that is $\sqrt{\lambda_{\max}(H^T H)}$

When Fourier Transforms signals are inverted, the spatial-domain result exhibits some overshoots and undershoots, especially in high-contrast areas where the signal drops or rises abruptly. When undershoots happen they may cause the signal to have negative values at some points. For this reason, a non-negative projection must be imposed to the values of the result:

$$\mathcal{P}_{(\mathbb{R}^+)}\{x\} = \max(x, 0) \quad (2.49)$$

Hence, the final form of the solution becomes:

$$x_{n+1} = \mathcal{P}_{(\mathbb{R}^+)}\{ x_n + \gamma H^T (y - Hx_n) \}, \quad 0 < \gamma < 2/\sigma_1^2 \quad (2.50)$$

, where \mathcal{F}^{-1} : inverse Fourier Transform

For the sake of speed, the above equation can be modified as below. In that way, each iteration performs fewer operations. Thus, the **solution** becomes:

$$x_{n+1} = \mathcal{P}_{(\mathbb{R}^+)}\{ Ax_n + G \}, \quad 0 < \gamma < 2/\sigma_1^2 \quad (2.51)$$

, where $A = \mathbf{I} - \gamma H^T H$ and $G = \gamma H^T y$

In the practical form for algorithms, this is expressed as:

$$x_{n+1} = \mathcal{P}_{(\mathbb{R}^+)}\{ \mathcal{F}^{-1}\{\hat{A}\hat{X} + \hat{G}\} \}, \quad 0 < \gamma < 2/\sigma_1^2 \quad (2.52)$$

, where $\hat{A} = \mathbf{1} - \gamma \overline{\hat{H}}\hat{H}$ and $\hat{G} = \gamma \overline{\hat{H}}\hat{Y}$

ITERATIVE CONSTRAINED TIKHONOV-MILLER (ICTM)

ICTM uses iterative gradient descent to minimize the RIF cost function (Eq. 2.42). The gradient of $\mathcal{C}(x)$ is:

$$\nabla \mathcal{C}(x) = -H^T y + (H^T H + \lambda L^T L)x \quad (2.53)$$

Substituting in the gradient descent equation (Eq. 2.46) with projection to \mathbb{R}^+ , gives the ICTM solution:

$$x_{n+1} = \mathcal{P}_{(\mathbb{R}^+)} \{ x_n + \gamma(H^T y - (H^T H + \lambda L^T L)x_n) \} \quad (2.54)$$

As in the LW solution, the ICTM **solution** is modified as:

$$x_{n+1} = \mathcal{P}_{(\mathbb{R}^+)} \{ Ax_n + G \} \quad (2.55)$$

, where $A = \mathbf{I} - \gamma(H^T H + \lambda L^T L)$ and $G = \gamma H^T y$

In the practical form for algorithms, this is expressed as:

$$x_{n+1} = \mathcal{P}_{(\mathbb{R}^+)} \{ \mathcal{F}^{-1} \{ \hat{A} \hat{X} + \hat{G} \} \} \quad (2.56)$$

, where $\hat{A} = \mathbf{1} - \gamma(\overline{\hat{H}} \hat{H} + \lambda \overline{\hat{L}} \hat{L})$ and $\hat{G} = \gamma \overline{\hat{H}} \hat{Y}$

JANSSON-VAN CITTERT (JVC)

The Eq. 2.33 can be manipulated in the following way:

$$y - Hx = 0 \Rightarrow y - Hx + x = x \quad (2.57)$$

In iterative form, along with the use of some weighting coefficients and the non-negative projection, the JVC **solution** is:

$$x_{n+1} = \mathcal{P}_{(\mathbb{R}^+)} \{ x_n + w \odot (y - Hx) \} \quad (2.58)$$

, where W : weighting coefficient matrix defined as $K[1 - \frac{2}{B-A} |x_n - \frac{A+B}{2}|]$, A, B : min and max values of x_k respectively, K : constant

In the practical form for algorithms, this is expressed as:

$$x_{n+1} = \mathcal{P}_{(\mathbb{R}^+)} \{ x_n + w \odot \mathcal{F}^{-1} \{ \hat{Y} - \hat{H} \hat{X} \} \} \quad (2.59)$$

This algorithm is quite straightforward and simple, but it exhibits slow convergence to an acceptable solution. This might mean that more iterations are needed. However, due to the fact that JVC does not take into account the additive noise of the image, as iterations increase it is possible that resonance effects will be created and constructive image artifacts will be generated. To partially overcome these problems, the initial guess is filtered with a Gaussian or a Wiener filter and each of 4-7 iterations is smoothed with a Gaussian filter of variable width.

GOLD

This algorithm manipulates the Eq. 2.33 in a way to form an iterative multiplicative solution. Note: the multiplications and division are element-wise.

$$y = Hx \Rightarrow \frac{y}{Hx} = 1 \Rightarrow \frac{y}{Hx} x = x \Rightarrow \quad (2.60)$$

$$\Rightarrow x_{n+1} = \mathcal{P}_{(\mathbb{R}^+)} \left\{ x_n \frac{y}{Hx} \right\} \quad (2.61)$$

In the practical form for algorithms, this is expressed as:

$$\Rightarrow x_{n+1} = \mathcal{P}_{(\mathbb{R}^+)} \left\{ x_n \frac{y}{\mathcal{F}^{-1}\{\hat{H}\hat{X}\}} \right\} \quad (2.62)$$

The same conclusions of JVC apply to the GOLD algorithm, although multiplicative formulation of GOLD gives a more rapid convergence than JVC.

RICHARDSON-LUCY (RL)

The previously examined algorithms did not take into consideration any existing noise. But, the statistical information of the noise in the observed image y can be used in order to reconstruct a more precise image. To find the estimate x , one must answer to the question: *Which image of the very many possible ones, is the most likely to be the desired underlying true image x , given the noisy image y ?* The meaning of probability is actually in terms of a normalized frequency of photon events in each image pixel.

The above x and y symbols denote the image matrices. So, the unknown x is expressed as:

$$\hat{x} = \operatorname{argmax}_x p(x|y) \quad (2.63)$$

, where \hat{x} denotes the estimated image x .

Thus, the estimate is the image with the Maximum A Posteriori (MAP) probability.

It is known that:

$$p(x|y) = \frac{p(x, y)}{p(y)} = \frac{p(y|x)p(x)}{p(y)} \quad (2.64)$$

From the two above equations it follows that:

$$\hat{x} = \operatorname{argmax}_x p(y|x)p(x) \quad (2.65)$$

This is equal to minimizing the negative logarithm of the argument, providing the cost function:

$$\mathcal{C}(y, x) = -\ln p(y|x) - \lambda \ln p(x) = L(y, x) + \lambda \Omega(x) \quad (2.66)$$

, where λ : regularization parameter, $\Omega(x)$: smoothing function.

There are two subfamilies of algorithms. Those that do not use the regularization function and follow a Poisson-distributed noise and those that use the regularization function but follow a Gaussian-distributed noise for the sake of math simplification. Richardson-Lucy belongs to the first category, which minimizes the likelihood $y|x$, thus making it a Maximum Likelihood Estimation (MLE) algorithm.

In the RL concept, every image pixel follows the Poisson distribution, that is the probability of obtaining a noisy pixel y_m given its noise-free averaged value μ_m , which is expressed as:

$$p(y_m|\mu_m) = \frac{\mu_m^{y_m} e^{-\mu_m}}{y_m!} \quad (2.67)$$

Every pixel is statistically independent from the others, so the probability of the whole image is equal to the product of the individual probabilities, giving:

$$p(y|x) = p(y|\mu) = \prod_m p(y_m|\mu_m) = \prod_m \frac{\mu_m^{y_m} e^{-\mu_m}}{y_m!} \quad (2.68)$$

Substituting the above expression into the cost function $\mathcal{C}(y, x) = -\ln p(y|x)$ gives:

$$\mathcal{C}(y, \mu) = \sum_m (\mu_m - y_m \ln \mu_m + \ln y_m!) \quad (2.69)$$

Since μ is the image of the noise-free averaged pixel values, it is true that μ is actually the noise-free convolution of the true image x and the PSF h (see Eq. 2.31). That is: $\mu = y * h$. Since, though, the $\mathcal{C}(y, \mu)$ contains a sum, it is better to express the convolution (for a single image pixel) in the sum form as: $\mu_m = \sum_l h_{l-m} x_l$

So, by setting the derivative of the $\mathcal{C}(y, x_l)$ to zero, with respect to x_l , it follows that:

$$\frac{\partial \mathcal{C}(y, x_l)}{\partial x_l} = \sum_l \left(h_{m-l} \frac{y_l}{\sum_n h_{n-l} x_n} \right) - 1 = 0 \quad (2.70)$$

Manipulating the above equation in order to convert it to an iterative multiplicative form, it gives:

$$x_m^{k+1} = K x_m^k \left(\sum_l \left(h_{m-l} \frac{y_l}{\sum_n h_{n-l} x_n^k} \right) \right) \quad (2.71)$$

, where K: normalizing energy constant.

This can be written back again to the convolution and matrix notation, as in this way the **solution** can be executed in the Fourier Transform domain:

$$x^{k+1} = x^k \odot h^T * \left(\frac{y}{h * x^k} \right) \quad (2.72)$$

, where multiplication and division are element-wise and h^T is the flipped PSF matrix.

From the above solution it is apparent that the implementation of the RL algorithm is easy as long as no extra parameters are included. Since noise is integrated in the algorithm, RL is generally more robust to noise than the aforementioned methods. However, RL exhibits very slow convergence to an acceptable image-solution, because it takes more computing time per iteration than the previously mentioned classical algorithms.

RICHARDSON-LUCY TOTAL VARIATION (RL-TV)

As examined in the previous methods, a regularization in the final solution helps counterbalancing noise amplification. The same can be applied in the RL solution. Specifically, regularization is achieved by minimizing the total variation of the image which is defined as the integral of the absolute gradient of the image. To put it practically, the total variation of a 1D signal is the length of the curve defining the signal itself. This can be expanded for images too. So, to derive the solution-image, a mutual minimization of the cost function of the RL (Eq. 2.69) plus the total variation of the image must happen. In a convolution and matrix notation along with a regularization factor, this can be expressed as:

$$\mathcal{C}(x) = h * x - y \ln(h * x) + \lambda \| Dx \|_1 \quad (2.73)$$

, where D : 1st order differentiation operator of x , λ : regularization parameter.

To derive the minimized **solution** from the $\mathcal{C}(x)$ a multiplicative form of the gradient descent method is used:

$$x_{k+1} = x_k [- \lambda \nabla \mathcal{C}(x_k)] \Rightarrow \quad (2.74)$$

$$\Rightarrow x_{k+1} = x_k \odot h^T * \left(\frac{y}{h * x_k} \right) \odot \frac{1}{1 + \lambda g_k} \quad (2.75)$$

, where g_k : the derivative of a regularized version of $\| Dx_k \|_1$.

Note: The L1 norm penalization is known to better preserve image discontinuities compared to L2 norm.

FAST ITERATIVE SOFT-THRESHOLDING ALGORITHM (FISTA)

Alternative regularization terms to the cost function of RIF (Eq. 2.42) can be considered. In particular, sparsity (regularization) constraints in the *wavelet domain* have proven to yield better preservation of image details and discontinuities. The associated cost function is:

$$\mathcal{C}(\mathbf{x}) = \| \mathbf{y} - H\mathbf{x} \|_1^2 + \lambda \| W\mathbf{x} \|_1 \quad (2.76)$$

, where W : a Wavelet Transform operator

Due to the nonsmoothness of the ℓ_1 norm, gradient-descent algorithms cannot be used. However, the problem can be solved efficiently by fast iterative soft-thresholding with the following iterations:

$$\mathbf{z}_{n+1} = \mathbf{s}_n - \gamma H^T (H\mathbf{s}_n - \mathbf{y}) \quad (2.77)$$

$$\mathbf{x}_{n+1} = W^T \mathcal{F}(W\mathbf{z}_{n+1}, \gamma\lambda) \quad (2.78)$$

, where $\mathcal{F}(\cdot, \tau)$: a soft-thresholding operator with threshold τ . In general, soft-thresholding means that a signal is sunk into a region determined by the following. When a particular signal value $x \in [-\tau, \tau]$, it becomes 0. When $x > |\tau|$, then it acquires the value $\text{sign}(x) \cdot (|x| - \tau)$.

$$p_{n+1} = \frac{1}{2} \left(1 + \sqrt{1 + 4p_n^2} \right) \quad (2.79)$$

$$\mathbf{s}_{n+1} = \mathbf{x}_{n+1} + \frac{p_n - 1}{p_{n+1}} (\mathbf{x}_{n+1}) - \mathbf{x}_n \quad (2.80)$$

Again, it is better the equations containing convolution operations to be expressed in the Fourier domain.

BLIND DECONVOLUTION

All the previously examined algorithms demand the knowledge of the PSF. But when acquiring the PSF is proved to be difficult for reasons of any kind, then an alternative approach is the use of blind deconvolution methods. They are termed "blind" because they try to estimate the true image out of the blurred one without knowing the impulse response function of the optical system (PSF). So, in order to start making guesses about the estimate, they must apply some constraints both on the estimate and the PSF. The constraints on the estimate may have the form of non-negativity, finite support with the latter referring to the smallest rectangle within which the true object is contained. Finite support has effect on fluorescence and astronomy images where objects are easily identified. The constraints on the PSF may have the form of symmetry, finite support, known parametric form with the latter meaning a particular type of blurring like defocus or camera motion blur.

Implementations of this category of algorithms may vary. In the next chapter, the blind deconvolution is realised with the algorithm explained below (as implemented in the Image Processing Toolbox of MATLAB[®]). Again, \mathbf{x} denotes the true image vector, \mathbf{y} the observed image vector and \mathbf{h} the PSF image vector.

The algorithm uses the standard MLE algorithm described above, together with a PSF estimation for each iteration. The object is computed, using the MLE estimation, as follows:

$$x^{k+1} = K x^k \odot h^T * \left(\frac{y}{h * x^k} \right) \quad (2.81)$$

Using exactly the same mathematical reasoning, PSF is estimated by maximizing the log likelihood function with respect to h , which gives:

$$h^{k+1} = \frac{1}{N} h^k \odot x^T * \left(\frac{y}{x * h^k} \right) \quad (2.82)$$

, where N is a normalization constant relating to the unit volume.

The following iterations take place as implemented in MATLAB. At first, estimate and PSF predictions (\mathbf{j} and \mathbf{k} respectively) using the non-negativity constrained are made:

$$\mathbf{j} = \mathcal{P}_{(\mathbb{R}^+)} \{ \mathbf{x}_n + \lambda_{x,n} (\mathbf{x}_n - \mathbf{x}_{n-1}) \} \quad (2.83)$$

$$\mathbf{k} = \mathcal{P}_{(\mathbb{R}^+)} \{ \mathbf{h}_n + \lambda_{h,n} (\mathbf{h}_n - \mathbf{h}_{n-1}) \} \quad (2.84)$$

As for the \mathbf{h}_0 , a initial PSF is assumed. The critical part of the assumption is the initial PSF image size, rather than an attempt to find a good PSF approach. Note: \mathbf{k} is normalised so that the PSF pixels sum to the value 1. Normalization is a necessary constraint because given only input image, the algorithm cannot know how much power is in the image vs the PSF.

$\lambda_{x,n}$ is a coefficient for the estimate prediction that is computed by:

$$\lambda_{x,n} = \boldsymbol{\alpha}_{x,n}^T \boldsymbol{\beta}_{x,n} / \boldsymbol{\beta}_{x,n}^T \boldsymbol{\beta}_{x,n}, \quad 0 \leq \lambda_{x,n} \leq 1 \quad (2.85)$$

Where:

$$\boldsymbol{\alpha}_{x,n} = \mathbf{x}_n - \mathbf{j} \quad (2.86)$$

and

$$\boldsymbol{\beta}_{x,n} = \boldsymbol{\alpha}_{x,n-1} \quad (2.87)$$

$\lambda_{h,n}$ is a coefficient for the PSF prediction that is computed by:

$$\lambda_{h,n} = \boldsymbol{\alpha}_{h,n}^T \boldsymbol{\beta}_{h,n} / \boldsymbol{\beta}_{h,n}^T \boldsymbol{\beta}_{h,n}, \quad 0 \leq \lambda_{h,n} \leq 1 \quad (2.88)$$

Where:

$$\boldsymbol{\alpha}_{h,n} = \mathbf{h}_n - \mathbf{k} \quad (2.89)$$

and

$$\boldsymbol{\beta}_{h,n} = \boldsymbol{\alpha}_{h,n-1} \quad (2.90)$$

The above computed estimate and PSF predictions are used in the Richardson-Lucy algorithm that produces the deconvolved estimate of the true image in each iteration.

GHOST ARTIFACTS, ZERO-PADDING AND EDGE TAPERING

Data subjected to a FFT must necessarily be assumed to be periodic. This implies that borders at opposite sides of the image are implicitly adjoined once periodization is taken into account. Consequently, structures near the borders of an image, once processed, will spill over the opposite border, letting ghosts appear. For this reason, images can be padded with zeros beyond all edges, resulting in an expanded image with dark regions around. If the padding is sufficient the ghost artifacts appear only in the dark regions. Finally, ghosts are cropped out. If it is not wanted images to be expanded, another solution is to blur the regions near the boundaries with the PSF, easing in that way the effect of ghosts after deconvolution. This technique is called edgetapering.

RINGING ARTIFACTS AND EARLY STOPPING

As far as all the algorithms are concerned, as it was previously explained in the Landweber algorithm section, inversed signals from the Fourier domain to the spatial one exhibit some overshoots and undershoots in areas of discontinuities and high signal jumps. Fourier Transform is performed in a discretized form allowing a finite number of harmonics to contribute in building the original signal. It is apparent that, the more harmonics included the better the representation of the original signal and the less the oscillations. However, these oscillations do not die out as the number of harmonics increases, but they reach a limit. This peculiar fact is known as the *Gibbs phenomenon* and explains the cause of *ringing artifacts* in images being processed with Fourier Transforms.

Hence, oscillations are imposed progressively on oscillations caused by FT. So, in order to avoid ringing artifact amplification in high contrast areas of images, the number of iterations is preferable not to exceed a limit which can be better found

by eye-evaluation of the resulted image. Algorithms in general though, can integrate such an *early stopping* criterion with the aid of quantitative metrics. Specifically they choose to stop the iterations, when they "see" that no substantial changes are made to the image.

2.4.3 Standard Processing Techniques

There exist simpler methods of enhancing the image quality [13] that differ from the deconvolution logic. Deconvolution methods enhance image resolution, whereas *Standard Processing Techniques* (SPT) enhance image contrast for visual purposes only. In the next chapter, a humble comparison between deconvolution methods and SPT is done in terms of quantitative metrics showing image quality enhancement.

- *Histogram Equalization*: A histogram shows the number of occurrences of each single grayscale pixel value of the image. It is an indicator of image contrast. Images with overwhelming percentages of white or black pixels have a low contrast, meaning difficulty in detail determination. For this kind of images, an imposed balance (equalization) between bright and dark pixels can provide the wanted high contrast.
- *Histogram Equalization in tiles*: Because images contain smooth regions as well as very detailed ones, histogram equalization in the whole image may destroy the details. So, the equalization is imposed in subregions of the image called tiles.
- *Sharpening*: A way of sharpening an image is using an image termed "unsharp" mask. Specifically, the original image is inverted, giving its negative image. Then, the latter is blurred to some degree and scaled to lower intensities. Finally, the addition of the original image with the scaled and blurred one is proved to provide a more sharp image than the initial.
- *Adjustment/Scaling*: A grayscale image is known to have pixel values in the range $[0, 1]$. This range can be changed in a way that for a quite bright image the most bright pixels are saturated in a lower value than 1 (decreasing brightness) and similarly, for a quite dark image the most dark pixels are saturated in a higher value (decreasing darkness). With this "trick" the initial image obtains a high contrast profile compared to the prior one.
- *Local Laplacian Filter*: This filter uses the Laplacian operator which imposed on (convolved with) an image gives a measure of the 2^{nd} spatial derivative of an image. The Laplacian of an image highlights regions of rapid intensity change which in turn can provide edge-detection information. It is desired intensity changes to be more highlighted in high-contrast regions whereas less highlighted in low-contrast regions.

2.5 Quantitative metrics of image quality and enhancement

After the deconvolution process is done, evaluating the quality of the result can be done in several ways.

RESIDUAL NORM

By reblurring the true image estimate (x) after the deconvolution process, it can be seen how similar this degraded image is with the original (y). If the reblurred image is close to the original image, this means that the deconvolution process worked effectively. The reblurred image is constructed convolving the deconvolution result with the PSF (circulant matrix H).

Hence, the difference $y - Hx$ is desired to be computed. This is called the residual between y and Hx . In order to obtain a single scalar number index, the sum of the squared values of the elements of the residual image [19] or equivalently the squared ℓ_2 norm of the residual image is computed and normalized by the square root of the total number of the residual elements. This is written as:

$$\text{Residual Norm} = \frac{1}{\sqrt{\text{numel}}} \|y - Hx\|_2^2 \quad (2.91)$$

, where *numel*: total number of residual image pixels

I-DIVERGENCE

Based on the Kullback–Leibler divergence [8] which is a measure of how a probability distribution diverges from a second expected probability distribution, a metric of difference between images can be computed. Probability distributions are substituted by the images which therefore gives a modified Kullback-Leibler measure, called I-divergence:

$$I\text{-divergence} = \sum_{ij} \left\{ (H\mathbf{x})_{ij} \cdot \ln \frac{(H\mathbf{x})_{ij}}{\mathbf{y}_{ij}} - \left((H\mathbf{x})_{ij} - \mathbf{y}_{ij} \right) \right\} \quad (2.92)$$

, where subscripts i, j denote the image pixel of the i -th row and the j -th column.

STRUCTURAL SIMILARITY INDEX (SSIM)

SSIM [23] is a perception-based model that considers image degradation as perceived change in structural information, while also incorporating important perceptual phenomena, including both luminance masking and contrast masking terms. Structural information is the idea that the pixels have strong inter-dependencies especially when they are spatially close. These dependencies carry important information about the structure of the objects in the visual scene. Luminance masking is a phenomenon whereby image distortions tend to be less visible in bright regions, while contrast masking is a phenomenon whereby distortions become less visible where there is significant activity or "texture" in the image.

The SSIM index is calculated on various windows of an image. The SSIM formula is based on three comparison measurements between the samples of two windows u and v (of Hx and y respectively) of common size $N \times N$. These comparison measurements concern luminance (l), contrast (c) and structure (s). The product of them produces the following formula in its final form:

$$SSIM(u, v) = \frac{(2\mu_u\mu_v + c_1)(2\sigma_{uv} + c_2)}{(\mu_u^2 + \mu_v^2 + c_1)(\sigma_u^2 + \sigma_v^2 + c_2)} \quad (2.93)$$

, where μ_u : average of u
 μ_v : average of v

σ_u^2 : variance of u

σ_v^2 : variance of v

σ_{uv} : covariance of u and v

c_1, c_2 : variables to stabilize divisions with weak denominators.

Chapter 3

Deconvolution algorithms GUI with measuring and modelling PSF

The deconvolution algorithms GUI (*deconv_gui.mlapp*) is built on MATLAB® App Designer and is supported on versions R2017a +. Later work will make it operational for older versions. The GUI integrates a set of inverse and iterative deconvolution algorithms along with some standard image processing techniques (SPT). The users of the GUI can examine the effectiveness and efficiency of deconvolution and SPT methods on their own images and PSFs but also on several a priori provided images and PSFs through a set of prepared demo tests. The latter implement a comparison of deconvolution algorithms in terms of convergence time with respect to the residual norm as well as in terms of efficiency of measuring and modelling PSF methods.

3.1 Getting to know the GUI

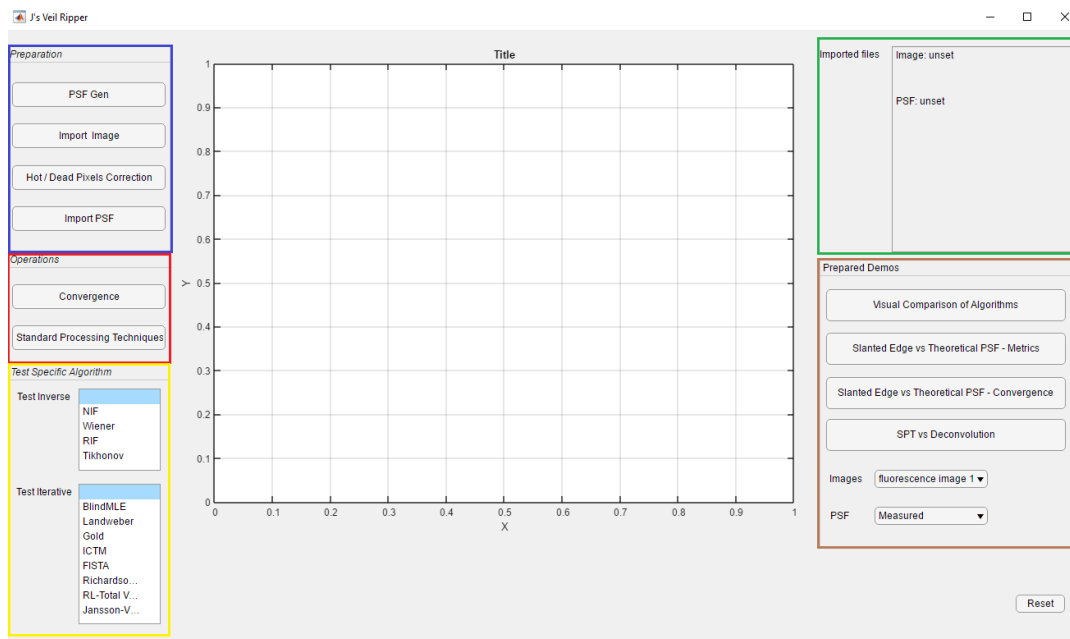


FIGURE 3.1: Initial deconvolution algorithms GUI with highlighted panels

Fig. 3.1 shows the initial GUI with highlighted areas indicating the 5 operational and informational panels. On the left side of the GUI, there are the panels that are oriented for images and PSFs loaded by the users. The blue highlighted panel (*Preparation*) is responsible for image and PSF import. As an additional function, the users can specify settings for constructing a PSF. The red highlighted panel (*Operations*) is about the deconvolution convergence depiction and SPT operations which use the images and PSFs loaded or generated in the preparation step. On the yellow highlighted panel (*Test specific algorithm*) the users can select a single deconvolution algorithm to test with the imported image and PSF. On the right side of the GUI, the users can see the results and graphs of some prepared demo tests by selecting the operations on the brown highlighted panel (*Prepared Demos*). Lastly, the green highlighted panel shows the filenames of the imported image and PSF along with the PSF set filename generated in the Preparation step.

Preparation step

- PSF Gen:** Setting parameters for generating a single PSF or a set of PSFs. Born and Wolf model of PSF is used. The users must specify the wavelength of light used in brightfield microscopy imaging or the emission wavelength of light in fluorescence microscopy. The users might not know the specifications of the microscope that was used for capturing their image. So, they can generate a set of PSFs and examine the results, aiming at finding an NA-magnification combination that is close to the real one. Therefore, regarding a set of PSFs, the users must set the possible minimum and maximum values of NA. Also: the sensor pixel size (or else size of the effective pixel pitch) which is measured in nm. The probable minimum and maximum magnification of the objective lens and lastly the wanted dimensions of the PSF. When a generation of a single PSF is the case, minimum and maximum values of both NA and magnification must be identical.

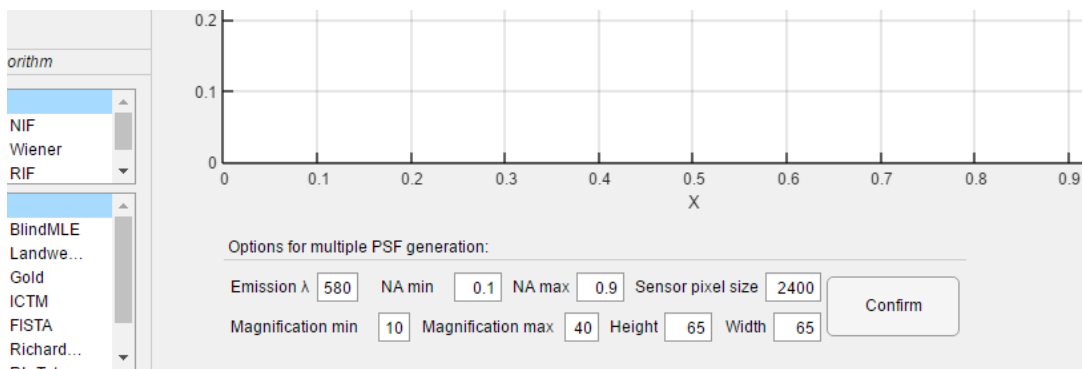


FIGURE 3.2: PSF generation

- Import Image:** Image to be improved.
- Import PSF:** Mat file containing the PSF. PSF can be selected also from a mat file which contains a PSF set.

Operations

- **Convergence:** The users have to define the parameters of each deconvolution algorithm. Then, every algorithm is executed using the imported PSF. In each iteration of every algorithm, the residual norm is computed providing in that way a curve of convergence.
- **Standard Processing Techniques:** Execution and depiction of the techniques explained in Subsec. 2.4.3.

Test Specific Algorithm

A single deconvolution process is executed. Selection of an inverse or an iterative deconvolution algorithm is followed by a panel of parameter setting.

Prepared Demos

Results from pre-executed deconvolution processes using a set of images and modelled or experimental PSFs, as well as pre-produced graphs are available for demonstration. The users can select a particular image and a PSF produced by the Born and Wolf formula or by the Slanted Edge method.

- **Visual Comparison of Algorithms:** All the results of the deconvolution processes are demonstrated with multiple subplots, zooming in a specific region of the images for better illustration of the differences.
- **Slanted Edge vs Modelled PSF - Metrics:** For the particular image selected by the users, deconvolution results using the experimental PSF along with the corresponding modelled one, are compared via residual norm, SSIM and I-divergence. For each metric, a different scatter graph is illustrated.
- **Slanted Edge vs Modelled PSF - Convergence:** As above, but the comparison is done via illustration of the convergence of the residual norm of the iterative deconvolution algorithms.
- **SPT vs Deconvolution:** It shows how SPT perform compared to deconvolution methods. For the selected image and PSF category, the results are demonstrated in a scatter graph.

3.2 Code implementation

3.2.1 Files and directories

startup.m:

```
path(path, genpath(' ./ '));
```

It adds all the folders, subfolders and files to the end of the MATLAB search path.

ALGORITHMS

"/DL/Algorithms" and *"/Other Techniques"* folders.

Regarding the implementation of each algorithm, all the iterative deconvolution methods incorporate residual norm computation in each iteration along with early stopping criterion. The latter is defined in the code as the case when the rate of change of the residual norm falls below -1% .

- NIF, RIF, TRIF, GOLD, JVC, LW, ICTM and FISTA algorithms are implemented by the transfer of the formulae that give the particular image estimates (Subsec. 2.4.2) into MATLAB code. The corresponding files are namesake and located in subfolder *DL/Algorithms*.
- For the RL, Wiener and Blind Deconvolution algorithms, their implementations of the Image Processing Toolbox of MATLAB are used (*deconvrl*, *deconvwnr* and *deconvblind* respectively). RL and Blind Deconvolution are modified only for integrating residual norm computation and early stopping criterion. These two algorithms are located in *rl.m* and *deconv_blind.m* files respectively.
- For the RLTV algorithm, the Total Variation factor is "attached" to the RL result in each iteration. It is located in *rltv.m* file.
- For the Standard Processing Techniques, their implementations of the Image Processing Toolbox of MATLAB are used. The next functions to be mentioned are called in file *runSPT.m* of the folder */SPT*. Histogram Equalization is implemented by function *histeq*, Histogram Equalization in tiles by *adapthisteq*, Sharpening by *imsharpen*, Adjustment/Scaling by *imadjust* and Local Laplacian Filter by *locallapfilt*. *Locallapfilt* is introduced in MATLAB version R2016b.

UTILITIES

/Util folder: Functions that are used throughout the source code files.

- *imzeropad_mk.m*: Not used in the deconvolution processes. It expands the size of the input image by zero-padding for ghost-elimination in a way that the padded image size is a common multiple of 2,3 and 5 which is known to facilitate faster FT computations. If it is needed to be used, it can be called before the algorithm selection switch case, but the resulted image must be cropped at the end and the quality metrics computations must change so as to use only the unpaaded images.
- *multiplesof235.m*: Used by *deconvPrepare.m*. It computes the numbers that are common multiples of 2,3 and 5 till number 27000. So, apparently, images of length or width bigger than 27000 are not padded.
- *cropResult.m*: Used if *deconvPrepare.m* is used. Given the initial dimensions of the padded image, the pads are cropped out.
- *resnorm.m*: It computes the residual norm between *PSF*deconvolution result* and *initialimage*.
- *i_divergence.m*: It computes the I-divergence between *PSF*deconvolution result* and *initialimage*.
- *iterations_stop.m*: It returns a *flag = 1* when the rate of change of the last two residual norms falls below -1% . Every iterative algorithm, in each iteration checks if this *flag == 1* so as not to continue with further deconvolution iterations.
- *iterations_stop2.m*: Another early stopping criterion. Instead of the fall rate of the residual norms, it computes the relative difference between two successive iterations. This criterion is not used in the algorithms.

- *diffraction_psf.m*: Computation of the model of Born and Wolf. Although, it is used for 2D PSFs, it can compute 3D PSFs too.
- *imoutliers_rm.m*: Removal of outliers of image data. When the deviation of a pixel from its surrounding disk-like neighbourhood is larger than a given threshold, then this pixel is replaced by the median of this particular region. The total area of the neighbourhood can be specified by the given radius.

GUI

/gui folder: Functions that are used in source code of *deconv_gui.mlapp*.

- *psfgen.m*: Functionality of "PSF Gen" button.
- *testConvergence.m*: Functionality of "Convergence" button.
- *lspec.m*: It produces diverse colors and marks for lines of plot graphs.
- *savegraphs.m*: Auxiliary file for saving of graphs initially generated in the GUI.

IMAGES AND PSFs

/IOimages folder: It contains originals and deconvolved images along with images processed with SPTs. It also contains PSF .mat files. The users have to copy their images and PSFs in */Images/Originals* and */PSFs* subfolders, respectively.

3.2.2 Software Experiments

Experimental vs Modelled PSF comparison using quantitative metrics

For this test, 3 images were used: 1 from a fluorescence microscope and 2 from a brightfield microscope. For the capture of the fluorescence image, a vibrator mechanism is utilized. This is due to the fact that the specific specimens are wet mounted, meaning that they float through liquid molecules that keep the specimens together on top of the mounting slip of the test glass. These chaotically moving molecules collide with the samples in all directions and when the acting force is stronger in the short term from one direction, the water molecules grant the particle acceleration in that direction; everything then repeats in a new location. The resulting motion is therefore disordered and abrupt [6], therefore causing ripples across the image. For this reason, the use of the vibrator is tested which eliminates such ripples, since the pre-existing tendency is isotropically rearranged because of the constant provision of external energy. Back to the image specifics, it is an RGB image, but the selected channel to operate on is selected to be the green one (even though 580 nm is interpreted as yellow light by our eyes and it is closer to the peak of the red band than that of the green band). Also in this image, there are several spots that can be considered as hot pixels. Because of the emerging ringing effect after deconvolution it is better to remove these spots. This is done with *imoutliers.m*. As for the brightfield images they are grayscale images and they are not pre-processed in any way prior to deconvolution.

Filenames of used images:

- 1) fluor_AREA1_15x_NA0,28_100dB_Ex532nm_Em580nm_LUMNIAPLEX+VIB.png
- 2) brfield_case2_40x_NA0,4_530nm.png
- 3) brfield_case3_23x_NA0,28_505nm.png

Fluorescence image information:

Excitation wavelength: 532 nm
Emmision wavelength: 580 nm
NA: 0.28
Overall magnification 15x
Sensor pixel pitch size: 2400 nm
Vibrator use: Yes
Dimensions: 2080x3096

Brightfield image # 1 information:

Wavelength: 530 nm
NA: 0.4
Overall magnification 40x
Sensor pixel pitch size: 2400 nm
Vibrator use: No
Dimensions: 2080x3096

Brightfield image # 2 information:

Wavelength: 505 nm
NA: 0.28
Overall magnification 23x
Sensor pixel pitch size: 2400 nm
Vibrator use: No
Dimensions: 2080x3096

These images are deconvolved with every algorithm, iterative or inverse. Regarding iteratives, the goal is to show how every algorithm converges with respect to the residual norm. The results are displayed on a plot graph. Due to the imposition of the early stopping criterion (*iterations_stop.m*, Subsec. 3.2.1) each algorithm stops at different number of iterations. Regarding inverse algorithms, their corresponding residual norms are displayed as straight lines in the convergence vs iterations plot graph.

Besides the effectiveness of the algorithms as far as the the residual norm is concerned, their execution times are definitely of great significance and display their efficiency as well. Every image is deconvolved with both its corresponding modelled (Born and Wolf) PSF and the experimental one which is originated from the Slanted Edge method. In order to eradicate the ghost artifacts that emerge on the boundaries of the image, it is chosen the regions near the boundaries to be blurred using the *edgetaper* function from the Image Processing Toolbox. Edgetaper method requires PSF size to be at most half the size of the image to be deconvolved. Since, the PSF obtained by the Slanted Edge method has the same size with the image, it needs to be cropped. More specifically, the cropping process centralizes the PSF, since the modelled PSF is also centralized. The PSF size is chosen as 65x65 for both modelled and experimental PSFs.

When it comes to the deconvolution algorithms, the results of the deconvolution operations can be seen by clicking on the **Visual Comparison** button of the *Prepared Demos* panel. All the deconvolution results are displayed in a figure. Specifically,

the images are zoomed in a specific region to allow better visual perception of the differences between the algorithms.

The convergence of the iterative algorithms with respect to the residual norms and in comparison with the inverse algorithms plus their execution times, is shown by clicking on the *Slanted Edge vs Modelled PSF - Convergence* button. In addition to this, all the image quality metrics can be shown by clicking on the *Slanted Edge vs Modelled PSF - Metrics* button. As an extra, SPTs can be compared with deconvolution algorithms by clicking on the *SPT vs Deconvolution* button.

The algorithms are tested with several different combinations of their particular parameters. The final parameters that are used, were selected having in mind the residual norm convergence and the other metrics results as well as the visual perception of the resulted image. More specifically, it is observed that in some cases the residual norm might continue to fall (and also the I-divergence which follows a similar behavior) even if the deconvolution result keeps deteriorating as perceived by the human eye. In these cases, SSIM acts as a good compass, which integrates human eye particularities regarding image perception. As for speed, the maximum iterations are set to 15. If a specific algorithm does not stop automatically by the early stopping criterion, then the best number of iterations for this algorithm is set by visual examination of the results.

For the fluorescence image, the used parameters of the algorithms are as follows:

Blind deconvolution: iterations = 5 | initial PSF size = 5x5

Deconvolution with modelled PSF:

Wiener: NSR = 1e-2
 RIF: lambda = 1e-1
 TRIF: lambda = 1e-2
 LW: iterations = 14 | gamma = 1.7
 ICTM: iterations = 14 | gamma = 1.7 | lambda = 1e-3
 GOLD: iterations = 3
 JVC: iterations = 10
 RL: iterations = 7
 RLTV: iterations = 5 | lambda = 1e-2
 FISTA: iterations = 8 | gamma = 1.2 | lambda = 1e-4
 | wavelet: symlet2 | decomposition levels = 3

Deconvolution with experimental PSF:

Wiener: NSR = 1e-2
 RIF: lambda = 1e-1
 TRIF: lambda = 1e-2
 LW: iterations = 12 | gamma = 1.7
 ICTM: iterations = 12 | gamma = 1.7 | lambda = 1e-3
 GOLD: iterations = 4
 JVC: iterations = 10
 RL: iterations = 6
 RLTV: iterations = 5 | lambda = 1e-2
 FISTA: iterations = 7 | gamma = 1.2 | lambda = 1e-4
 | wavelet: symlet2 | decomposition levels = 3

The following **images** and **graphs** display:

- Fig. 3.3-Fig. 3.4 The original **fluorescence image** along with the Blind deconvolution result and the deconvolved images using the **experimental PSF**.
- Fig. 3.5-Fig. 3.6 The original **fluorescence image** along with the Blind deconvolution result and the deconvolved images using the **modelled PSF**.
- Fig. 3.7 Standard Processing Techniques results.
- Fig. 3.8-Fig. 3.9 Intensity profile across a defined line on the image. A thin object with abrupt changes of luminance was chosen.
- Fig. 3.10 Convergence of the iterative algorithms with respect to the residual norms, along with the inverse deconvolution results (the straight lines) and the time of executions.
- Fig. 3.11 Comparison of the residual norms of the deconvolution results.
- Fig. 3.12 Comparison of the SSIM of the deconvolution results.
- Fig. 3.13 Comparison of the I-divergence of the deconvolution.
- Fig. 3.14 Comparison of Standard Processing Techniques.

For the brightfield image # 1, the used parameters of the algorithms are as follows:

Blind deconvolution: iterations = 5 | initial PSF size = 5x5

Deconvolution with modelled PSF:

```

Wiener: NSR = 2e-2
RIF:    lambda = 1e-1
TRIF:   lambda = 1e-2
LW:     iterations = 15 | gamma = 1.7
ICTM:   iterations = 15 | gamma = 1.7      | lambda = 1e-3
GOLD:   iterations = 5
JVC:    iterations = 5
RL:     iterations = 10
RLTV:   iterations = 5 | lambda = 1e-2
FISTA:  iterations = 10 | gamma = 1.2      | lambda = 1e-4
        | wavelet: symlet2 | decomposition levels = 3

```

Deconvolution with experimental PSF:

```

Wiener: NSR = 5e-3
RIF:    lambda = 1e-1
TRIF:   lambda = 1e-2
LW:     iterations = 15 | gamma = 1.8
ICTM:   iterations = 15 | gamma = 1.8      | lambda = 1e-4
GOLD:   iterations = 5
JVC:    iterations = 10
RL:     iterations = 10
RLTV:   iterations = 10 | lambda = 1e-3
FISTA:  iterations = 15 | gamma = 1.2      | lambda = 1e-4
        | wavelet: symlet2 | decomposition levels = 3

```

The following **images** and **graphs** display:

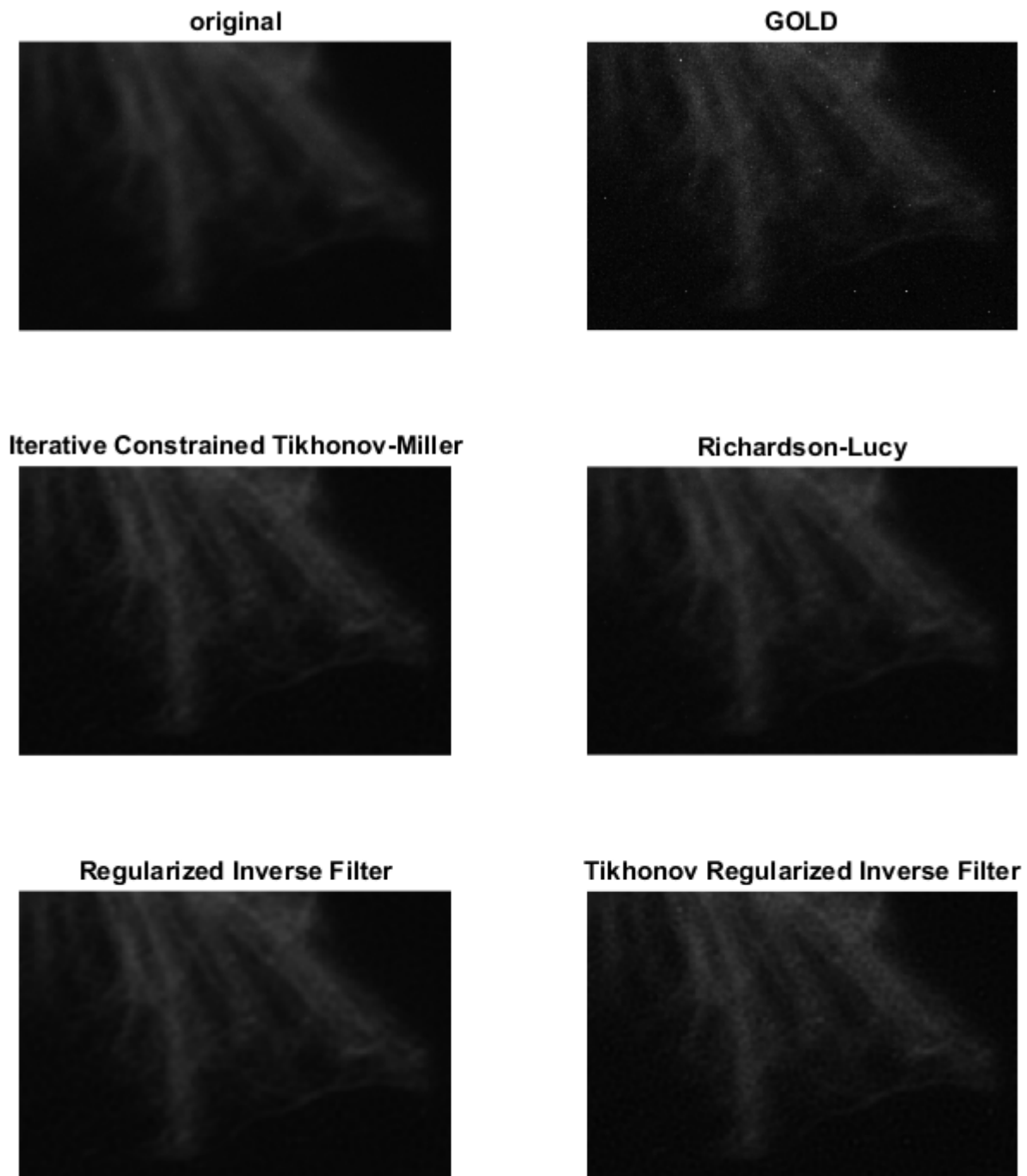


FIGURE 3.3: Deconvolution results with the use of the measured PSF (in comparison with the original image and the Blind deconvolution result).

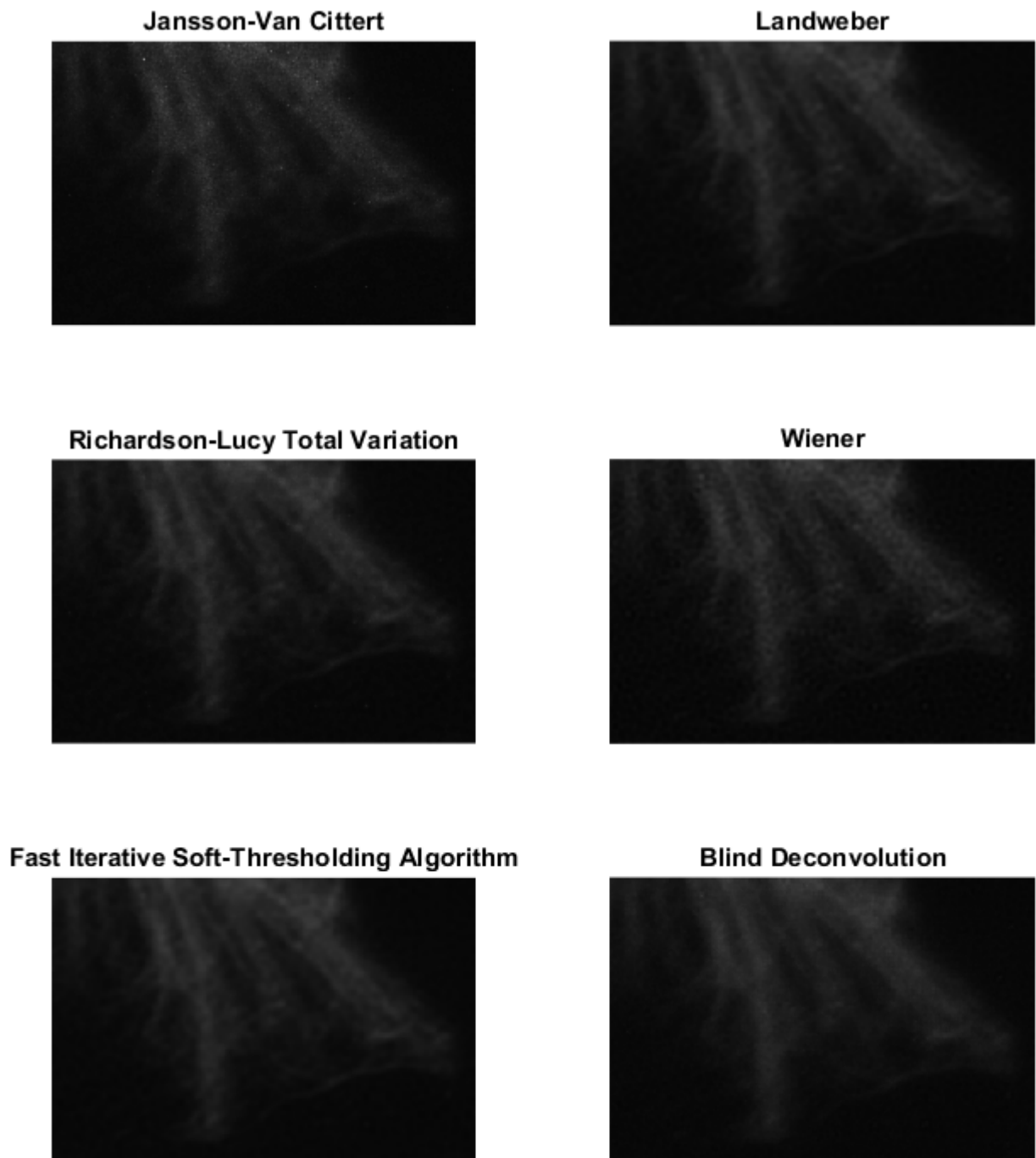


FIGURE 3.4

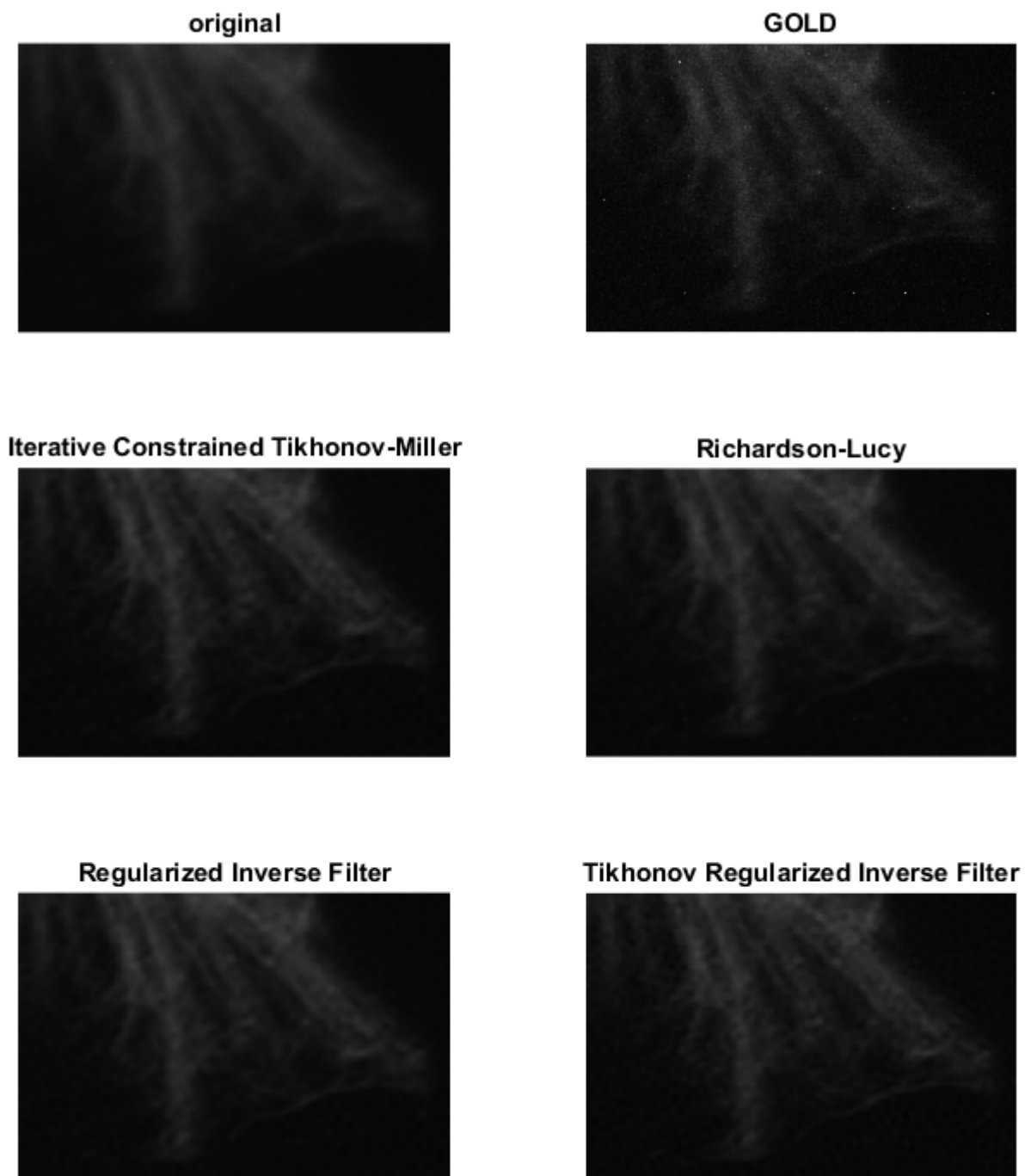


FIGURE 3.5: Deconvolution results with the use of the modelled PSF (in comparison with the original image and the Blind deconvolution result).

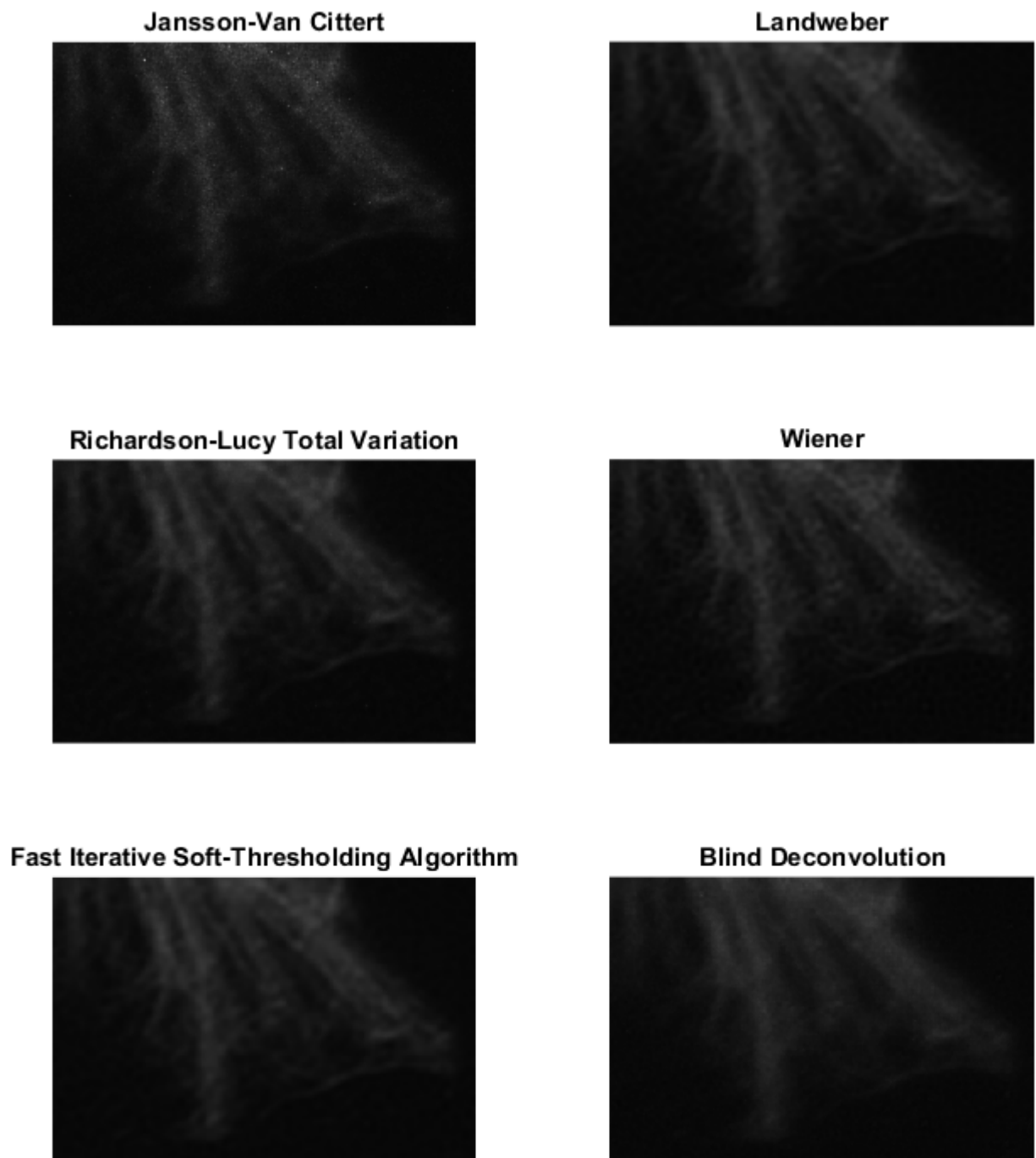


FIGURE 3.6

- Fig. 3.15-Fig. 3.16 The original brightfield image # 1, along with the Blind deconvolution result and the deconvolved images using the experimental PSF.
- Fig. 3.17-Fig. 3.18 The original **fluorescence image** along with the Blind deconvolution result and the deconvolved images using the **modelled PSF**.
- Fig. 3.19 Standard Processing Techniques results.
- Fig. 3.20-Fig. 3.21 Intensity profile across a defined line on the image. A round cell was chosen.
- Fig. 3.22 Convergence of the iterative algorithms with respect to the residual norms, along with the inverse deconvolution results (the straight lines) and the time of executions.
- Fig. 3.23 Comparison of the residual norms of the deconvolution results.
- Fig. 3.24 Comparison of the SSIM of the deconvolution results.
- Fig. 3.25 Comparison of the I-divergence of the deconvolution.
- Fig. 3.26 Comparison of Standard Processing Techniques.

For the brightfield image # 2, the used parameters of the algorithms are as follows:

Blind deconvolution: iterations = 5 | initial PSF size = 5x5

Deconvolution with modelled PSF:

```

Wiener: NSR = 5e-3
RIF:    lambda = 1e-1
TRIF:   lambda = 1e-2
LW:     iterations = 15 | gamma = 1.7
ICTM:   iterations = 15 | gamma = 1.7      | lambda = 1e-3
GOLD:   iterations = 5
JVC:    iterations = 5
RL:     iterations = 10
RLTV:   iterations = 5 | lambda = 1e-3
FISTA:  iterations = 10 | gamma = 1.3      | lambda = 1e-3
        | wavelet: symlet2 | decomposition levels = 3

```

Deconvolution with experimental PSF:

```

Wiener: NSR = 5e-3
RIF:    lambda = 1e-1
TRIF:   lambda = 1e-2
LW:     iterations = 15 | gamma = 1.8
ICTM:   iterations = 15 | gamma = 1.8      | lambda = 1e-4
GOLD:   iterations = 5
JVC:    iterations = 5
RL:     iterations = 10
RLTV:   iterations = 5 | lambda = 1e-3
FISTA:  iterations = 10 | gamma = 1.2      | lambda = 1e-4
        | wavelet: symlet2 | decomposition levels = 3

```

The following **images** and **graphs** display:

- Fig. 3.27-Fig. 3.28 The original brightfield image # 2, along with the Blind deconvolution result and the deconvolved images using the experimental PSF.
- Fig. 3.17-Fig. 3.18 The original **fluorescence image** along with the Blind deconvolution result and the deconvolved images using the **modelled PSF**.
- Fig. 3.31 Standard Processing Techniques results.
- Fig. 3.32-Fig. 3.33 Intensity profile across a defined line on the image. A round cell was chosen.
- Fig. 3.34 Convergence of the iterative algorithms with respect to the residual norms, along with the inverse deconvolution results (the straight lines) and the time of executions.
- Fig. 3.35 Comparison of the residual norms of the deconvolution results.
- Fig. 3.36 Comparison of the SSIM of the deconvolution results.
- Fig. 3.37 Comparison of the I-divergence of the deconvolution.
- Fig. 3.38 Comparison of Standard Processing Techniques.

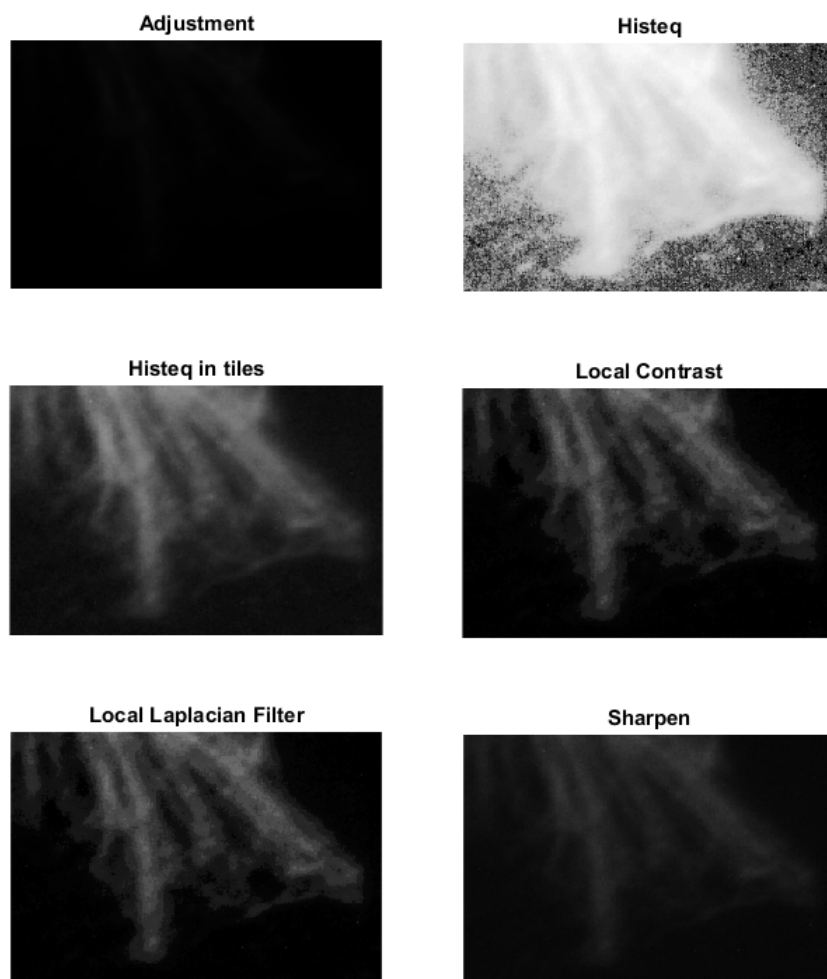


FIGURE 3.7: SPT results

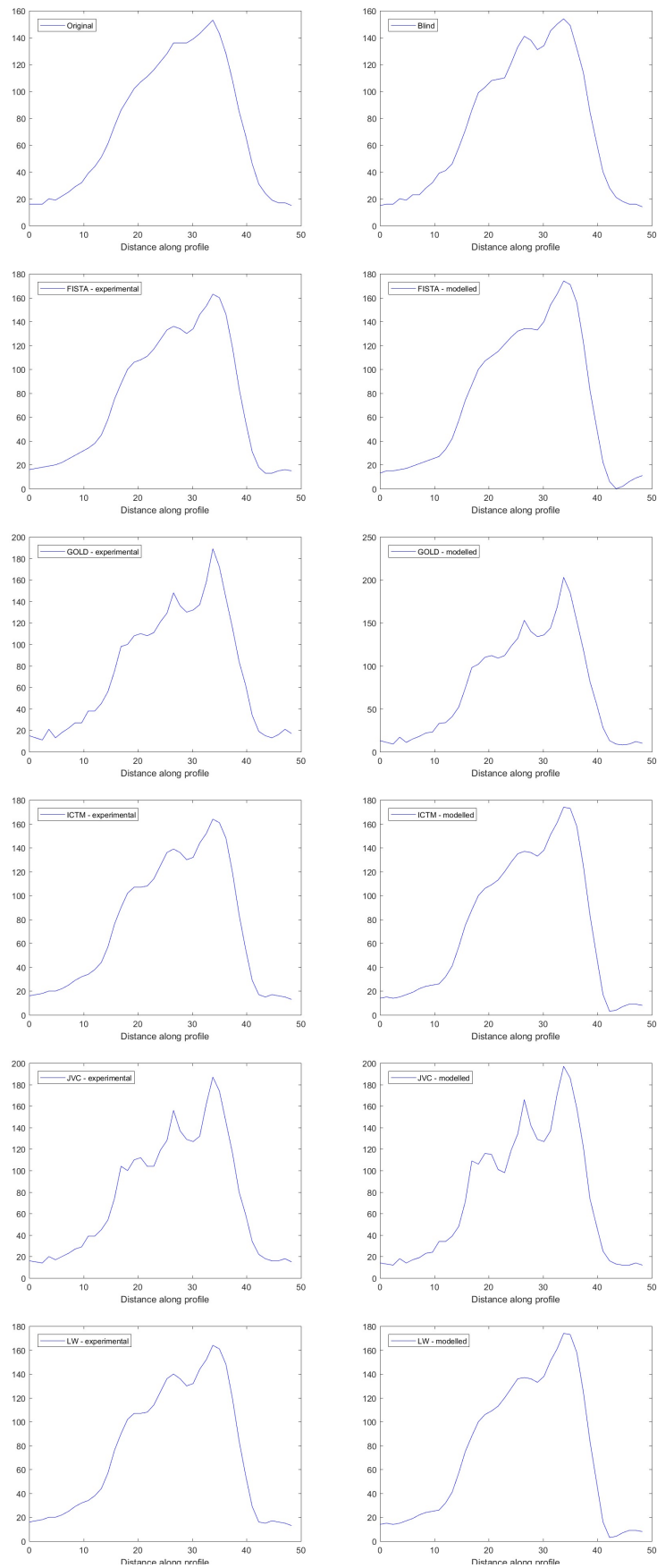


FIGURE 3.8: Intensity profiles

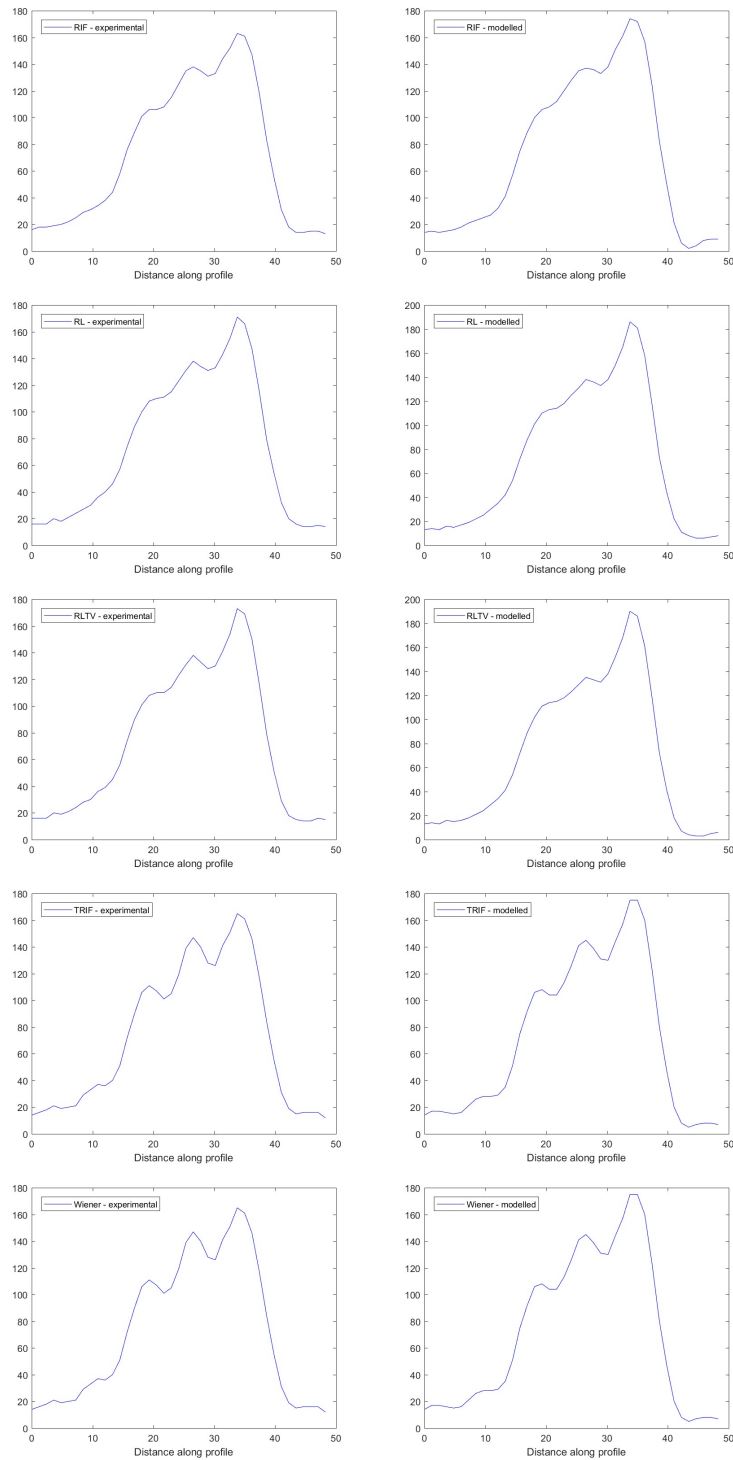


FIGURE 3.9

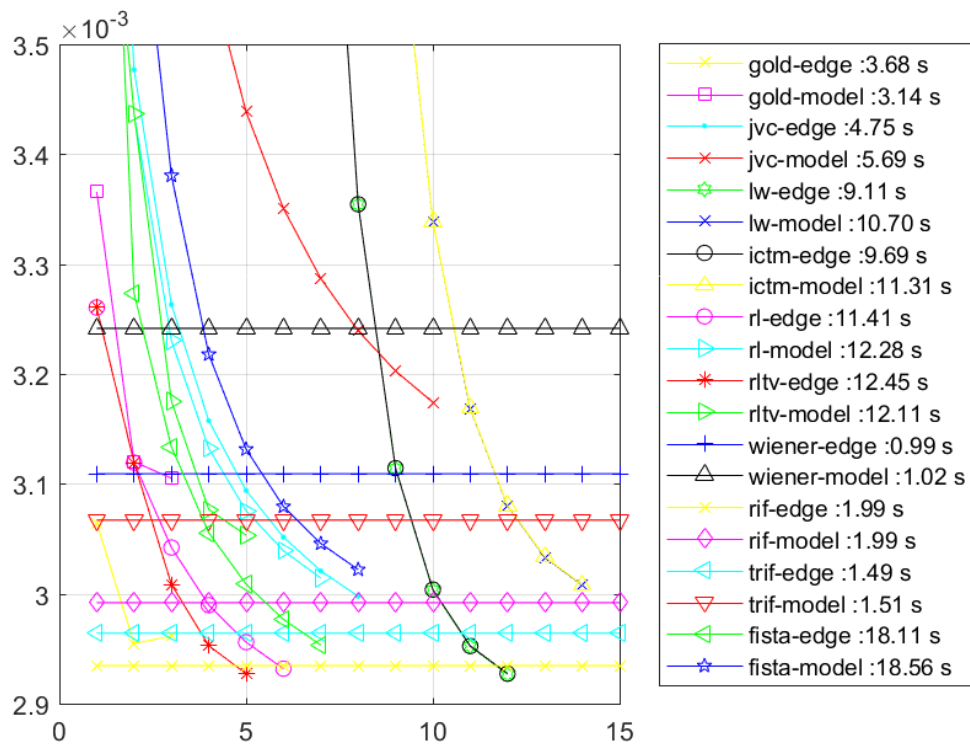


FIGURE 3.10: Convergence of iterative algorithms - execution times

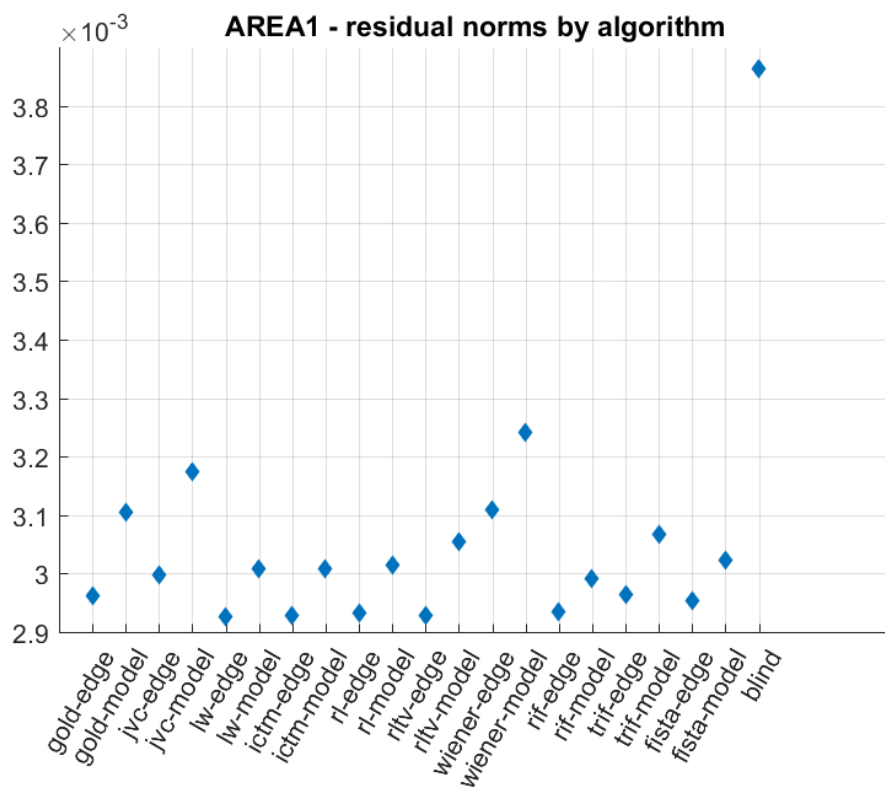


FIGURE 3.11: Residual norms of every algorithm

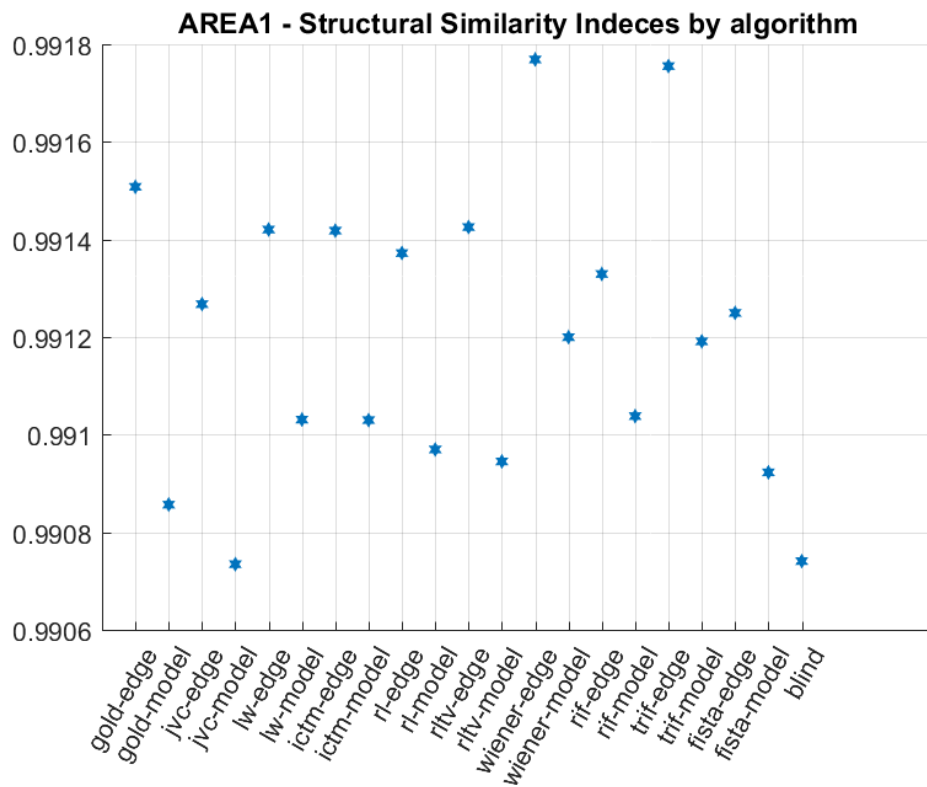


FIGURE 3.12: SSIM of every algorithm

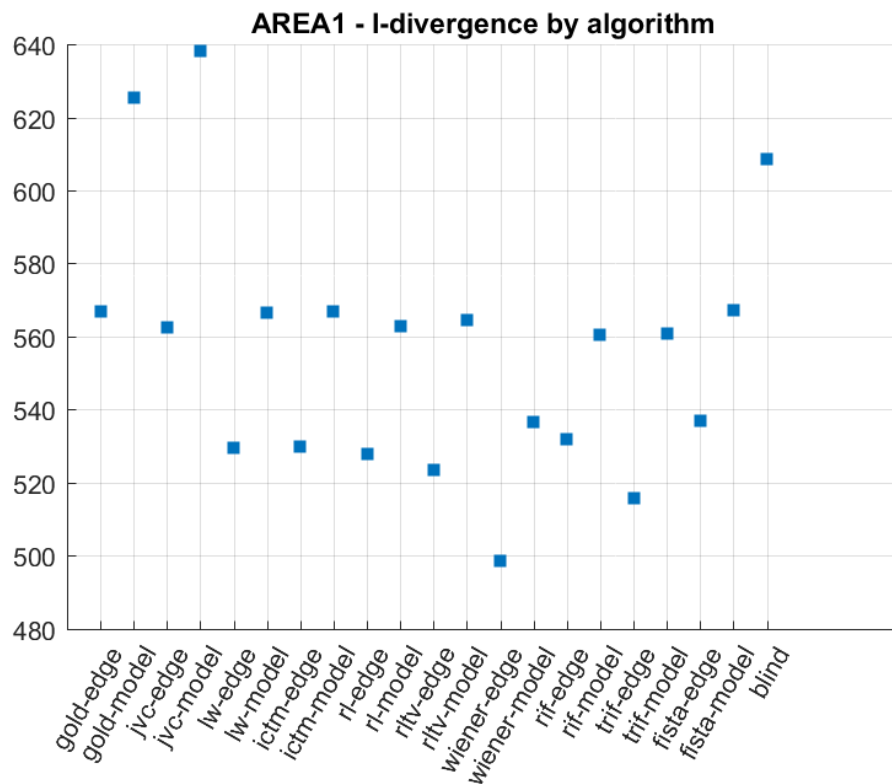


FIGURE 3.13: I-divergence of every algorithm

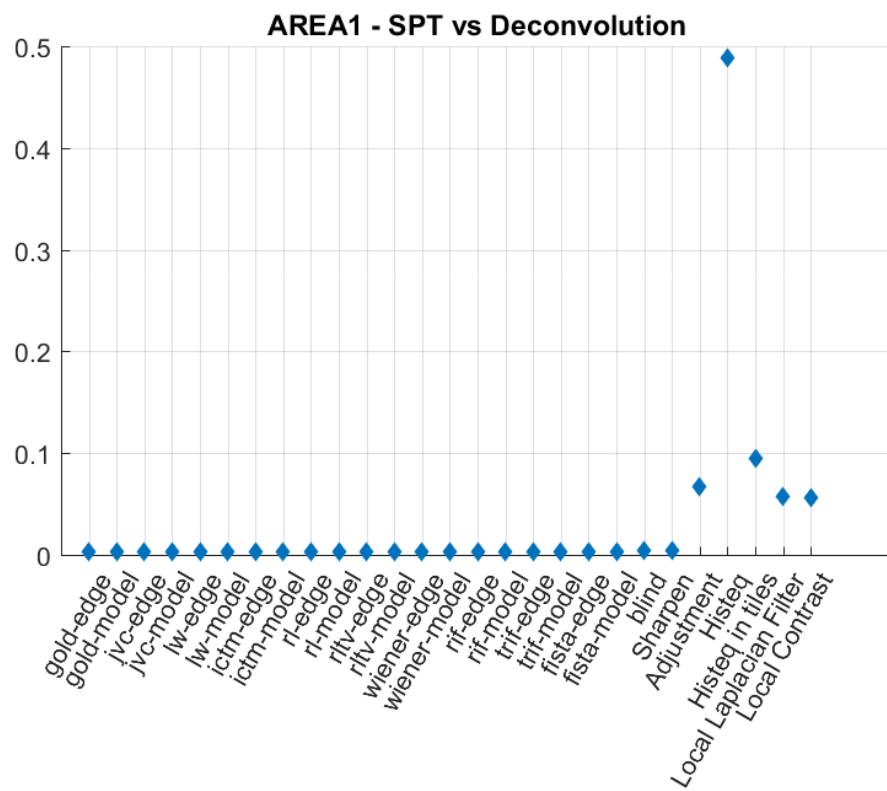


FIGURE 3.14: Standard Processing Techniques comparison

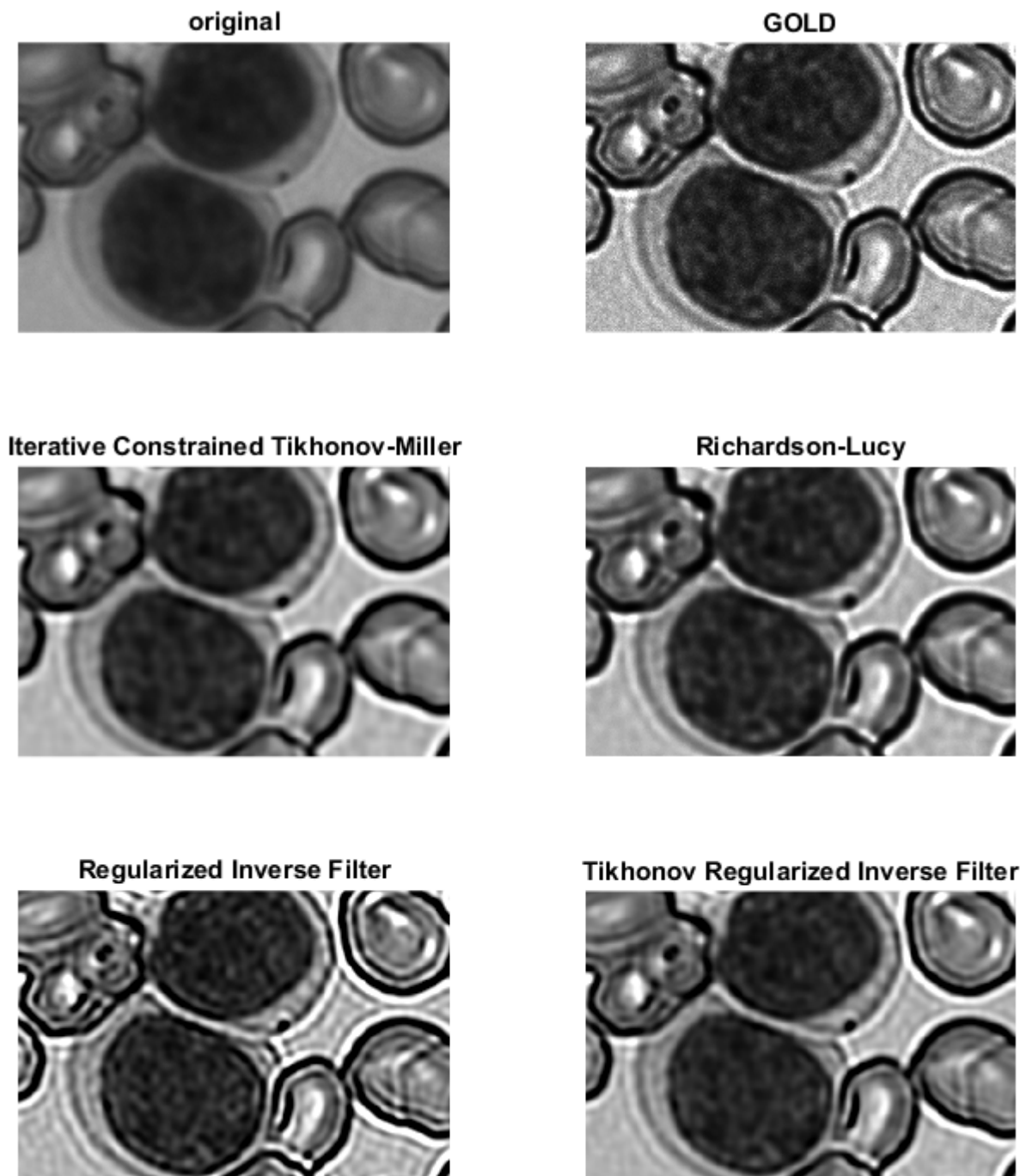


FIGURE 3.15: Deconvolution results with the use of the measured PSF (in comparison with the original image and the Blind deconvolution result).

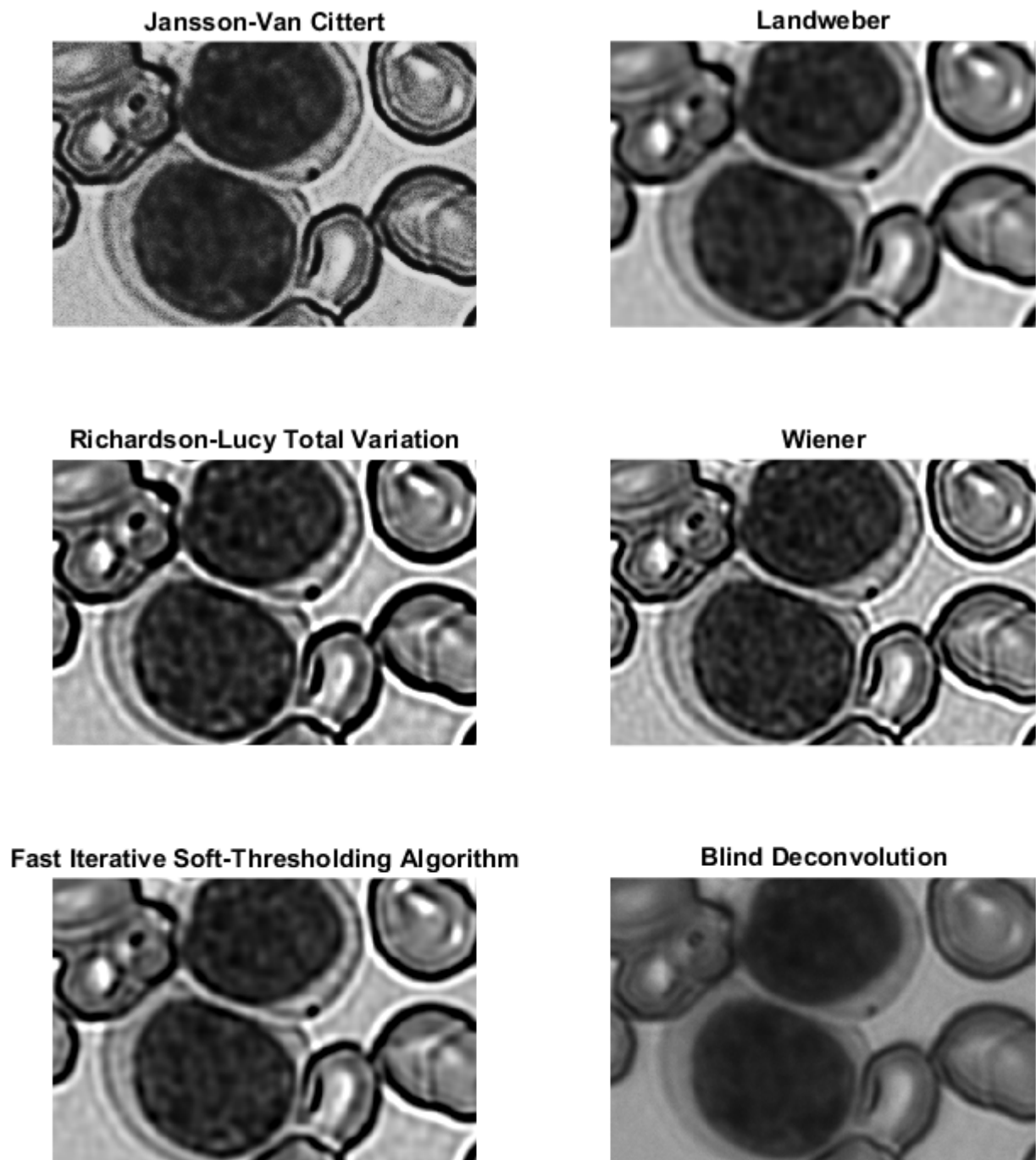


FIGURE 3.16

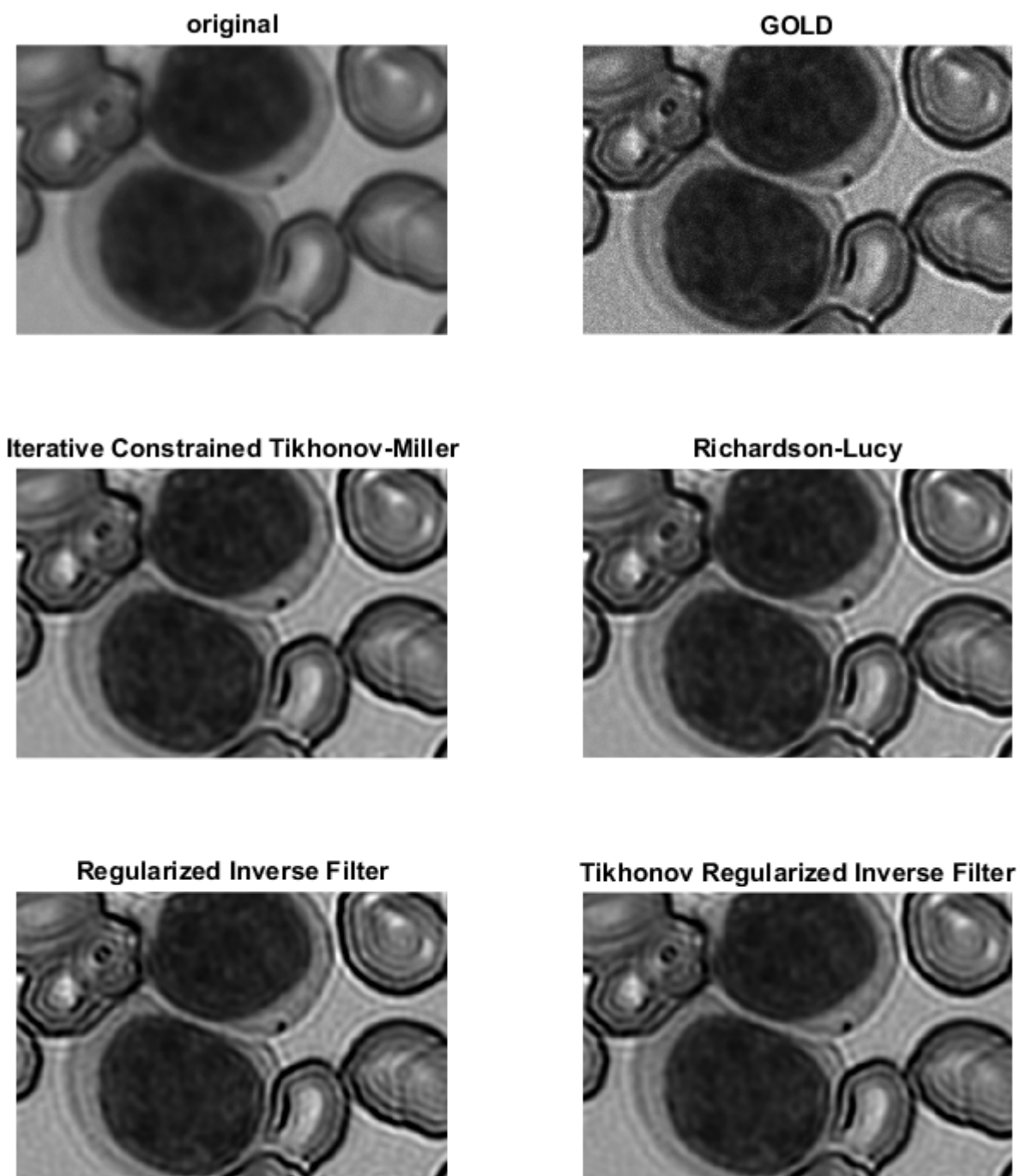


FIGURE 3.17: Deconvolution results with the use of the modelled PSF (in comparison with the original image and the Blind deconvolution result).

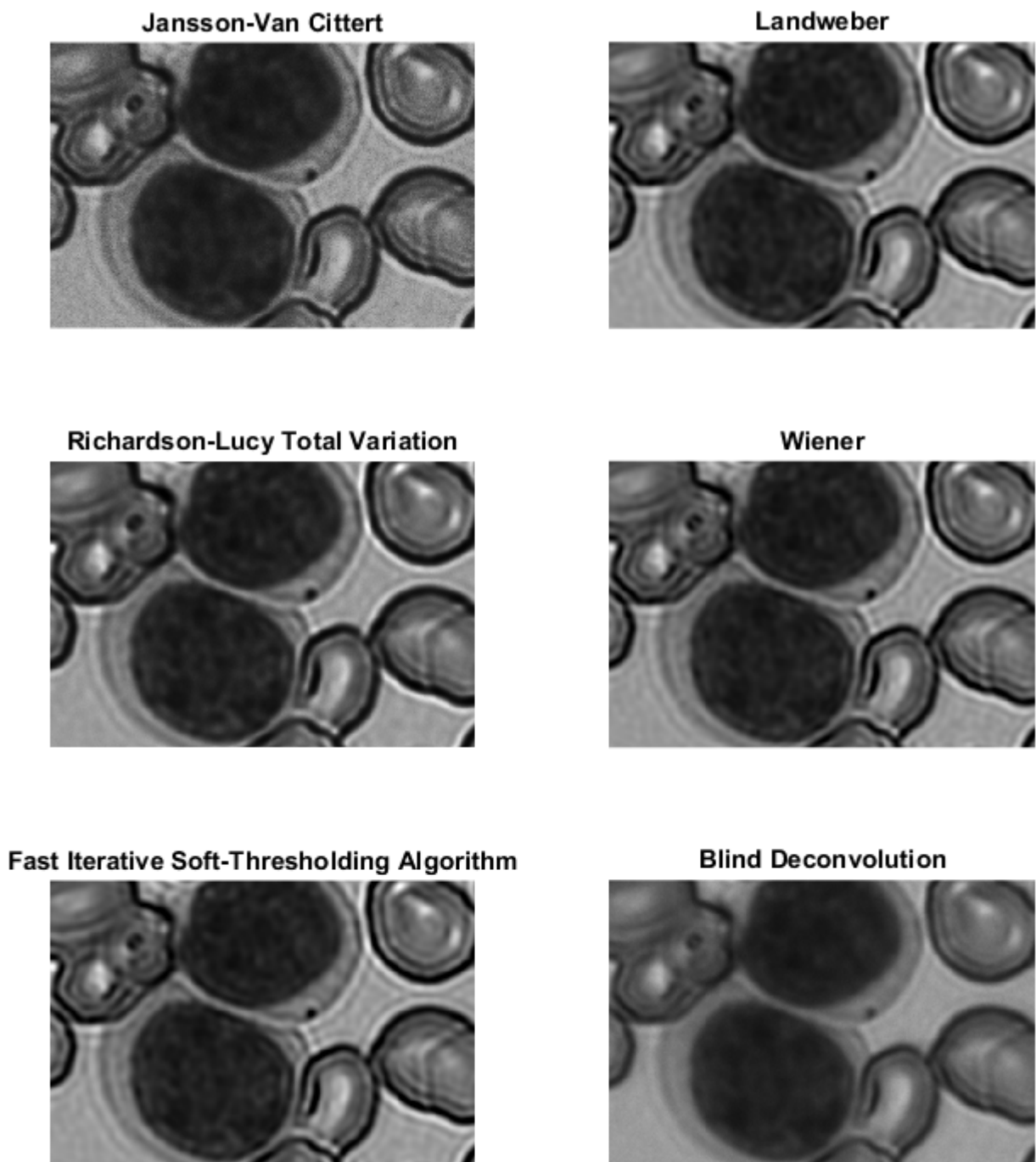


FIGURE 3.18

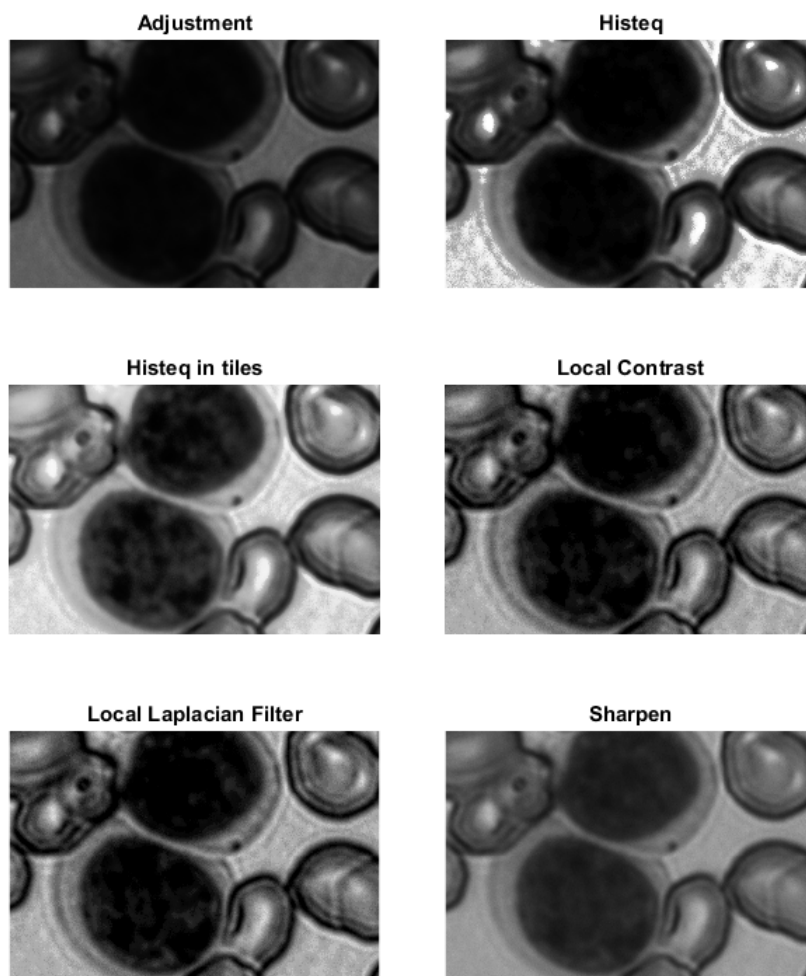


FIGURE 3.19: SPT results

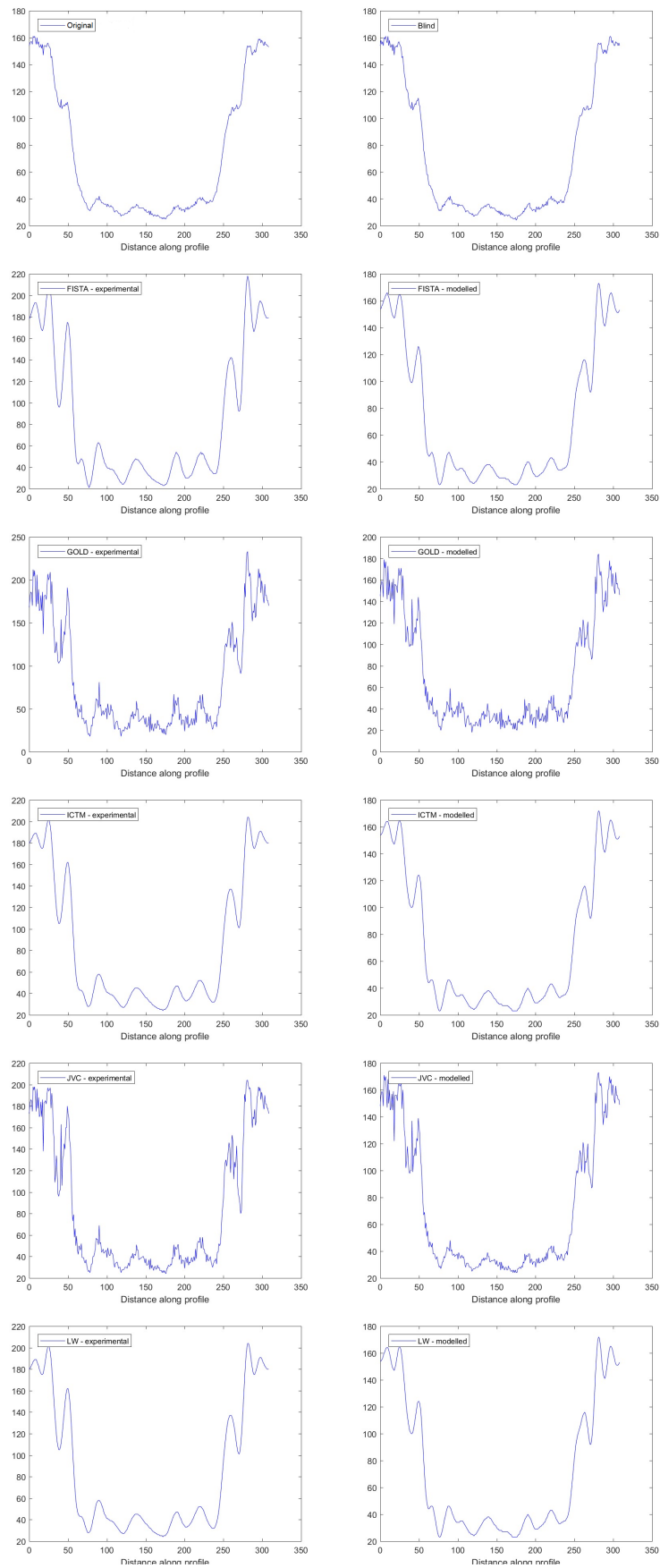


FIGURE 3.20: Intensity profiles

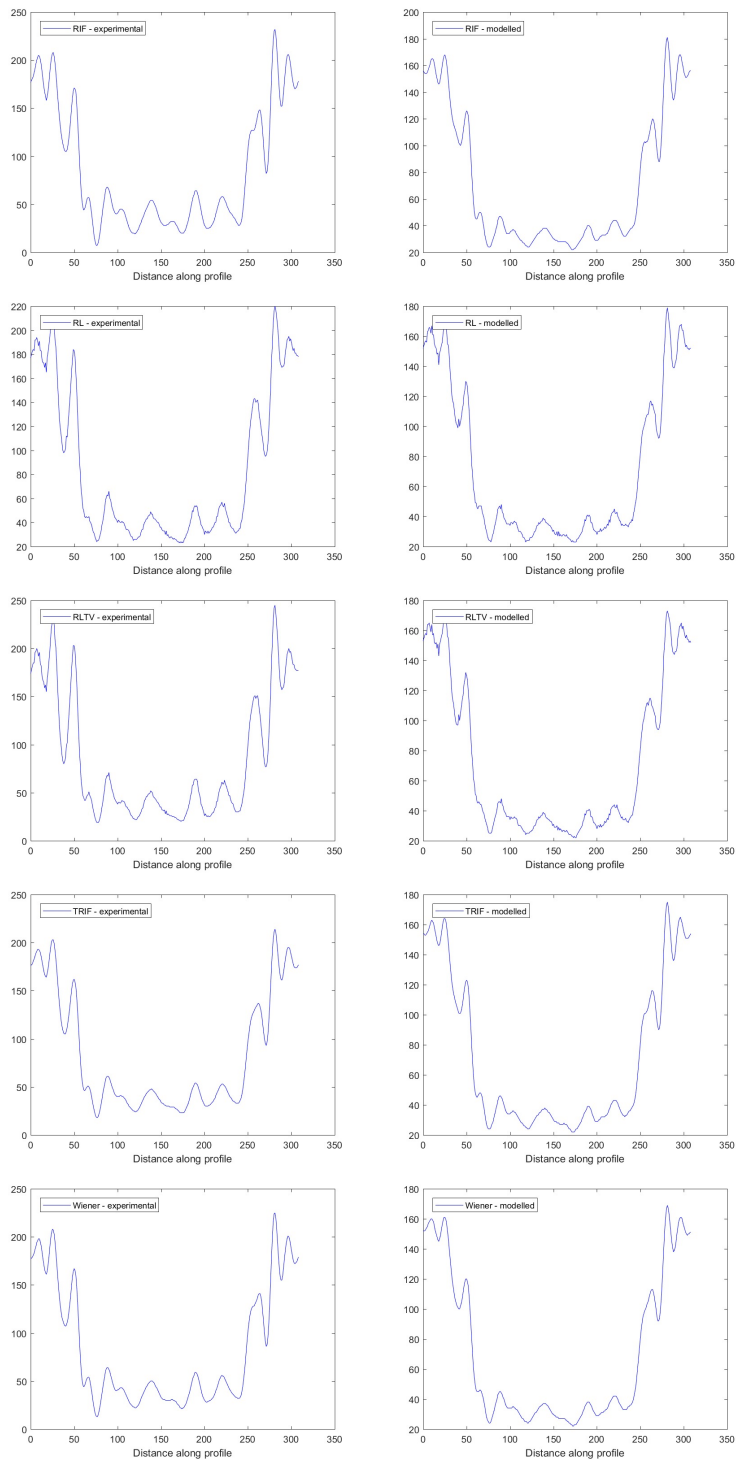


FIGURE 3.21

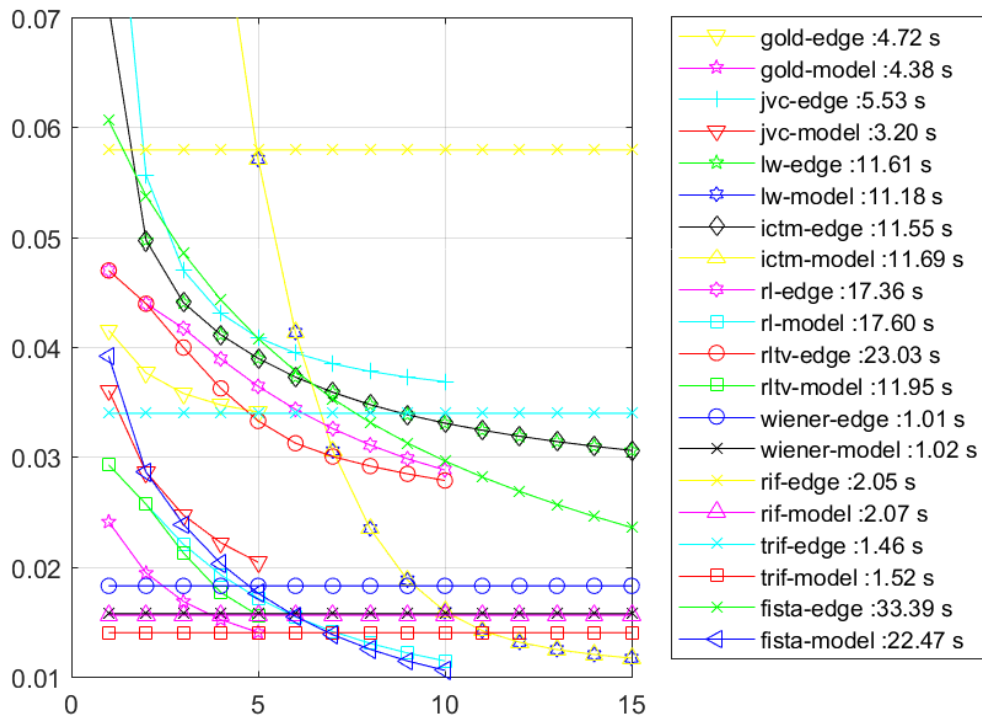


FIGURE 3.22: Convergence of iterative algorithms - execution times

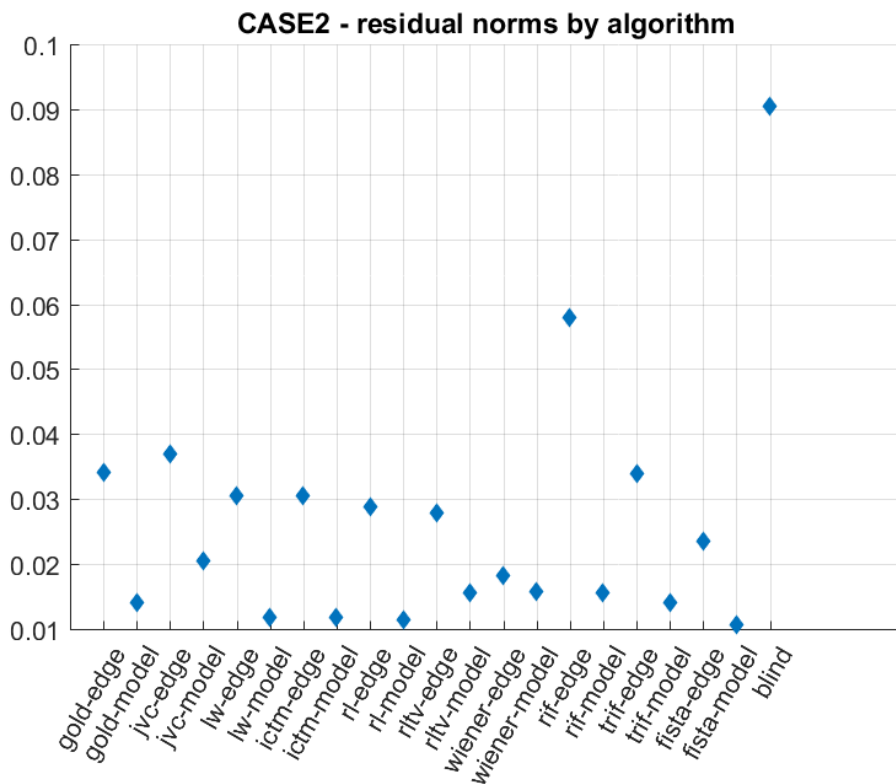


FIGURE 3.23: Residual norms of every algorithm

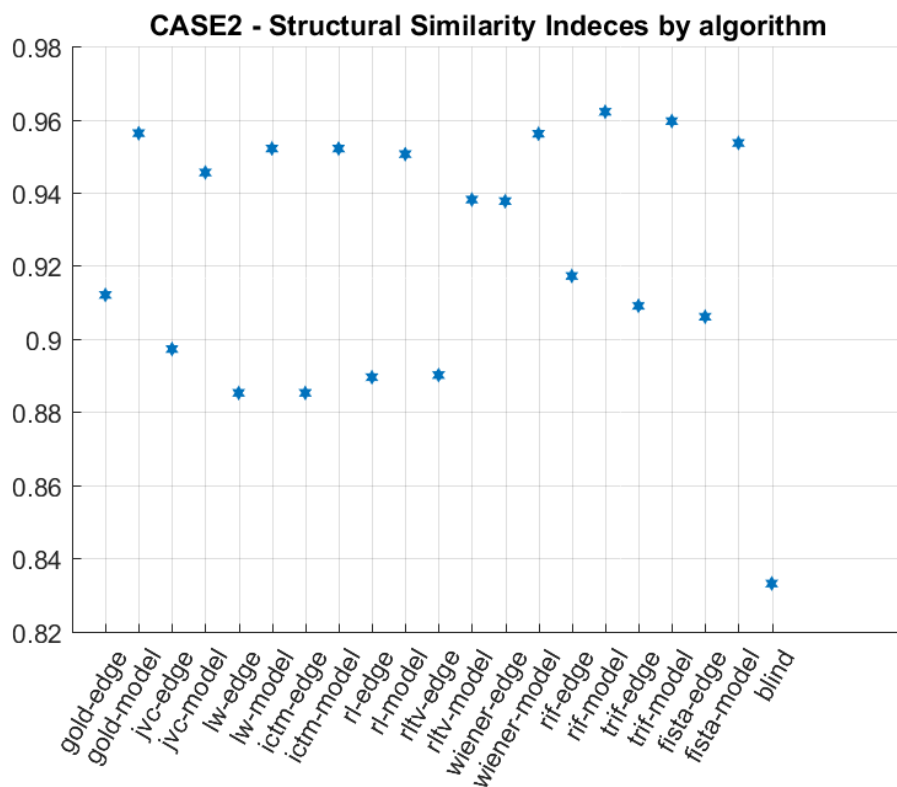


FIGURE 3.24: SSIM of every algorithm

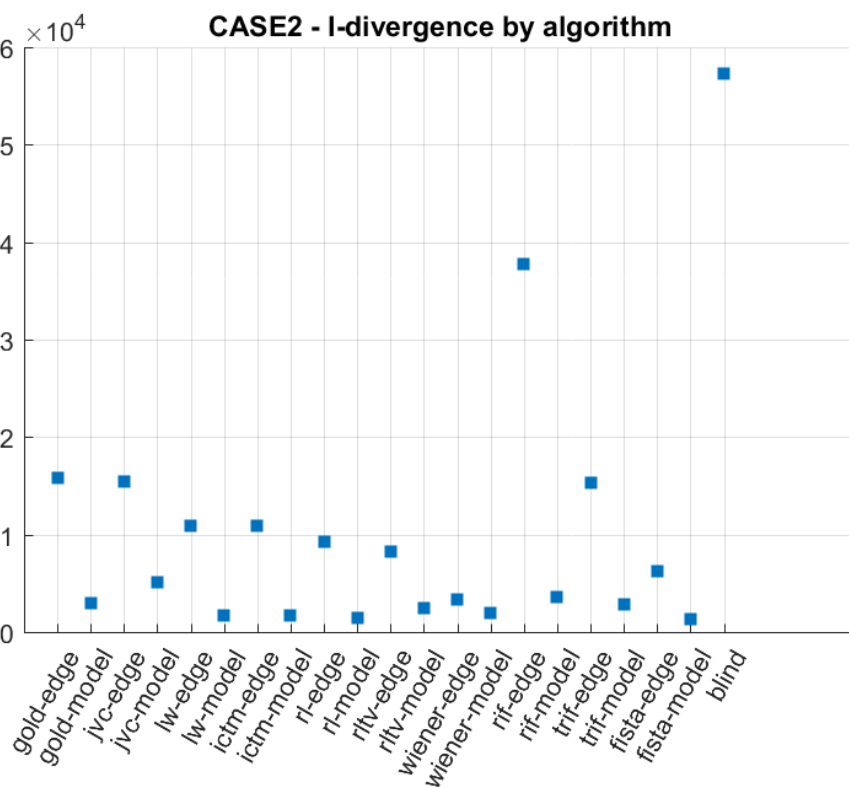


FIGURE 3.25: I-divergence of every algorithm

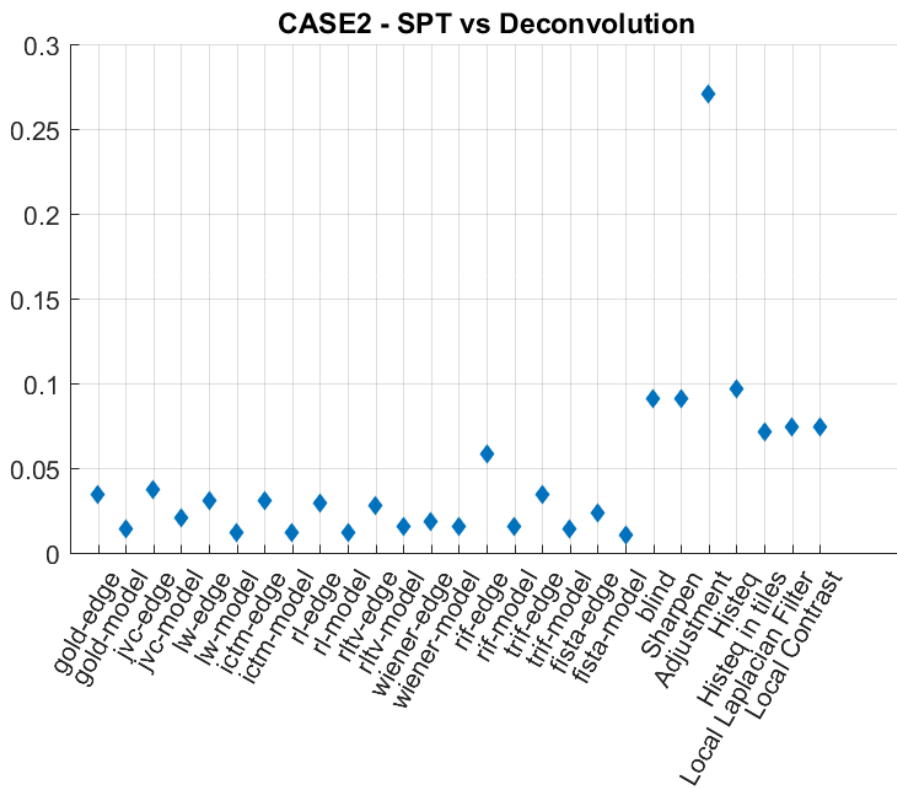


FIGURE 3.26: Standard Processing Techniques comparison

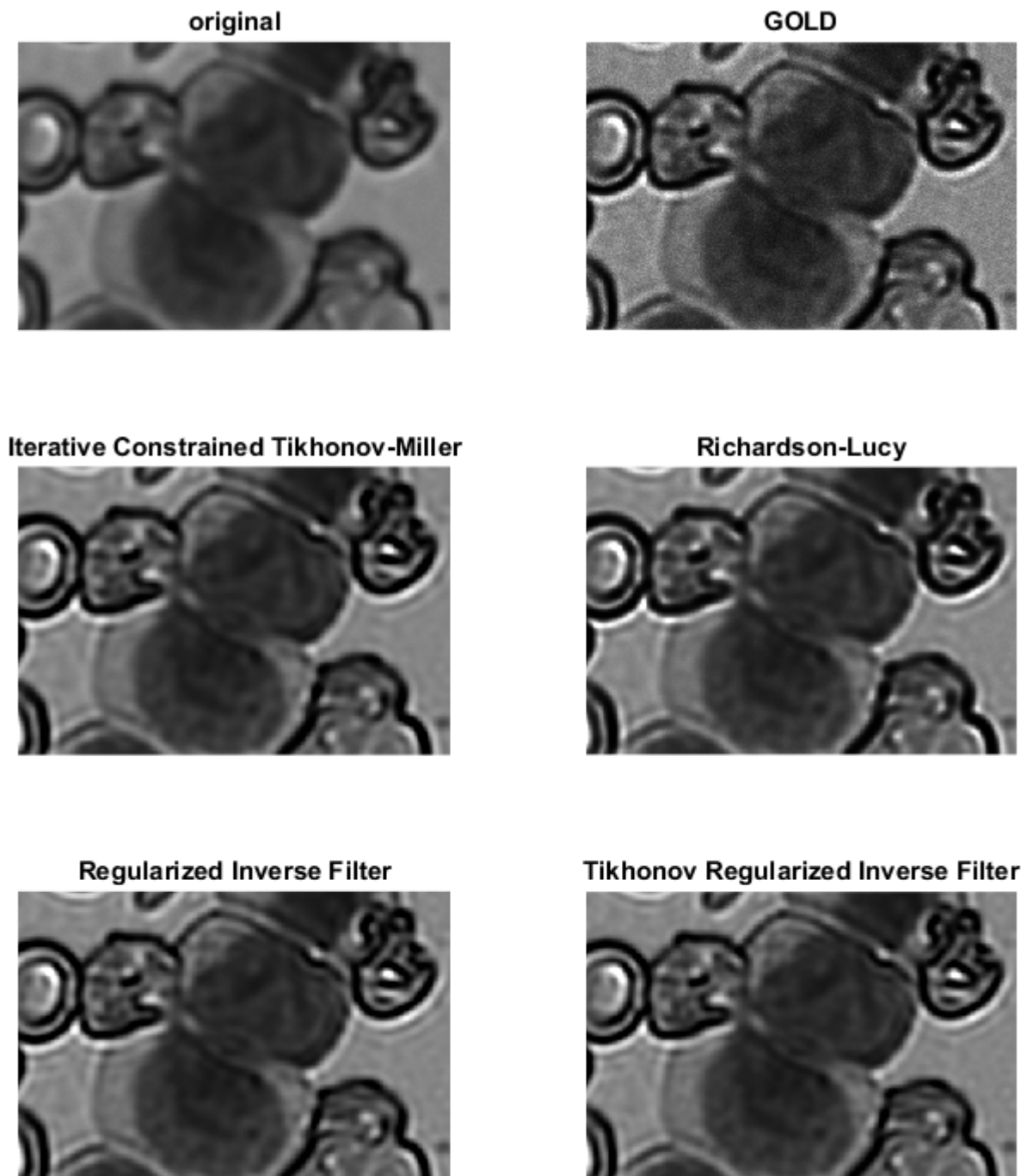


FIGURE 3.27: Deconvolution results with the use of the measured PSF (in comparison with the original image and the Blind deconvolution result).

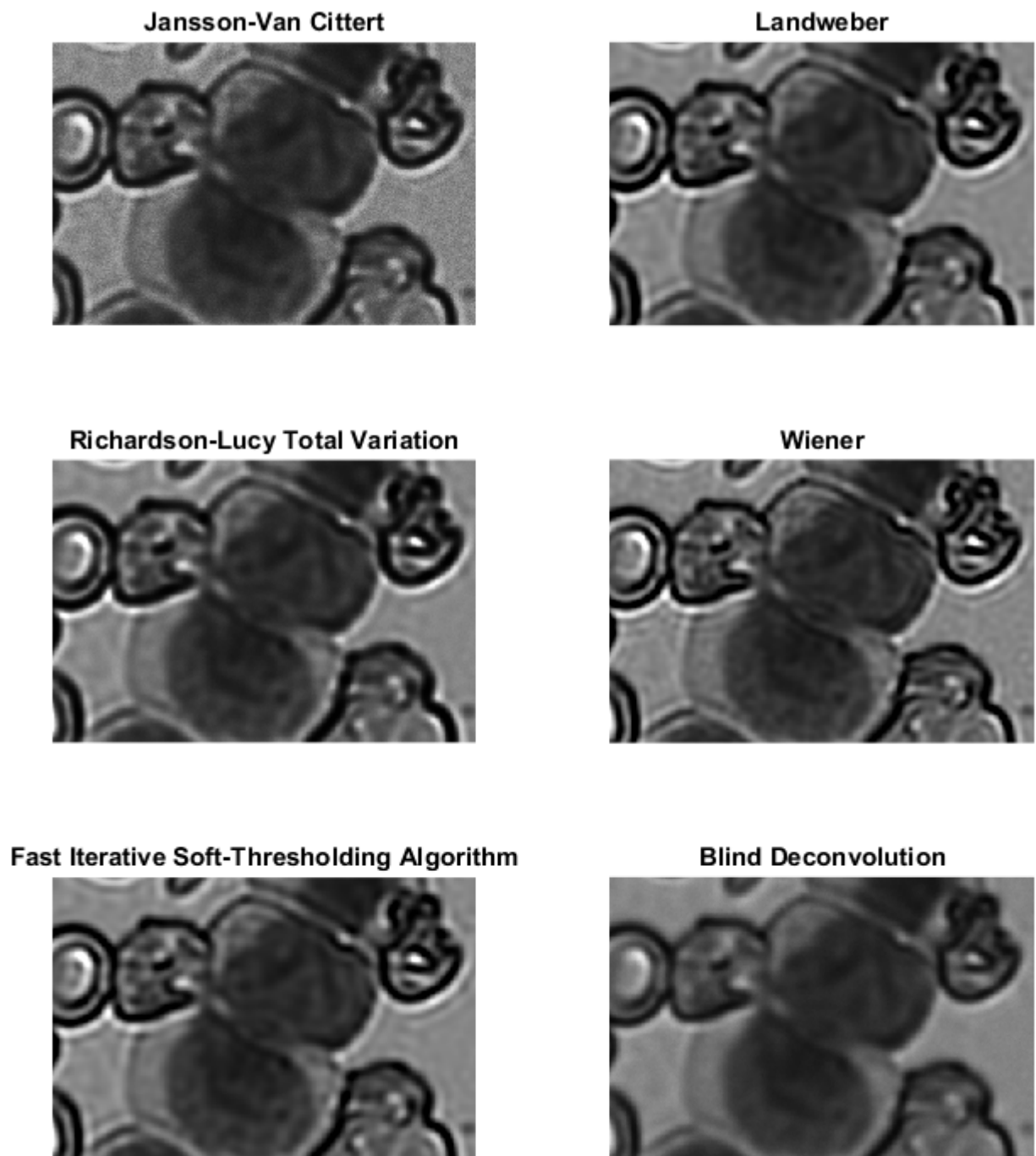


FIGURE 3.28

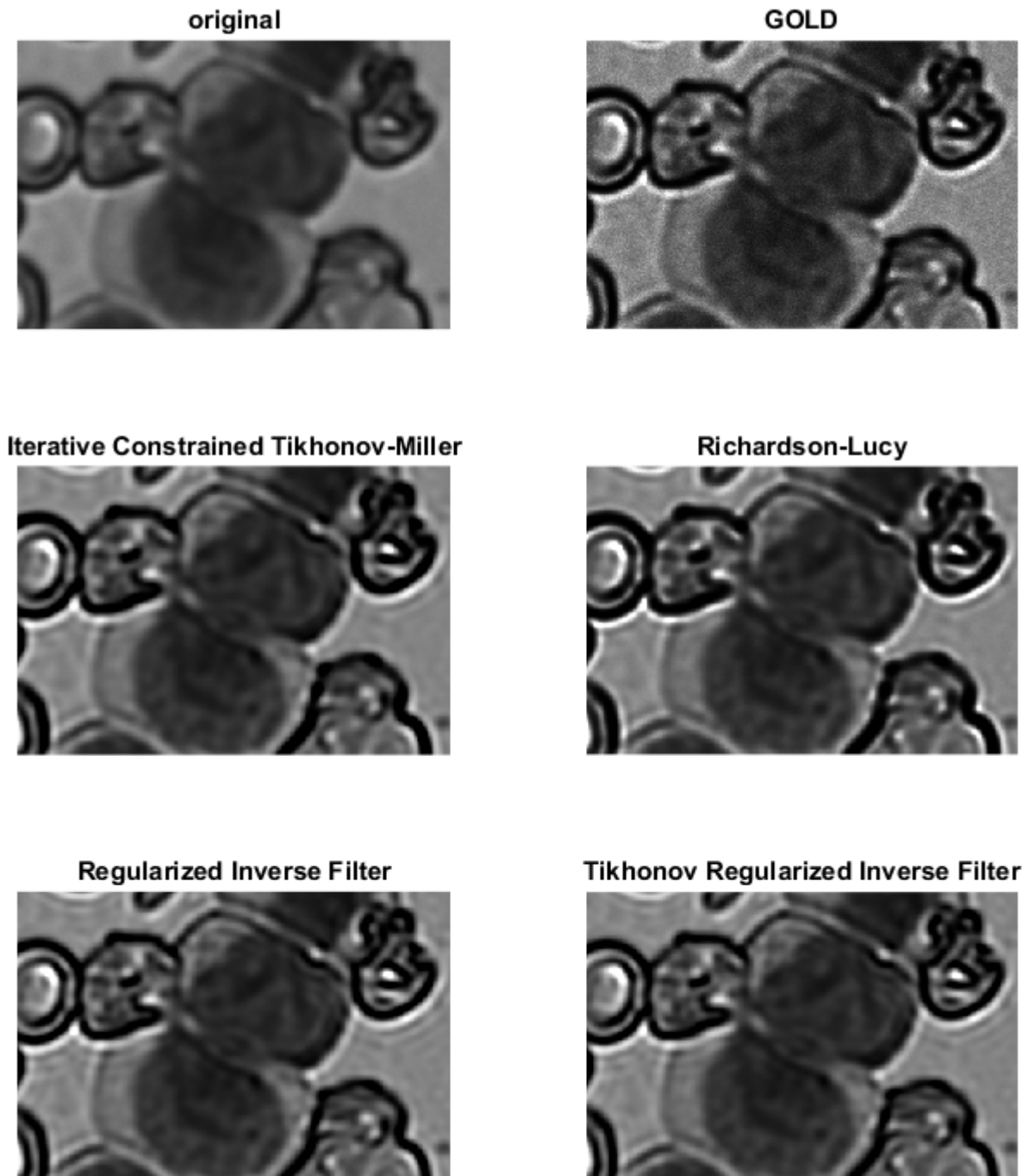


FIGURE 3.29: Deconvolution results with the use of the modelled PSF (in comparison with the original image and the Blind deconvolution result).

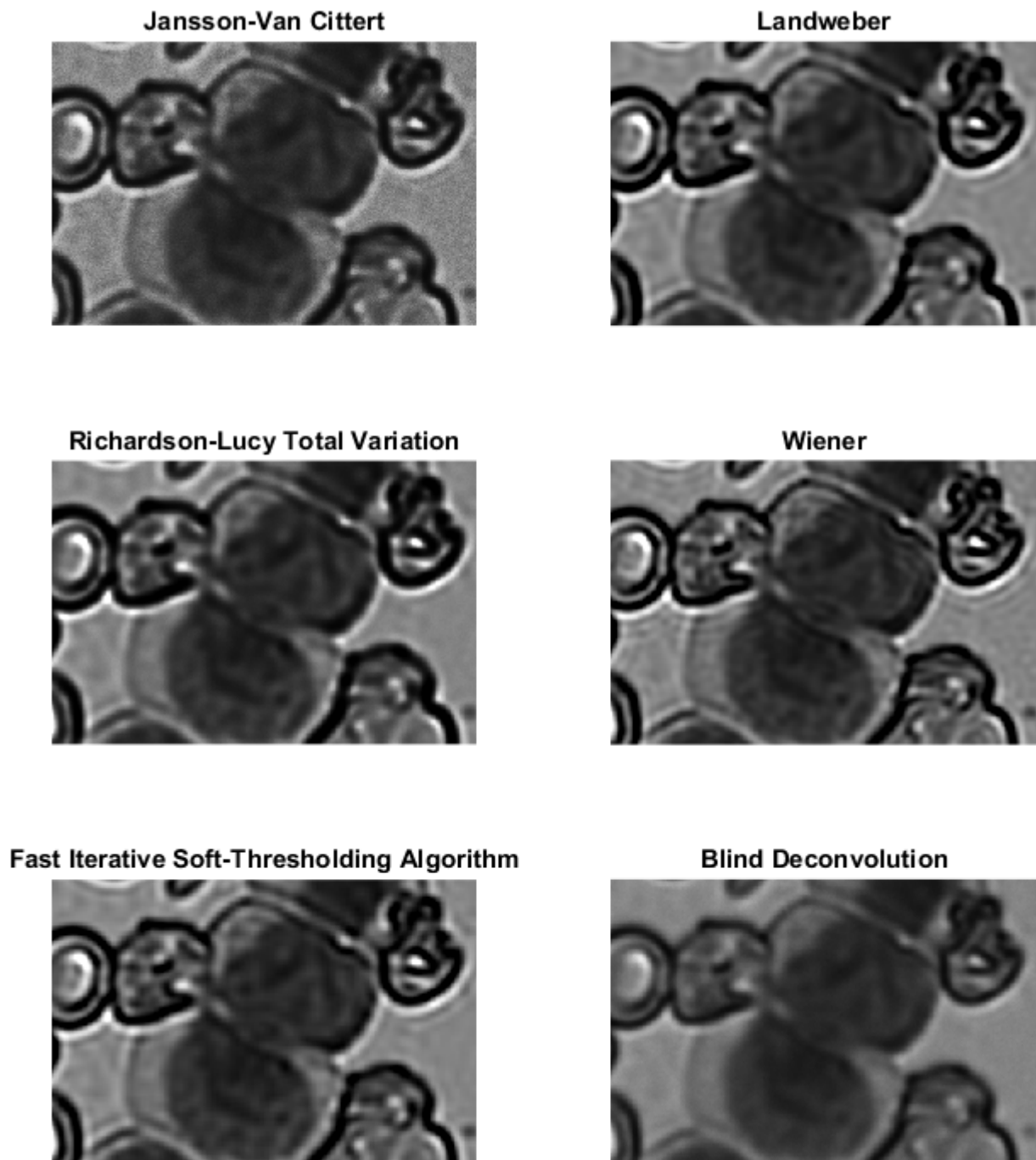


FIGURE 3.30

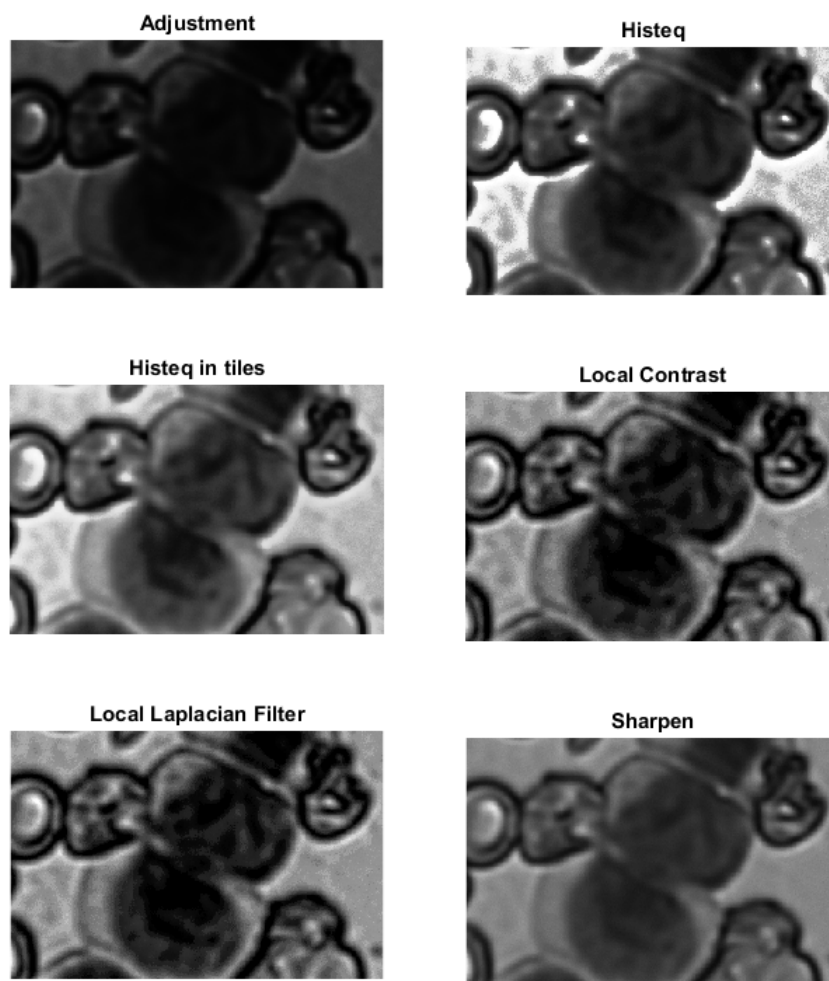


FIGURE 3.31: SPT results

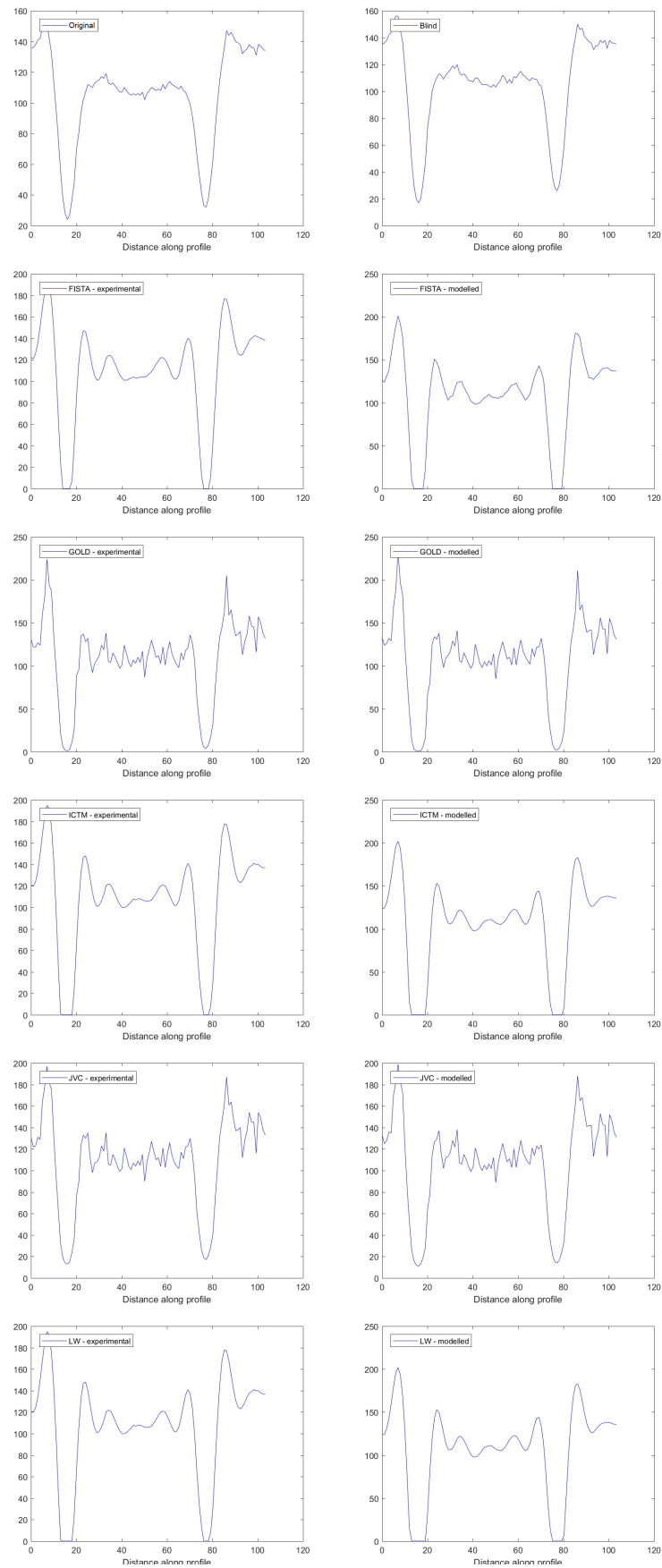


FIGURE 3.32: Intensity profiles

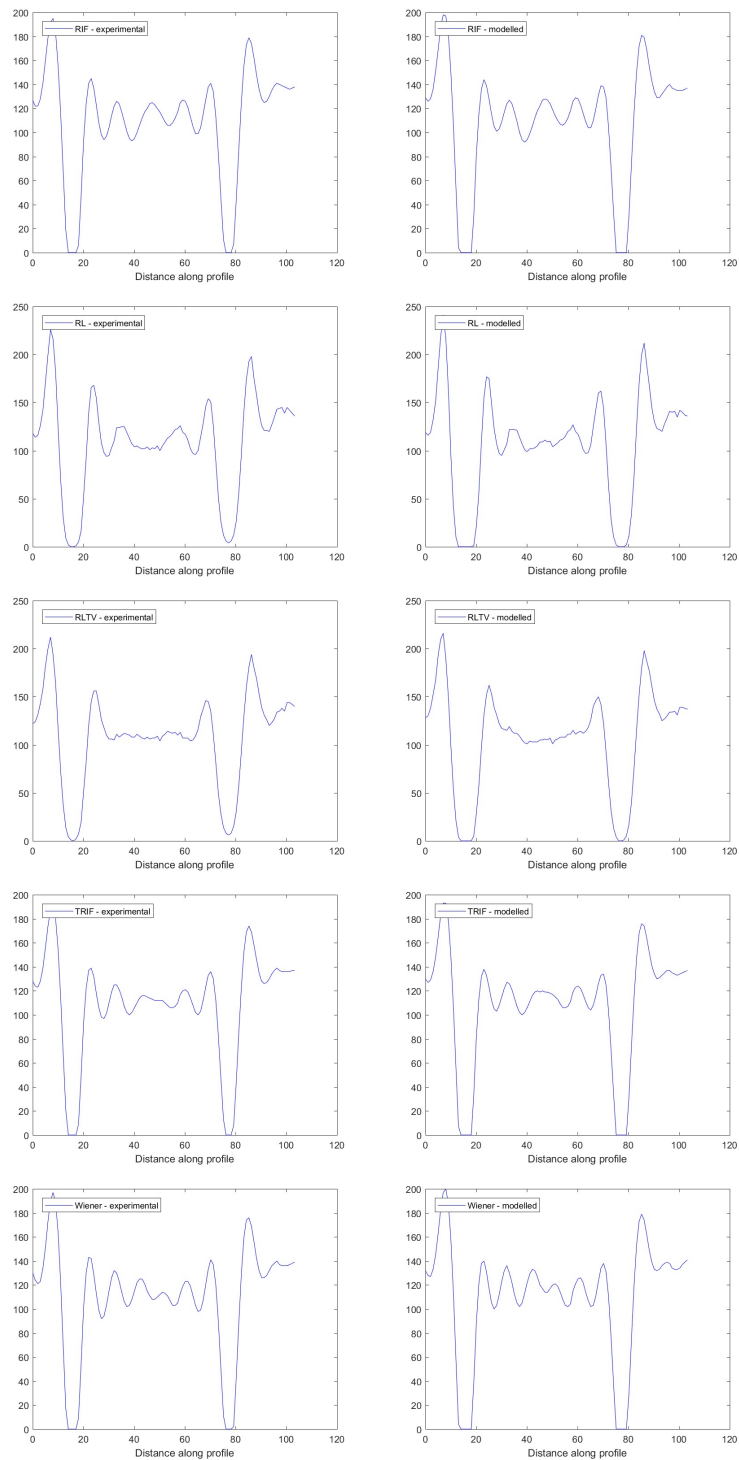


FIGURE 3.33

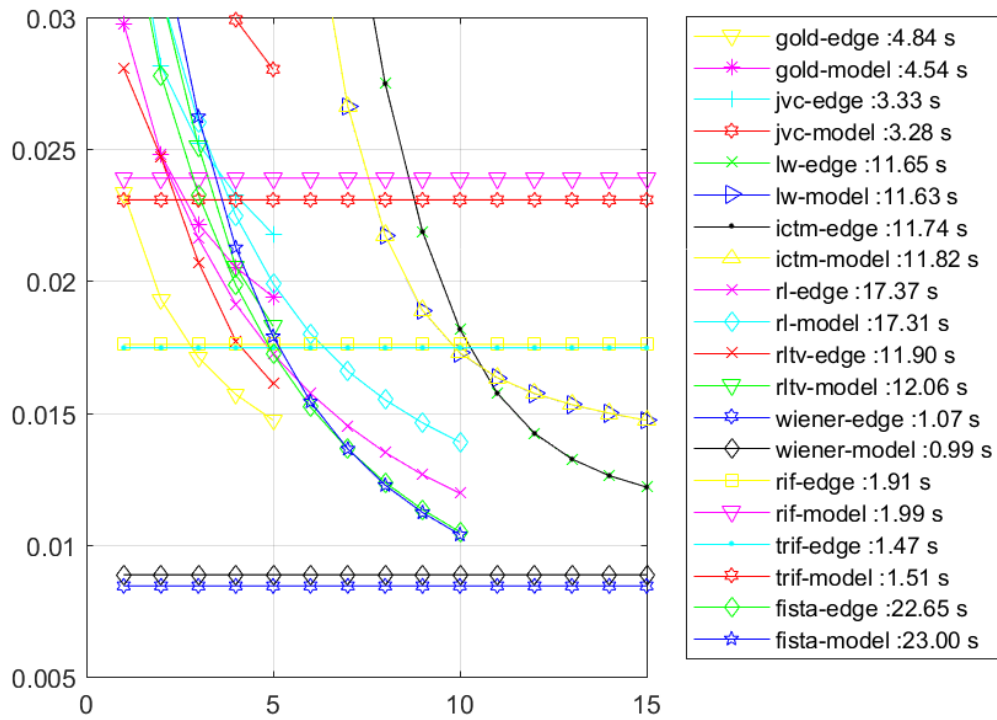


FIGURE 3.34: Convergence of iterative algorithms - execution times

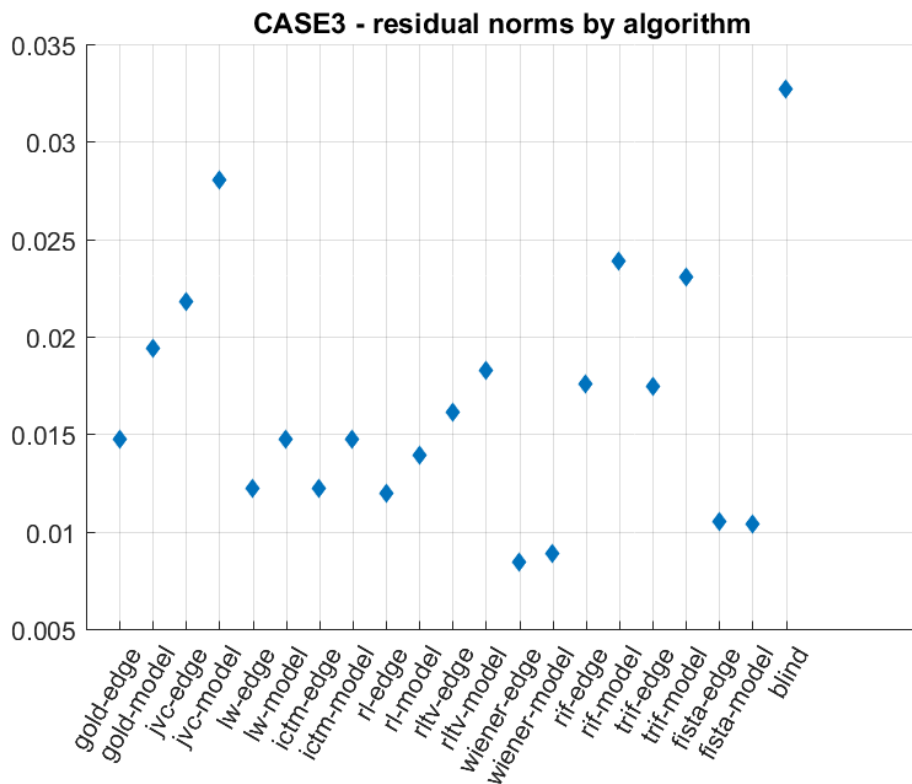


FIGURE 3.35: Residual norms of every algorithm

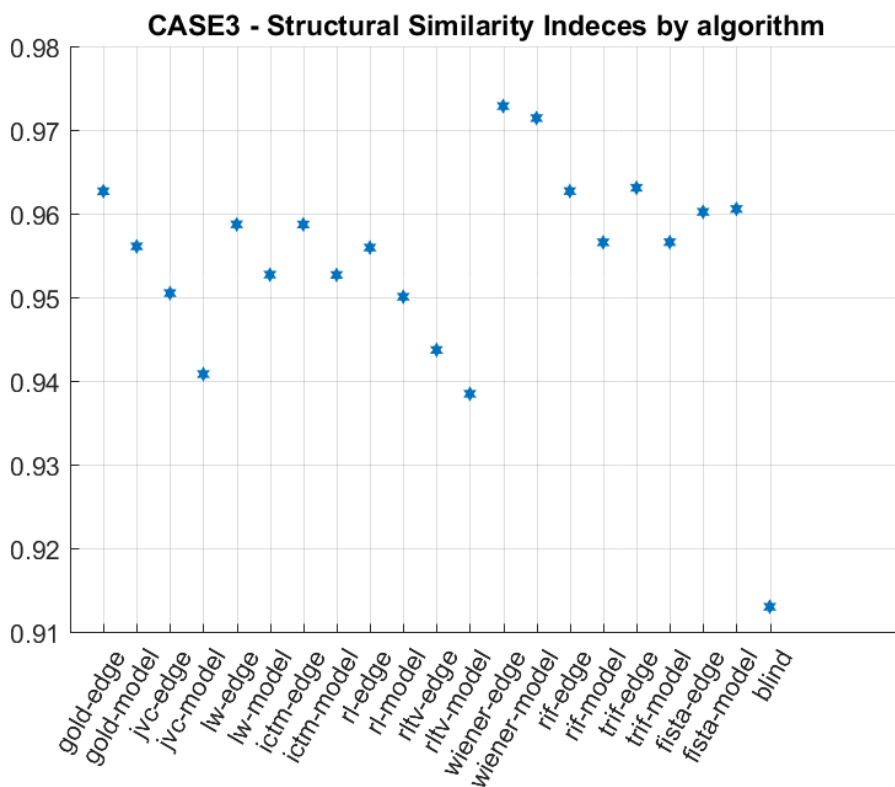


FIGURE 3.36: SSIM of every algorithm

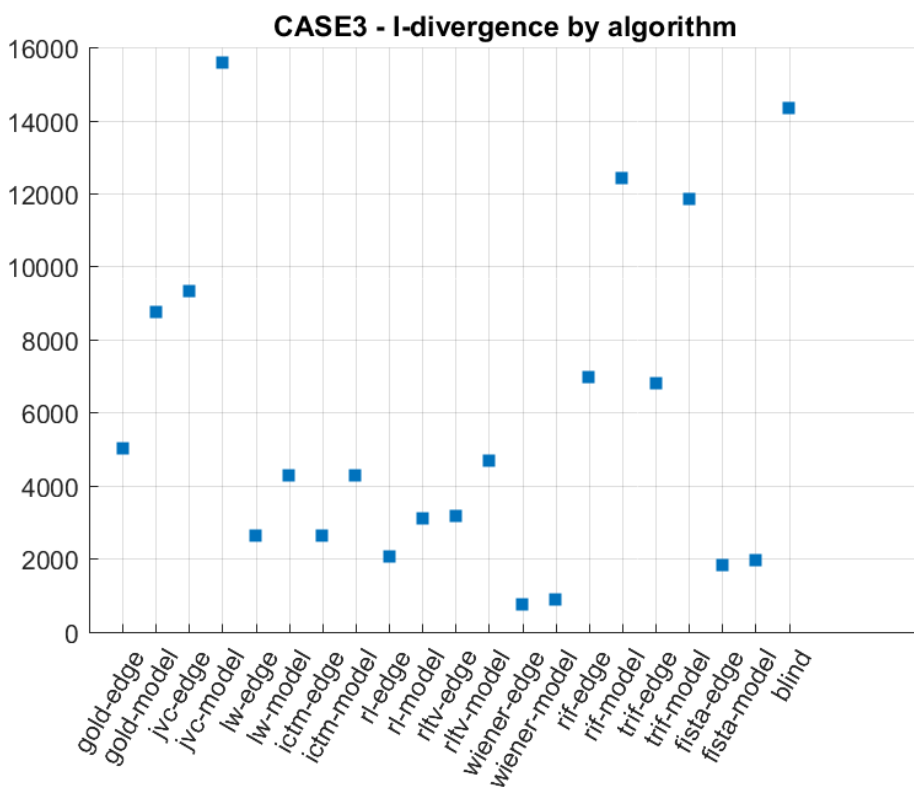


FIGURE 3.37: I-divergence of every algorithm

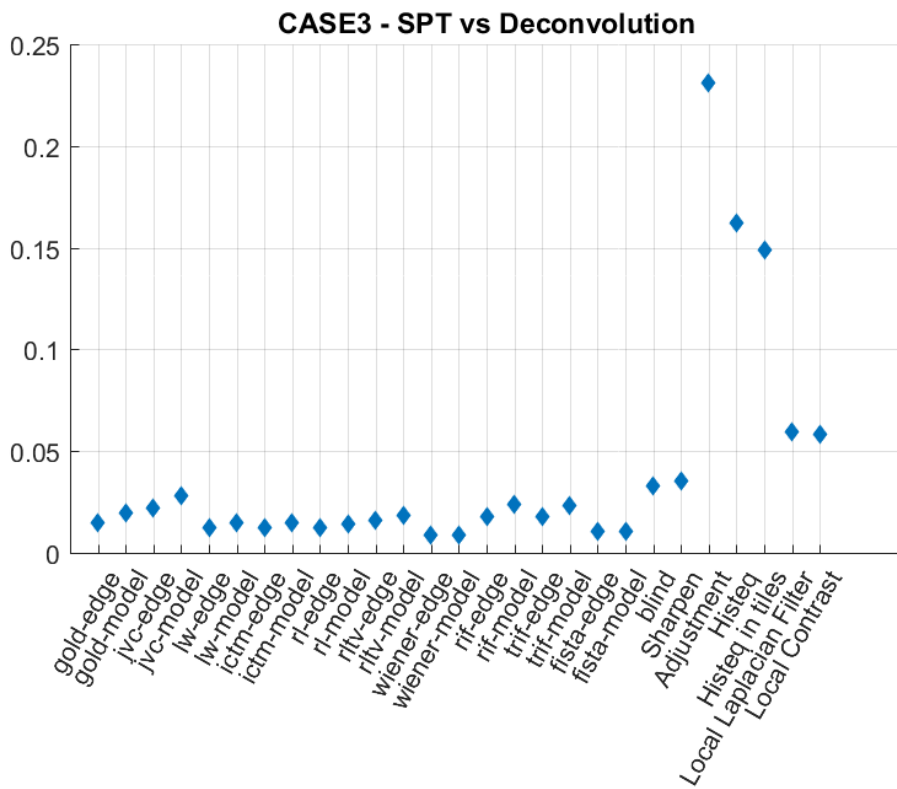


FIGURE 3.38: Standard Processing Techniques comparison

Chapter 4

Explanation of software experiments results

4.1 Conclusions

Residual norm, SSIM and I-divergence compute the overall deviation (with the general meaning of the word) of two images. Each pixel has its own deviation, but the metrics sum all these deviations leading to an overall scalar number-index. This process is prone to non-unique indices, meaning that more than one and probably quite different visually perceived images share the same index. For this reason, the human eye does the last inspection of the deconvolution results. Definitely, as stated on the previous chapter, SSIM is a good compass for choosing a parameter setting for a specific deconvolution algorithm.

On the other hand, speaking apart from the number of pixels in an image, the dynamic range and the presence of noise, human eye assumes that an image is of high quality when it has a high contrast in the useful optical information. As observed in Local Laplacian Filter and Local Contrast results of SPTs (Fig. 3.7-3.19-3.31), they may exhibit a boost of contrast, at least in the region of interest, but at the expense of realism. It is obvious that the images are deformed even if some fibres for example (fluorescence image) are seen more clearly than in the original image.

Now, in the basic subject of the deconvolution outcomes, deconvolved fluorescence and brightfield # 2 images using the corresponding experimental PSF, achieve better results as far as the quantitative metrics are concerned. On brightfield image # 1 it seems that the modelled PSF provide better metrics than the experimental one. This is shown in the corresponding plot and scatter graphs. One can see the metrics results of the deconvolution outcomes in the relative subfolders in the *"/Demos"* folder of the MATLAB implementation (*"/area1_data"* for the fluorescence image, *"/case2_data"* for the brightfield image # 1 and *"/case3_data"* for the brightfield image # 2).

FLUORESCENCE IMAGE

Convergence with respect to the residual norms

Regarding the fluorescence image specifically (Fig. 3.10), it is observed that as the algorithms are set (explained in the previous chapter how), ICTM and LW achieve the **smallest residual norms**. Because the metrics results of these two algorithms seem to be indistinguishable, they will be mentioned as LW-ICTM hereafter. Continuing, after LW-ICTM, the RLTV, RL, RIF, FISTA, GOLD and TRIF algorithms follow. These occasions are with the use of the **experimental PSF**. At this point of the conversation, the time of execution of these methods must be taken into account. Of course, RIF and TRIF as inverse algorithms exhibit the most rapid given solutions

in just 1.5 – 2 seconds. The rest iterative methods that follow RIF and TRIF, reach execution times ranging from 10 to 18 seconds. This is definitely quite a big difference among inverse and iterative algorithms. As an extra deduction from the convergence graph, RL and RLTV are of greater rapidness as opposed to FISTA which need the double number of iterations to reach a satisfactory residual norm. RLTV generally and as seen in the graph too, exhibits slightly better results for the same number of iterations than RL despite the extra and time-consuming Total Variation integration. In total, two cases differ blatantly from the others. Gold diverges from the very beginning and Blind deconvolution does almost no work at all. *In conclusion, as far as the residual norms are concerned, the experimental PSF yields better results than the modelled one.*

Certainly, constraints regarding visual perception of the images and speed of algorithms must be included in order to have a complete view before arriving to any final conclusions. Visual perception may falls to the field of subjectivity, but it is obligatory since images are used by humans as diagnostic tools and they have to be in position to discern useful information in an image. In addition to this, one may have a look at the intensity profiles to compare the original image with the deconvolved one with the experimental PSF along with the modelled PSF. However, it might be unclear if higher contrast in the intensity profile means more details or more noise. For this reason, the intensity profile of the original image must be used necessarily as a reference. Hence, keeping what is mentioned above in mind, with an operation of visual examination, it is deduced that the order of the best algorithms as set based on the residual norms only, changes into **RIF,LW-ICTM,RLTV,RL**. If though, in some applications, execution time of up to 10 seconds is not crucial, the LW-ICTM could be preferred, even though visual differences are not too strong.

I-divergence

Using I-divergence in order to compare the results, a new view of them emerges. The inverse Wiener algorithm, which is the fastest of all with 1 second of execution time, using the experimental PSF exhibit the best outcome. TRIF, RLTV, RL, and LW-ICTM follow. Again the results relative to the experimental PSF, provide a lower metric result, with I-divergence being smaller than in the results with the modelled PSF.

Including visual and speed constraints, the above-mentioned order changes a bit and becomes **LW-ICTM, RL, RLTV, Wiener and TRIF**. If though, execution time is crucial, Wiener could be preferred, even though it exhibits little ringing effects and the visual differences are clear.

SSIM

As with I-divergence, SSIM outcomes show that Wiener with the experimental PSF behave better. More specifically, Wiener, TRIF, GOLD, RLTV and LW-ICTM act as the best methods. Once again, using the experimental PSF yields results with higher SSIM indeces. Consequently, SSIM is the third quantitative metric that validates the argument that deconvolution of an observed image of an object with an experimental PSF provides an image which is closer to the true underlying image of this object.

With visual and speed constraints, the best-order changes into **LW-ICTM, RLTV, GOLD, Wiener, TRIF**. Again, if execution time is crucial then Wiener could be preferred, despite its ringing effect problem.

BRIGHTFIELD IMAGE # 1*Convergence with respect to the residual norms*

Deconvolution with this specific brightfield image gives a quite different view. The modelled PSF seems to yield better results with respect to the residual norm as it is seen in Fig. 3.22. Observing the convergence graph, results with the use of the experimental PSF and those with the modelled one are very distinguishable, like forming two clusters of convergence curves. The lower cluster corresponds to the modelled PSF. More specifically, FISTA yields the lower residual norm and RL, LW-ICTM, TRIF and GOLD follow, with the last two sharing the same residual norm.

With the visual and speed constraints, this order changes into **TRIF, LW-ICTM, GOLD, RL, FISTA**.

I-divergence

Regarding this metric, the best-order is formed as: FISTA, RL, LW-ICTM, Wiener, RLTV. By visual examination and speed constraint inclusion, this order changes into: **Wiener, LW, RLTV, RL, FISTA**.

SSIM

Regarding SSIM, the best-order is as: RIF, TRIF, Wiener, GOLD, FISTA and LW-ICTM. Wiener and Gold share the same metric value. With visual examination and speed constraint taken into account, this order changes into: **Wiener, LW, TRIF, RIF, GOLD, FISTA**. Of course, again if execution time of up to 10 seconds is forbidding in some applications, Wiener, TRIF and RIF could be preferred.

BRIGHTFIELD IMAGE # 2*Convergence with respect to the residual norms*

On this occasion, as far as the experimental and modelled PSFs are concerned, the results are "mixed up". The best-order of the algorithms with respect to the residual norm is: Wiener(experimental PSF), Wiener(modelled PSF), FISTA(modelled), FISTA(experimental), RL(experimental), LW-ICTM(experimental), RL(modelled). Taken visual and speed factors into account, FISTA is the least preferred algorithm, since it is the most timeconsuming (double execution time compared to LW-ICTM) and with subtle visual differences. The only drawback of Wiener on this occasion, is the more noticeable ringings as opposed to the iterative algorithms that exhibit almost no ringing effects. However, the useful information of the image (inside the cells) as viewed by the human eye, remains intact. Hence, Wiener should be preferred among the other algorithms. To tidy this up, from the view of algorithms, the best-order including speed and visual examination becomes: **Wiener, RL, LW-ICTM and FISTA**.

I-divergence

Regarding this metric, the best-order is: Wiener(experimental PSF), Wiener(modelled), FISTA(experimental), FISTA(modelled), RL(experimental), LW-ICTM(experimental). This order changes if visual and speed factors are taken into account and from the view of algorithms only, becomes: **Wiener, RL, LW-ICTM and FISTA**. For a particular algorithm, using the experimental PSF or the modelled one, makes no noteworthy difference for the eye.

SSIM

Finally, SSIM shows the following best-order: Wiener(experimental PSF), Wiener(modelled PSF), TRIF(experimental), GOLD(experimental), FISTA(modelled), FISTA(experimental). TRIF and GOLD share the same metric value. Now, with the visual and speed constraints, no changes are made in this specific order. That is, from the view of algorithms only, it is: **Wiener, TRIF, GOLD, FISTA**.

CONCLUSION

On some occasions, even though FISTA yields better results, with respect to the metrics, from the majority of the other algorithms, it is the last algorithm to be preferred because it is the slowest. Again, if the execution time is not forbidding for some applications, it should be characterized as the best option for deconvolution. Apart from the metrics results, wavelet decomposition does NOT amplify the possible ringing effects and it may eradicate completely some regions that consist false information, such as marks of the coverslip of the microscope which are evident in the brightfield cases.

Between the fluorescence image and the two brightfield ones, it is easily seen that deconvolution outcomes of the latter are quite improved and much more as opposed to the former. This can be explained since brightfield images contain much more optical information than the fluorescence ones. Deconvolution in general, cannot reconstruct lost signals. So, if the optical signal is meagre, deconvolution cannot enhance the image as good as it does in the brightfield occasion.

Regarding the comparison of the experimental PSF and the modelled one, there is a contradiction between the outcomes of the metrics and the images as perceived visually by the human eye. One can say that on the occasions where the quantitative metrics show better results using the experimental PSF, the deconvolved images with the modelled PSF exhibit better resolution. This can be also said for the converse case where modelled PSF yield better metrics than the experimental one. In general, what is perceived as good by the eye does not necessarily mean that it is in agreement with reality. But specifically in the brightfield image # 2 it can be noticed that when comparing the deconvolution outcomes of the experimental and the modelled PSF with the original image, the outlines of the depicted cells and other details in the image are thickened in the case of the modelled PSF which yields worse results of the metrics but it is perceived as better visually. The same applies for the fluorescence image, even though it is not so evident as in the brightfield image. Regarding the brightfield image # 1, the results of the metrics show a superiority of the modelled PSF, but when the image is deconvolved with the experimental PSF, the results please the human eye more.

Consequently, this is a trade-off situation. If deconvolution applications do not include quantitative measurements of cells for example, with precision being of high significance, then deconvolution outcomes more pleasant to the eye can be preferred.

4.2 Discussion

The results shown in this work were produced via a meticulous examination of the possible parameters that each algorithm can be set with. It is known that Image Processing as a field is not fully independent from the human factor, meaning that visual perception of images in many cases may contradict with the mathematical models, relations or results in general. As an evaluation of the deconvolution results, three quantitative metrics were used as explained in the previous chapter. However, only SSIM in particular seems to be a satisfactory match between the math integrated in the algorithms and the human eye. So, a method has yet to be designed that will act as compass for the development of new algorithms without the so far obligatory inclusion of a human to validate or dismiss their results. This may fall in the field of Deep Machine Learning which in fact has proved to yield tremendous results when it comes to image processing.

As for the PSF estimation, due to the complexity of the inherent physical limits and the possible deviations of an optical train from the ideal one in a microscope, mathematical models need to be very intricate involving parameters that may be not known while being in the process of image acquisition. For this reason, experimental methods in general and apart from the testing that was operated in the current work, seem to be preferable since they incorporate every misalignment and every aberration of the optical system and do not demand detailed knowledge of it. Consequently, the main weight of potential efforts in that domain need the development or enhancement of new or current experimental methods instead of more detailed mathematical models.

Bibliography

- [1] Mortimer Abramowitz, Kenneth R. Spring, and Michael W. Davidson. “Introduction to Lenses and Geometrical Optics”. In: (). URL: <http://www.olympusmicro.com/primer/lightandcolor/lensesintro.html>.
- [2] Mortimer Abramowitz et al. “Anatomy of the Fluorescence Microscope”. In: (). URL: <http://www.olympusmicro.com/primer/techniques/fluorescence/anatomy/fluoromicroanatomy.html>.
- [3] Costas Balas. “Advanced Topics in Electronic Imaging-HPY 603 - Lecture 7: Microscopy Basics. Lecture notes”. In: (), pp. 2–5,8.
- [4] Costas Balas. “Transport phenomena - Basic Optics. Lecture notes”. In: (), pp. 18–21,28–34.
- [5] M. Born and E. Wolf. “Principles of Optics, 7th edition”. In: *Cambridge University Press*, Chapter 8.5 (2003), pp. 436–445.
- [6] *Brownian Motion*. URL: <http://fyzikalnipokusy.cz/1944/brownian-motion>.
- [7] Peter Burns. “Slanted-Edge MTF for Digital Camera and Scanner Analysis”. In: *Review of Scientific Instruments* ().
- [8] I. Csiszar. “ I -Divergence Geometry of Probability Distributions and Minimization Problems”. In: *The Annals of Probability* Vol. 3.No. 3 (1975). Ed. by Institute of Mathematical Statistics. URL: <http://www.jstor.org/stable/2959270>.
- [9] Ferréol Soulez Denis Fortun Guillaume Schmit Arne Seitz Romain Guet Cédric Vonesch Michael Unser Daniel Sage Lauréne Donati. “DeconvolutionLab2: An open-source software for deconvolution microscopy”. In: *Methods* Vol. 115 (2017), pp. 28–41. URL: <http://www.sciencedirect.com/science/article/pii/S1046202316305096>.
- [10] The Editors of Encyclopaedia Britannica. “Aberration OPTICS”. In: (). URL: <https://www.britannica.com/technology/aberration>.
- [11] Brian Herman et al. “Basic Concepts in Fluorescence”. In: (). URL: <http://www.olympusmicro.com/primer/techniques/fluorescence/fluorescenceintro.html>.
- [12] Will Hossack. “Operation of Simple Lens”. In: (), pp. 5–6. URL: <http://www2.ph.ed.ac.uk/~wjh/teaching/mo/slides/lens/lens.pdf>.
- [13] *Image Filtering and Enhancement*. URL: <https://www.mathworks.com/help/images/image-enhancement-and-restoration.html>.
- [14] “Introduction to Modulation Transfer Function”. In: (). URL: <https://www.edmundoptics.com/resources/application-notes/optics/introduction-to-modulation-transfer-function/>.

- [15] Sibarita JB. “Deconvolution Microscopy”. In: *Rietdorf J. (eds) Microscopy Techniques. Advances in Biochemical Engineering* Vol. 95 (). Ed. by Springer, pp. 11–14.
- [16] Anton M. Jopko. “Fraunhofer Diffraction by a Circular Aperture”. In: (). URL: http://math.jbpub.com/advancedengineering/docs/Project15.4_FraunhoferDiffractionCircularAperture.pdf.
- [17] Douglas A. Kerr. “Determining MTF with a Slant Edge Target, Issue 2”. In: (2010).
- [18] “MTF - MODULATION TRANSFER FUNCTION”. In: (). URL: <http://www.telescope-optics.net/mtf.htm>.
- [19] *Residual sum of squares*. URL: https://en.wikipedia.org/wiki/Residual_sum_of_squares.
- [20] Peter J. Shaw. “Comparison of Widefield/Deconvolution and Confocal Microscopy for Three-Dimensional Imaging”. In: (). URL: https://www.jic.ac.uk/staff/peter-shaw/pdfs/Shaw_Handbook_ch23_05.pdf.
- [21] Kenneth R. Spring, John C. Long Brian O. Flynn, and Michael W. Davidson. “Spatial Resolution in Digital Imaging”. In: (). URL: <https://www.microscopyu.com/tutorials/spatial-resolution-in-digital-imaging>.
- [22] Wes Wallace, Lutz H. Schaefer, and Jason R. Swedlow. “Introduction to Deconvolution”. In: (). URL: <http://www.olympusmicro.com/primer/digitalimaging/deconvolution/deconintro.html>.
- [23] Zhou Wang et al. *Image Quality Assessment: From Error Visibility to Structural Similarity*. 2004. URL: <https://ece.uwaterloo.ca/~z70wang/publications/ssim.html>.